Journal of Advanced Ceramics
先进陶瓷
ISSN 2226-4108
CN 10-1154/TQ
清华大学出版社 Tsinghua University Press
SciOpen

J Adv Ceram 2026, **15**: 9221320

https://doi.org/10.26599/JAC.2026.9221320

Review

A review of microwave dielectric ceramics: From fundamental mechanisms and property regulation to advanced preparation, applications, and data-driven discovery

Hongyu Yang[1,†,*], Chuntao Ou[1,†], Huan Liu[2,†], Lei Li[3,*], Hua-ao Sun[4], Guangran Lin[4], Wanghuai Zhu[4], Feng Shi[4,*], Weijia Guo[5,6,*], Weijia Luo[5,6,*], Zhenxing Yue[5,*], Ying Tang[7], Jie Li[7,*], Huaicheng Xiang[7], Weishuang Fang[8], Huixing Lin[9], Junfeng Yang[10], Liang Fang[7,*], Muhammad Adnan Munir[11], Jing Guo[11,*], Kaixin Song[2*], Jincheng Qin[12], Zhifu Liu[12,*], Zhichao Hu[13], Enzhu Li[13*], Hong Wang[14,*]

[1.] *School of Advanced Materials and Nanotechnology, Xidian University, Xi'an 710071, China*

[2.] *College of Electronics Information, Hangzhou Dianzi University, Hangzhou 310018, China*

[3] *Laboratory of Dielectric Materials, School of Materials Science&Engineering, Zhejiang University, Hangzhou 310027, China*

[4.] *Shandong Key Laboratory of Advanced Glass Manufacturing and Technology, School of Materials Science and Engineering, Qilu University of Technology (Shandong Academy of Sciences), Jinan, 250353, China*

[5.] *State Key Laboratory of New Ceramic Materials, Tsinghua University, Beijing 100084, China*

[6.] *State Key Laboratory of New Ceramic Materials, Beijing Tsinghua Institute for Frontier Interdisciplinary Innovation, Beijing 102202, China*

[7.] *Guangxi Universities Key Laboratory of Non-ferrous Metal Oxide Electronic Functional Materials and Devices, Guangxi Key Laboratory of Optical and Electronic Materials and Devices, College of Materials Science and Engineering, Guilin University of Technology, Guilin 541004, China*

[8.] *College of Materials and Chemical Engineering, Hezhou University, Hezhou 542899, China*

[9.] *Key Laboratory of Inorganic Functional Material and Device, Shanghai Institute of Ceramics, Chinese Academy of Sciences, Shanghai 200050, China*

[10.] *Aurora Technologies Co. Ltd., Guangzhou 510288, China*

[11.] *State Key Laboratory for Mechanical Behavior of Materials & School of Materials Science and Engineering, Xi'an Jiaotong University, Xi'an 710049, China*

[12.] *State Key Laboratory of High Performance Ceramics, Shanghai Institute of Ceramics, Chinese Academy of Sciences, Shanghai 201899, China*

[13.] *State Key Laboratory of Electronic Thin Films and Integrated Devices, University of Electronic Science and Technology of China, Chengdu 610054, China*

[14.] *State Key Laboratory of Quantum Functional Materials, Department of Materials Science and Engineering, Southern University of Science and Technology, Shenzhen 518055, China*

† These authors contributed equally to this work.

* Corresponding author:

E-mail: H. Yang, yanghongyu@xidian.edu.cn;

L. Li, zjulilei@zju.edu.cn;

F. Shi, sf751106@sina.com;

W. Guo, guoweijia0315@163.com;

W. Luo, luoweijia.2020@tsinghua.org.cn;

Z. Yue, yuezhx@mail.tsinghua.edu.cn;

J. Li, jielee@glut.edu.cn;

L. Fang, fanglianggl001@aliyun.com;

J. Guo, jingguo19@xjtu.edu.cn;

K. Song, kxsong@hdu.edu.cn;

Z. Liu, liuzf@mail.sic.ac.cn;

E. Li, lienzhu@uestc.edu.cn;

H. Wang, wangh6@sustech.edu.cn

Received: March 30, 2026; Revised: May 11, 2026; Accepted: May 13, 2026

清華大學出版社 Tsinghua University Press | SciOpen

Abstract

Microwave dielectric ceramics (MWDCs) are pivotal to modern wireless communication systems, with their performance governed by three key parameters: relative dielectric constant (ε_r), $Q\times f$ value (product of quality factor Q (reciprocal dielectric loss) and frequency f), and temperature coefficient of resonant frequency (τ_f). This review systematically summarizes the recent research progress of MWDCs from five interrelated aspects. In terms of performance characterization, standardized resonant methods achieve ε_r measurement errors below 1% and a tanδ detection limit as low as 10^{-5}. Theoretically, frameworks from complex crystal chemistry to the recently elucidated cation rattling effect enable quantitative interpretation of dielectric behavior. In processing, the cold sintering process achieves ceramic densification below 300 °C, reducing energy consumption by over 97% in comparison with conventional sintering. For applications, these materials have been widely deployed in high-performance substrates, resonators, and filters for 5G/6G communications, with device insertion loss maintained below 1 dB. Additionally, data-driven approaches, particularly machine learning, can accurately predict key dielectric properties with a coefficient of determination (R^2) higher than 0.9, accelerating the exploration and development of novel MWDCs. By integrating these perspectives, this review offers a systematic insight into the state-of-the-art progress and future development directions of MWDCs research.

Keywords: Microwave dielectric ceramics; Microwave dielectric property measurement; Cold sintering; Dielectric theory of crystal structure; Lattice dynamics; Defect; Cation rattling effect; Wireless communication; Machine learning prediction

1. Introduction

Microwave dielectric ceramics (MWDCs) form the cornerstone of modern wireless communication technologies, serving as the essential materials for antennas, resonators, and filters in devices ranging from mobile terminals to satellite base stations [1, 2]. The ever-

increasing demand for higher data rates, miniaturization, and energy efficiency in 5G/6G networks and the Internet of Things imposes stringent requirements on the performance of these materials [3]. Their utility is fundamentally governed by three key dielectric parameters: a suitable relative dielectric constant (ε_r) for size reduction or signal transmission speed, $Q \times f$ value (product of quality factor Q (reciprocal dielectric loss) and frequency f) for frequency selectivity and low signal loss, and a near-zero temperature coefficient of resonant frequency (τ_f) for thermal stability [4, 5]. Consequently, the accurate characterization, deep understanding, and precise regulation of these properties are central to the advancement of the field.

The research and development of MWDCs have advanced along multiple interconnected fronts over the past decades. Despite significant progress, several critical research gaps remain unaddressed. Firstly, in property characterization, the accurate measurement of ultra-low dielectric loss ($\tan\delta < 10^{-5}$) is still challenging due to conductor loss and spurious mode interference, and the temperature coefficient τ_f is often treated as a constant despite its actual temperature dependence. Then, theoretical understanding of dielectric loss and τ_f is fragmented: the role of multiscale defects in anharmonic lattice vibrations is not fully quantified, and the recently recognized cation rattling effect has not yet been systematically integrated into classical dielectric theory. Thirdly, conventional high-temperature sintering (>1000 °C) causes severe energy consumption, volatilization of active elements, and incompatibility with low-melting-point electrodes, hindering the co-firing integration required for miniaturized devices. Following that, while machine learning offers new avenues for materials discovery, its application to MWDCs suffers from small datasets, lack of physics-informed descriptors, and poor model interpretability, limiting predictive accuracy and generalizability. This review aims to provide a comprehensive overview of these developments, covering five key aspects that represent the full cycle from fundamental characterization to practical application, with an explicit focus on how recent advances address the above gaps.

The three key microwave dielectric parameters (ε_r, $Q \times f$, and τ_f) serve as the central organizing principle of this review. These parameters determine the practical utility of MWDCs. The ε_r governs component miniaturization and signal propagation delay; $Q \times f$ (the product of quality factor and resonant frequency) dictates insertion loss and frequency selectivity; and τ_f ensures thermal stability against ambient temperature fluctuations. A logical framework therefore emerges: why are these parameters important for wireless communication? How can they be measured reliably and accurately? What physical mechanisms from chemical bonding to lattice dynamics, from defect chemistry to cation rattling govern their values? How can we tune them via composition design, structural engineering, and innovative processing? And how do these parameter values translate into the performance of devices such as antennas, filters, and resonators?

To answer these questions, this review is structured along a parameter-driven logical thread spanning five interconnected dimensions. First, the precise property characterization forms the cornerstone of subsequent research, necessitating the establishment of a reliable evaluation system as a first step. For the measurement of the three key parameters, resonant techniques suitable for low-loss materials are predominantly employed [6]. Among these, the TE_{011}-mode parallel plate method and the $TE_{01\delta}$-mode metal cavity method warrant particular attention as the most mature testing solutions, accurately capturing the dielectric response and providing reliable data to support material development. Building upon precise characterization, a deep understanding of the underlying physical mechanisms governing ε_r, $Q \times f$, and τ_f guides rational material design. Microwave dielectric behavior is governed by multiple interrelated factors: the dielectric theory of crystal structure reveals the intrinsic link between microscopic bonding characteristics and macroscopic properties [7, 8]; lattice dynamics elucidates the physical essence of how phonon vibrations determine the dielectric response [9]; a defect perspective on microwave dielectric loss provides critical insights into how multiscale defects, ranging from point defects to domain structures, influence anharmonic lattice vibrations and relaxation

behavior, thereby governing the ultimate loss limits of these materials [10]. Furthermore, the recently elucidated cation rattling effect offers a novel perspective on the mechanisms of temperature stability [11]. Together, these frameworks construct a comprehensive understanding from different levels.

Translating theoretical understanding into tangible materials requires innovative processing techniques to overcome the bottlenecks of traditional methods [12]. The cold sintering process, an energy efficient sintering method, achieves ceramic densification below 300°C through a dissolution-precipitation mechanism [13]. This breakthrough not only substantially reduces energy consumption during fabrication but also, more importantly, enables the co-firing of ceramics with low-melting-point materials, opening new avenues for device integration. With processing breakthroughs paving the way for high-performance materials, their ultimate value is realized through device applications. The values of ε_r, $Q\times f$, and τ_f precisely dictates a material's suitability for specific components: ceramic substrate components emphasize the synergistic optimization of dielectric constant and low loss; Low-temperature co-fired ceramic (LTCC) multilayer components require the integration of low loss, co-firing compatibility, and temperature stability [14]; and dielectric resonator components rely on high $Q\times f$ and near-zero τ_f to ensure low insertion loss and high selectivity under miniaturized conditions [15]. These application examples clearly illustrate the complete pathway from material properties to functional device performance. Concurrent with expanding applications, research methodologies themselves are undergoing a profound transformation. Data-driven paradigms are accelerating the discovery of new materials [16]. Recent progress in applying machine learning to predict the three microwave dielectric properties (ε_r, $Q\times f$, and τ_f) is particularly noteworthy, evolving from simple composition-property mapping to sophisticated models that incorporate physical mechanisms [17]. This evolution enables a more accurate capture of complex structure-property relationships, injecting new momentum into materials innovation.

2.1 Properties Evaluation: Standardized Testing and Evaluation

The three fundamental dielectric parameters of microwave dielectric ceramics—ε_r, $Q\times f$, and τ_f—require accurate measurements for both research and application. Microwave dielectric measurement methods fall into two categories [18]. In transmission line (non-resonant) methods, a shaped sample is placed in a transmission line, and the complex permittivity at a given frequency is extracted from the complex *S*-parameters measured at that frequency [18]. The key advantage of transmission line methods lies in their ability to perform rapid and broadband measurements via frequency sweeping. However, the low measurement accuracy and susceptibility to interference restrict their applicability to materials with low ε_r and medium/high tanδ. In contrast, resonant methods utilize electromagnetic resonance in a microwave resonator containing the sample. Measuring *S*-parameter variation near the resonance peak yields resonant characteristics, which depend on the sample's dielectric properties, resonator structure, dimensions, and resonant mode. Hence, the dielectric properties at the resonant frequency can be extracted [18, 19]. Resonant methods offer significantly higher accuracy than transmission line methods because resonant characteristics can be measured precisely. However, resonant methods provide measurements only at single or discrete frequencies, and are generally unsutable for high-loss materials, where resonance peaks are difficult to observe. Consequently, resonant methods are primarily applicable to low-loss (tanδ < 0.01) non-magnetic materials such as microwave dielectric ceramics. In practice, most resonant methods are dielectric resonator methods [19].

2.1.1 Measurement of Resonant Characteristics

Microwave resonators employed in dielectric resonator methods are generally configured as either one-port reflection-type or two-port transmission-type devices [20, 21]. The fundamental resonant characteristics that define their performance are the resonant frequency (f_0) and the unloaded quality factor (Q_u). The measurement of f_0 is relatively straightforward: for reflection-type resonators, it is identified as the frequency at which the magnitude of S_{11} (reflection) reaches its minimum, while for transmission-type resonators, it corresponds to the frequency

where S_{21} (transmission) attains its maximum value. In contrast, the determination of Q_u is considerably more intricate, as it cannot be measured directly. Instead, it must be derived from two measurable parameters: loaded quality factor (Q_L) and the coupling coefficient (κ). The commonly referenced quality factor obtained by dividing f_0 by the half-power bandwidth Δf is precisely Q_L, expressed mathematically as:

$$Q_L = \frac{f_0}{\Delta f} \tag{1}$$

For a single-port reflection-type resonator, the relationship connecting these parameters is:

$$Q_u = Q_L(1+\kappa) \tag{2}$$

Consequently, accurate determination of Q_u requires measuring both Δf (or Q_L) and κ. Referring to **Fig. 1(a)**, the half-power bandwidth Δf is obtained by identifying the frequencies at which S_{11} equals a specific value, calculated using the formula:

$$S_{11,\Delta f} = 10\log_{10}\left(\frac{10S_{11,b}/10 + 10S_{11,f_0}/10}{2}\right) \tag{3}$$

where $S_{11,b}$ and $S_{11,f0}$ represent the S_{11} values at the resonance baseline and resonant frequency respectively. The coupling coefficient κ can be determined using Smith chart analysis [22]. By plotting the complex S_{11} response near resonance and fitting it to a circle, one obtains a resonance circle with diameter d. Constructing an additional loss circle through the open-circuit and detuned points yields a diameter d_2, allowing κ to be calculated as:

$$\kappa = \frac{d}{d_2 - d} \tag{4}$$

For two-port transmission-type resonators, the relationship becomes:

$$Q_u = Q_L(1+\kappa_1+\kappa_2) \tag{5}$$

where κ_1 and κ_2 are the coupling coefficients for each port. Here, Q_L is determined from the -3dB bandwidth of the S_{21} frequency response.

Referring to **Fig. 1(b)**, S_{21} at the half-power points can be determined using the following formula:

$$S_{21,\Delta f} = S_{21,f_0} - 3\text{dB} \tag{6}$$

When the coupling coefficients can be made approximately equal ($\kappa_1 = \kappa_2 = \kappa$), a simplified expression emerges:

$$2\kappa = \frac{\left|S_{21,f_0}\right|}{1-\left|S_{21,f_0}\right|} \tag{7}$$

Substituting this into the Q_u equation yields [21]:

$$Q_u = \frac{Q_L}{1-10^{S_{21,f_0}/20}} \tag{8}$$

Thus, by using a vector network analyzer to measure the complex S-parameters near resonance, both Q_L and the coupling coefficients can be determined, enabling calculation of Q_u [18, 21, 22].

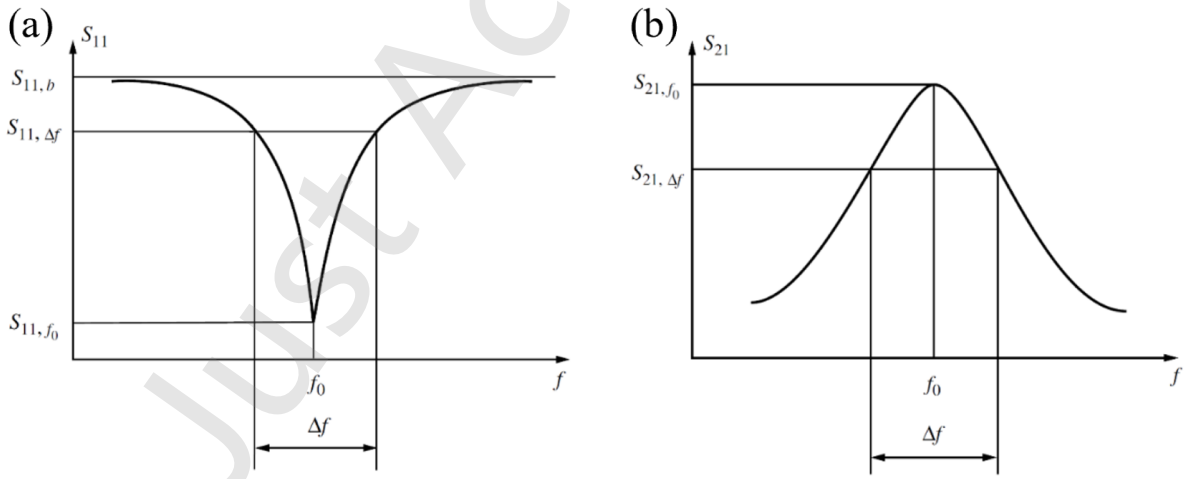

Figure 1. Measurement of f_0 and Δf from resonance peaks characterized by (a) S_{11} of a reflection-type resonator and (b) S_{21} of a transmission-type resonator [18]. Reproduced with permission from Ref. [18], © John Wiley & Sons, 2004.

2.1.2 Extracting Procedures of ε_r and tanδ

As previously discussed, the resonant characteristics (f_0 and Q_u) of a dielectric resonator containing the sample under test are jointly determined by the sample's dielectric properties,

the resonator structure, dimensions, and the specific resonant mode employed. Therefore, by measuring these resonant characteristics, one can extract the dielectric properties of the sample at the resonant frequency. Specifically, when the resonant mode and the physical dimensions of both the resonator and sample are fixed, ε_r can be calculated from f_0 through a relatively straightforward process. In contrast, extracting tanδ from Q_u is considerably more complex, as it involves numerous intermediate parameters and calculations.

The unloaded quality factor Q_u of a dielectric resonator fundamentally represents the reciprocal of its total unloaded loss, defined as 2π times the ratio of electromagnetic energy stored in the resonator to the energy dissipated per cycle [19]. For resonators used in microwave dielectric measurements, the absence of radiation loss is a fundamental requirement. Consequently, the total unloaded loss comprises two components: loss attributable to the dielectric materials and loss caused by the conductor walls. Their reciprocals are defined as the dielectric quality factor (Q_d) and the conductor quality factor (Q_c) respectively, giving the relationship:

$$\frac{1}{Q_u} = \frac{1}{Q_d} + \frac{1}{Q_c} \tag{9}$$

Here, all lossy dielectrics within the resonator contribute to the $1/Q_d$ term, with the contribution determined by their electric energy filling factors ($P_{e,i}$), expressed as:

$$\frac{1}{Q_d} = \sum_i \left(P_{e,i} \tan \delta_i \right) \tag{10}$$

where i denotes each dielectric region. The electric energy filling factor represents the ratio of electric energy stored in a specific dielectric to the total electric energy stored in all dielectrics, ranging between 0 and 1, with the sum of all filling factors equaling unity.

In practical measurements, air's dielectric loss is typically negligible. Furthermore, support structures used in some dielectric resonator methods generally have both low loss and very small electric energy filling factors, making their contribution to $1/Q_d$ negligible. In such cases,

as in the TE_{011}-mode parallel plate method and $TE_{01\delta}$-mode metal resonant cavity method, $1/Q_d$ is determined solely by the sample, simplifying the relationship to:

$$\frac{1}{Q_u} = P_e \cdot \tan\delta + \frac{1}{Q_c} \tag{11}$$

Conductor loss ($1/Q_c$) arises from electrical currents flowing through the conductor surfaces, converting electrical energy to heat due to finite conductivity. Due to the skin effect at microwave frequencies, current flow and associated losses are confined to a thin surface region with depth on the order of micrometers, making the effective surface conductivity (σ_s) closely related to surface roughness and typically lower than bulk conductivity. Therefore, σ_s must be determined before calculating Q_c based on surface current distribution in the conductor walls.

In a brief summary, the complete extraction procedure involves: extracting ε_r from measured f_0, solving for the electromagnetic field distribution and calculating P_e, determining σ_s and solving for surface current distribution to obtain Q_c, and finally extracting $\tan\delta$ using Eq. 11. This process generally requires computer implementation due to its mathematical complexity, employing either analytical solutions for simple structures like parallel plate resonators or numerical methods for more complex configurations [19].

2.1.3 Parallel Plate Method and Metal Resonant Cavity Method

There are numerous methods for measuring microwave dielectric properties based on dielectric resonance, but practical factors like sample preparation, mode identification, and accuracy limit their application. Cylindrical resonators with cylindrical samples are most common. While ε_r can be measured with errors below 1%, $\tan\delta$ measurement is more complex and error-prone, largely influenced by the conductor quality factor Q_c. High Q_c is essential for the measurement accuracy and limit of low $\tan\delta$. TE_{0np} modes, especially TE_{011}, are preferred due to their high Q_c. This section focuses on the TE_{011}-mode parallel plate method and $TE_{01\delta}$-mode metal resonant cavity method. Both the two methods are suitable and mostly used for low-loss

materials like microwave dielectric ceramics, and the resonant cavity method offers wider range and higher accuracy for tanδ.

As shown in **Fig. 2**, a cylindrical sample with diameter D and height H is clamped between two parallel metal plates of diameter D_0, forming a parallel plate dielectric resonator. First proposed by Hakki and Coleman [23] and later refined by Courtney [24], this method is also known as the Hakki-Coleman method, Courtney method, or open cavity method due to its open structure.

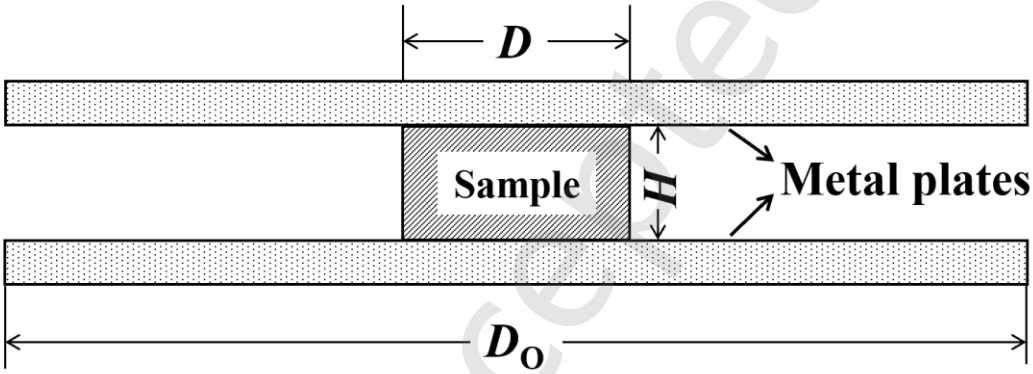

Figure 2. Schematic diagram of parallel plate method.

The parallel plate dielectric resonator is derived from a short-circuited dielectric waveguide. For ideal operation, the metal plates should be infinitely large to prevent radiation. In practice, however, this method requires a finite diameter of metal plates that is several times large than the sample diameter and specific diameter-to-height ratios (typically 1.9-2.3) to ensure the TE_{011} mode operates in a "trapped state" without radiation loss.

For an ideal resonator with infinitely large plates, the characteristic equation for each resonant mode is given by:

$$\left[\frac{\varepsilon_r J_m'(\alpha)}{\alpha J_m(\alpha)}+\frac{K_m'(\beta)J_m'(\alpha)}{\beta K_m(\beta)}\right]\left[\frac{J_m'(\alpha)}{\alpha J_m(\alpha)}+\frac{K_m'(\beta)}{K_m(\beta)}\right]=m^2\left(\frac{\varepsilon_r}{\alpha^2}+\frac{1}{\beta^2}\right)\left(\frac{1}{\alpha^2}+\frac{1}{\beta^2}\right) \quad (12)$$

This equation also applies to the trapped modes in practical resonators. In this equation, J_m and K_m are the mth order Bessel functions of the first and second kinds, respectively, m and p are

azimuthal and axial mode numbers, and α and β are parameters defined by Eqs. 13 and 14, which depend on the resonant frequency f_0, sample dimensions, and ε_r.

$$\alpha = \frac{\pi D f_0}{c_0}\sqrt{\varepsilon_r - \left(\frac{p c_0}{2 f_0 H}\right)^2} \tag{13}$$

$$\beta = \frac{\pi D f_0}{c_0}\sqrt{\left(\frac{p c_0}{2 f_0 H}\right)^2 - 1} \tag{14}$$

where c_0 is the speed of light in vacuum. Among all modes, TE_{0np} modes exhibit the highest conductor quality factor Q_c, making them most suitable for measuring low-loss materials. For the fundamental TE_{011} mode ($m = 0$, $p = 1$), Eq. 12 simplifies to Eq. 15.

$$\frac{J_0(\alpha_1)}{K_0(\beta_1)} = -\frac{\beta_1 J_1(\alpha_1)}{\alpha_1 K_1(\beta_1)} \tag{15}$$

If ε_r is known, the first root of this equation yields the resonant frequency. Conversely, if the resonant frequency f_0 is measured, Eq. 15 can be used to calculate ε_r. To measure tanδ using the TE_{011} mode, Eq. 11 is applicable since dielectric loss comes almost exclusively from the sample. The electric energy filling factor P_e of the sample in Eq. 11 is determined by:

$$P_e = \frac{1}{1 + \frac{W}{\varepsilon_r}} \tag{16}$$

$$W = \frac{J_1^2(\alpha_1)}{K_1^2(\beta_1)} \cdot \frac{K_0(\beta_1)K_2(\beta_1) - K_1^2(\beta_1)}{J_1^2(\alpha_1) - J_0(\alpha_1)J_2(\alpha_1)} \tag{17}$$

The conductor quality factor Q_c, required in Eq. 11, is calculated using:

$$Q_c = \frac{30\pi^2(\varepsilon_r + W)}{(1+W)R_s} \cdot \left(\frac{2 f_0 H}{c_0}\right)^3 \tag{18}$$

$$R_s = \sqrt{\frac{\pi f_0 \mu}{\sigma_s}} \tag{19}$$

which depend on the surface resistance R_s and thus the surface conductivity σ_s of the metal plates. Determining σ_s is essential and can be achieved through two approaches. The first uses

a single standard sample with known tanδ: measure f_0 and Q_u, calculate P_e, derive Q_c from Eq. 11, and then obtain σ_s from Eqs. 18 and 19. The second uses two standard samples of the same material and diameter but different heights (H and pH). By measuring the TE_{011} and TE_{01p} modes (which ideally have the same f_0), the difference in conductor loss allows Q_c to be solved from Eqs. 20 and 21, from which σ_s is then calculated.

$$\frac{1}{Q_{u,1}} = P_{e,1} \cdot \tan\delta + \frac{1}{Q_{c,1}} \tag{20}$$

$$\frac{1}{Q_{u,2}} = P_{e,1} \cdot \tan\delta + \frac{1}{pQ_{c,1}} \tag{21}$$

Although higher-order TE_{0np} modes can, in principle, measure dielectric properties at higher frequencies by using the appropriate roots of Eq. 12, their practical application is limited. Their resonant peaks are often obscured by spurious modes, making identification and accurate measurement difficult.

As discussed above, the TE_{011} mode in parallel plate resonators is suitable for low-loss materials due to lower conductor loss, but its Q_c is limited to a few thousands (conductor loss on the order of 10^{-4}), causing errors for very low dielectric loss. This limitation arises from direct sample contact with conducting walls, inducing large surface current and conductor loss. The metal resonant cavity method, where the sample is placed on a support away from walls, as shown in **Fig. 3**, reduces conductor loss, increases Q_c, and improves accuracy. It extends the tanδ measurement limit from 10^{-4} (parallel plate) to 10^{-5}, meeting microwave dielectric ceramic requirements.

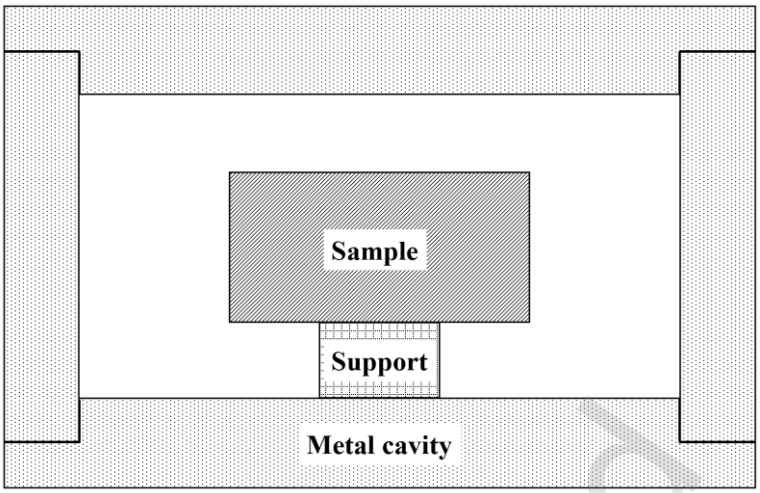

Figure 3. Schematic diagram of metal resonant cavity method.

Due to its enclosed structure, the metal resonant cavity method is also known as the closed cavity method. A small, low-ε_r, and low-tanδ support minimizes its effect on resonance. The TE_{011} mode used here is also denoted as $TE_{01\delta}$, where "δ" indicates that the axial mode number within the sample is less than 1, though the full-cavity mode number remains 1. Thus, $TE_{01\delta}$ is essentially equivalent to the TE_{011} mode in the parallel plate method. Although slightly more complex, this structure lacks an analytical solution, requiring numerical methods to extract dielectric properties. Numerical methods such as mode matching, Rayleigh-Ritz, finite element, and finite difference methods can be used to calculate the f_0 and field distribution from the sample's ε_r [19, 25]. For property extraction, an inverse approach is needed: an initial ε_r is assumed, f_0 is calculated, and the result is compared to the measured f_0. ε_r is iteratively adjusted until the frequency difference is sufficiently small (e.g., $<10^{-5}$), yielding an accurate ε_r value.

In the metal resonant cavity method, the contribution of the support to the total loss of the resonant system is generally negligible. Therefore, the tanδ of the sample can also be determined using Eq. 11 based on the measured Q_u and calculated P_e and Q_c. Here, P_e is obtained from the electromagnetic field distribution using Eq. 22, while Q_c is calculated using Kajfez's incremental frequency rule, which is applicable to TE_{0np} modes in cylindrical resonant cavities [26].

$$P_{e,i} = \frac{\int_{V_i} \frac{1}{2} \varepsilon_{r,i} E^2 dV_i}{\sum_i \left(\int_{V_i} \frac{1}{2} \varepsilon_{r,i} E^2 dV_i \right)} \tag{22}$$

This rule assumes that all the inner conductor walls of the cavity are moved inward by the skin depth δ, which increases the resonant frequency f_0. The increment in resonant frequency $\Delta f_0(\delta)$ can be calculated numerically, and Q_c is obtained by:

$$Q_c = \frac{f_0}{\Delta f_0(\delta)} \tag{23}$$

$$\delta = \frac{1}{\sqrt{\pi f_0 \mu \sigma_s}} \tag{24}$$

Similar to the parallel plate method, the surface conductivity of conductor walls (σ_s) is also required for calculating δ and Q_c for the metal resonant cavity method. The σ_s can be determined from the measured Q_u of TE_{011} mode for the empty cavity without any sample inside. Since the contribution of the support to the resonator loss is negligible, Q_c equals to Q_u. Using Eq. 23, $\Delta f_0(\delta)$ and δ are obtained for the empty cavity, and σ_s can then be derived from Eq. 24. The higher-order TE_{0np} modes can also be utilized for measuring the microwave dielectric properties at higher frequencies [27]. However, similar to the situation for parallel plate method, the utilization of these higher-order modes in metal resonant cavity method are also limited because their identification and accurate measurement are challenging and strongly rely on the measurement experience.

The routine measurement of τ_f is quite simple. By measuring the resonant frequencies of a dielectric resonator containing the sample under test at two separated temperatures T_1 and T_2 (typically 20 °C and 80 °C), τ_f can be easily calculated from Eq. 25.

$$\tau_f = \frac{f_0(T_2) - f_0(T_1)}{f_0(T_1) \cdot (T_2 - T_1)} \tag{25}$$

However, one should notice that the τ_f obtained from Eq. 25 is the τ_f of the resonator ($\tau_{f,r}$), but not that of the sample ($\tau_{f,s}$). $\tau_{f,s}$ equals to $\tau_{f,r}$ only for an ideal dielectric resonator that is fully

filled with the material under test, but does not contain any other dielectric such as air and support. Since the parallel plate resonator is much closer to the ideal one than the metal cavity resonator, it is suggested to measure $\tau_{f,s}$ by the parallel plate method, for which the assumption of $\tau_{f,s} = \tau_{f,r}$ is acceptable in most cases [28, 29]. If the metal resonant cavity method is used for measurement instead, the $\tau_{f,r}$ obtained by Eq. 25 should be corrected via a complex procedure, especially for the samples with low ε_r [28, 29]. Besides, τ_f may exhibits significant temperature dependence, although it is usually regarded as a temperature-independent constant [30]. Therefore, it is recommended to measure the f_0 at multiple temperatures over a wider temperature range (e.g., -40 °C to 80 °C) with smaller temperature intervals (e.g., 20 °C) [28, 30], so that the temperature depdence of τ_f can be revealed, which is very imporatnt for understanding the real temperature instability of microwave dielectric ceramics.

2.2 Properties Regulation: Theoretical Basis of Microwave Dielectric Mechanism

A fundamental starting point for understanding microwave dielectric properties is the Clausius–Mossotti (C–M) equation, which relates the ε_r to the total polarizability of constituent ions [31]:

$$\frac{\varepsilon_r - 1}{\varepsilon_r + 2} = \frac{4\pi\alpha}{3V_m} \tag{26}$$

In this equation, V_m represents the molar volume. The total molecular polarizability (α) of the system can be regarded as the sum of inter ion polarizability. Shannon calculated ionic polarizabilities via least-squares fitting of the Clausius–Mossotti equation to the dielectric constants of 129 oxides and 25 fluorides. Hence, the theoretical ionic polarizabilities enable estimation of the dielectric constant of a given material system. It is noteworthy that discrepancies between predicted and measured dielectric constants frequently arise from compressed or rattling states of cations, or from dipolar impurities [31]. This equation provides the microscopic basis for ε_r. The C–M equation serves as the theoretical foundation. The P–V–L bond theory can be viewed as a bond-level decomposition of α; lattice dynamics provides a phonon-based calculation of polarizability; and the cation rattling effect offers an explanation

for anomalous polarizability temperature dependence, which directly influences τ_f as derived in that subsection.

2.2.1 Dielectric theory of crystal structure

Dielectric theory of crystal structure was originally established by Phillips, Van Vechten and Levine [32-37], also known as the P–V–L bond theory, which provides important bond features. These bonding features of crystalline materials are essential for interpreting both the chemical and solid-state physical properties of crystal structures. These concepts enable a qualitative understanding of various crystalline traits. In the early 1970s, Phillips and Van Vechten (P–V) introduced a chemical bond theory that marked the first quantitative approach to characterizing crystal properties. Rooted in the dielectric description of solids, this framework provides a method to calibrate bond-related parameters and delineate the interrelations among various microscopic quantities within crystals. The theory has been widely applied to compute numerous crystal attributes, such as bond charge [38, 39], electronic structure [40], thermodynamic behavior [41], band structures [42], et al. It is important to mention, however, that the P–V theory is limited to eight-electron A^NB^{8-N} type crystals containing only one bond type. Subsequently, Levine extended the P–V formalism to more complex systems, including A_mB_n, $A^IB^{III}C_2^{VI}$, $A^{II}B^{IV}C_2^{V}$, and $A^{III}B^{V}C_4^{VI}$ families. This was accomplished by partitioning bulk crystal properties into contributions from individual bonds, incorporating parameters such as polarizability, ionicity, and average electron count per bond [36]. Despite this advancement, the extended model still requires the simultaneous presence of two bond types, identical coordination numbers, and nearly equivalent nearest-neighbor distances. Nonetheless, it introduced the foundational idea of normalizing macroscopic characteristics to individual bonds.

In materials research, compositional systems are rarely limited to binary combinations. High-entropy ceramics, for instance, typically consist of five or more metallic elements in near-equimolar ratios [43]. Likewise, in the field of microwave dielectric ceramics, ionic modification commonly relies on ternary systems, as exemplified by Ba–Mg–Al–Si–O [44],

Zn–Nb–Ti–O [45], and Yb–Si–O [46], et al. A deep understanding of how bonding features influence crystal structures is therefore essential. To solve this issue, the P–V–L bond theory requires appropriate refinement to ensure its effective applicability to such multi-component systems. Zhang then proposed a strategy of deconstructing such polycrystalline compounds into simpler A_mB_n binary units [7, 47]:

$$A_{a1}^{1}A_{a2}^{2}A_{a3}^{3}\cdots A_{aj}^{i}B_{b1}^{1}B_{b2}^{2}B_{b3}^{3}\cdots B_{bj}^{i} = \sum\nolimits_{ij} A_{mi}^{i}B_{nj}^{j} \tag{27}$$

Here, A and B denote cations and anions, respectively, while A^i and B^j represent either distinct elements or symmetry-equivalent positions of the same element, with a_i and b_j indicating their respective stoichiometric coefficients. The m and n values are calculated considering the given coordination number N_{cAi} and N_{cBj}, where the detailed calculation process can be found elsewhere. Within this framework, a crystal is treated as an assembly of chemical bonds formed between constituent ions. It is assumed that the paired ions forming each bond occupy crystallographically equivalent symmetric sites, and bonds sharing identical interatomic distances are grouped into a single bond type. Each distinct bond type, represented in binary form, possesses unique bond parameters, spatial geometry, and elemental stoichiometry. By designating the elemental proportion associated with a given bond type as its binary bond formula, every bond category within the crystal corresponds to a specific binary representation. The overall crystal can thus be viewed as a composite of all such bond types, with its molecular formula derived from the superposition of all corresponding binary bond formulas. In this way, the P–V–L bond theory becomes applicable for quantifying the properties of each binary bond formula. Once the linkage between binary bond formulas and the parent complex crystal is established, it becomes possible to systematically investigate the bonding characteristics of intricate crystalline phases and to correlate microscopic structural parameters with macroscopic material behavior. A case in point for deviding the $Al_2Mo_3O_{12}$ is presented in **Table 1**.

Table 1. Coordinate environments of the $Al_2Mo_3O_{12}$ structure

Bond	$N_{(Bj\text{-}Ai)}$	Bond	$N_{(Bj\text{-}Ai)}$	Bond	$N_{(Bj\text{-}Ai)}$	Bond	$N_{(Bj\text{-}Ai)}$	Bond	$N_{(Bj\text{-}Ai)}$
Al^1 (CN = 6)		Al^2 (CN = 6)		Al^3 (CN = 6)		Al^4 (CN = 6)		Mo^1 (CN = 4)	
Al^1–O^6	1	Al^2–O^1	1	Al^3–O^2	1	Al^4–O^9	1	Mo^1–O^7	1
Al^1–O^7	1	Al^2–O^3	1	Al^3–O^8	1	Al^4–O^{12}	1	Mo^1–O^9	1
Al^1–O^{13}	1	Al^2–O^4	1	Al^3–O^{11}	1	Al^4–O^{14}	1	Mo^1–O^{12}	1
Al^1–O^{16}	1	Al^2–O^5	1	Al^3–O^{17}	1	Al^4–O^{15}	1	Mo^1–O^{20}	1
Al^1–O^{20}	1	Al^2–O^{10}	1	Al^3–O^{18}	1	Al^4–O^{19}	1		
Al^1–O^{24}	1	Al^2–O^{23}	1	Al^3–O^{22}	1	Al^4–O^{21}	1		
Mo^2 (CN = 4)		Mo^3 (CN = 4)		Mo^4 (CN = 4)		Mo^5 (CN = 4)		Mo^6 (CN = 4)	
Mo^2–O^2	1	Mo^3–O^5	1	Mo^4–O^{14}	1	Mo^5–O^{17}	1	Mo^6–O^1	1
Mo^2–O^3	1	Mo^3–O^6	1	Mo^4–O^{16}	1	Mo^5–O^{19}	1	Mo^6–O^{10}	1
Mo^2–O^4	1	Mo^3–O^8	1	Mo^4–O^{18}	1	Mo^5–O^{23}	1	Mo^6–O^{11}	1
Mo^2–O^{13}	1	Mo^3–O^{15}	1	Mo^4–O^{21}	1	Mo^5–O^{24}	1	Mo^6–O^{22}	1
O^1 (CN = 2)		O^2 (CN = 2)		O^3 (CN = 2)		O^4 (CN = 2)		O^5 (CN = 2)	
O^1–Al^2	1	O^2–Al^3	1	O^3–Al^2	1	O^4–Al^2	1	O^5–Al^2	1
O^1–Mo^6	1	O^2–Mo^2	1	O^3–Mo^2	1	O^4–Mo^2	1	O^5–Mo^3	1
O^6 (CN = 2)		O^7 (CN = 2)		O^8 (CN = 2)		O^9 (CN = 2)		O^{10} (CN = 2)	
O^6–Al^1	1	O^7–Al^1	1	O^8–Al^3	1	O^9–Al^4	1	O^{10}–Al^2	1
O^6–Mo^3	1	O^7–Mo^1	1	O^8–Mo^3	1	O^9–Mo^1	1	O^{10}–Mo^6	1
O^{11} (CN = 2)		O^{12} (CN = 2)		O^{13} (CN = 2)		O^{14} (CN = 2)		O^{15} (CN = 2)	
O^{11}–Al^3	1	O^{12}–Al^4	1	O^{13}–Al^1	1	O^{14}–Al^4	1	O^{15}–Al^4	1
O^{11}–Mo^6	1	O^{12}–Mo^1	1	O^{13}–Mo^2	1	O^{14}–Mo^4	1	O^{15}–Mo^3	1
O^{16} (CN = 2)		O^{17} (CN = 2)		O^{18} (CN = 2)		O^{19} (CN = 2)		O^{20} (CN = 2)	
O^{16}–Al^1	1	O^{17}–Al^3	1	O^{18}–Al^3	1	O^{19}–Al^4	1	O^{20}–Al^1	1
O^{16}–Mo^4	1	O^{17}–Mo^5	1	O^{18}–Mo^4	1	O^{19}–Mo^5	1	O^{20}–Mo^1	1
O^{21} (CN = 2)		O^{22} (CN = 2)		O^{23} (CN = 2)		O^{24} (CN = 2)			
O^{21}–Al^4	1	O^{22}–Al^3	1	O^{23}–Al^2	1	O^{24}–Al^1	1		
O^{21}–Mo^4	1	O^{22}–Mo^6	1	O^{23}–Mo^5	1	O^{24}–Mo^5	1		

Note: CN is the coordination number, and $N_{(Bj\text{-}Ai)}$ represents the number of A^i cations in the ligand of B^j ion.

The schematic diagram of crystal structure and bonding environment are shown in **Fig. 4** [48]. One can get a visualization of coordination environment via COD No. 1530062 [49]. Thus, the A_mB_n binary units can be obtained, as shown in Eq. 28:

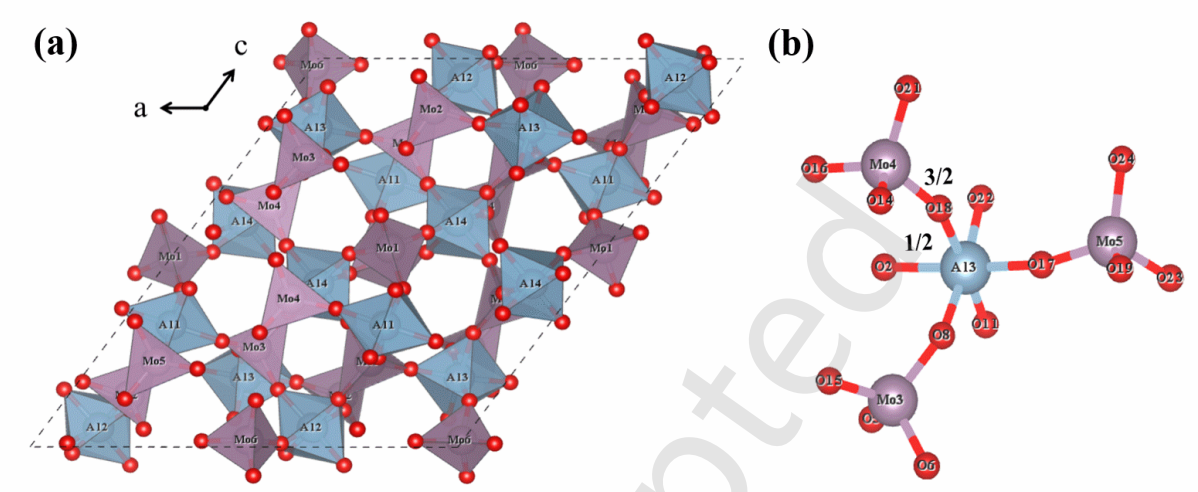

Figure 4. Schematic diagram of (a) $Al_2Mo_3O_{12}$ crystal structure, and (b) bonding environment coordinates and charge profiles of cations in $Al_2Mo_3O_{12}$. Reproduced with permission from Ref. [48], © Elsevier Ltd. and Techna Group S.r.l. 2023.

$$\begin{aligned} Al_2Mo_3O_{12} &= Al^1{}_{1/2}Al^2{}_{1/2}Al^3{}_{1/2}Al^4{}_{1/2}Mo^1{}_{1/2}Mo^2{}_{1/2}Mo^3{}_{1/2}Mo^4{}_{1/2}Mo^5{}_{1/2}Mo^6{}_{1/2}O_{12} \\ &= \sum_{i=1}^{4}\left(Al^i{}_{1/12}O^a{}_{1/4} + Al^i{}_{1/12}O^b{}_{1/4} + Al^i{}_{1/12}O^c{}_{1/4} + Al^i{}_{1/12}O^d{}_{1/4} + Al^i{}_{1/12}O^e{}_{1/4} + Al^i{}_{1/12}O^f{}_{1/4}\right) \\ &+ \sum_{i'=1}^{6}\left(Mo^{i'}{}_{1/8}O^{a'}{}_{1/4} + Mo^{i'}{}_{1/8}O^{b'}{}_{1/4} + Mo^{i'}{}_{1/8}O^{c'}{}_{1/4} + Mo^{i'}{}_{1/8}O^{d'}{}_{1/4}\right) \end{aligned} \quad (28)$$

For simplicity, i (ranging from 1 to 4) and i' (ranging from 1 to 6) denote the distinct types of Al and Mo atoms, respectively. The symbols *a-f* and *a*'-*d*' correspond to the associated oxygen anions. The cations possess valence electron numbers of $Z_{Al} = 3$ and $Z_{Mo} = 6$. The effective valence electron count for each oxygen anion is determined by bond electroneutrality, yielding values of 3 for Al–O bonds and 9 for Mo–O bonds. After obtaining the m and n values for binary units, the fundamental bond features, mainly including bond ionicity (f_i), bond covalency (f_c) and bond susceptibility (χ), can be calculated. Determining the ionic and covalent contributions of chemical bonds in crystal structure of oxide ceramic is of great interest, as bonds are seldom purely ionic or purely covalent in nature. For any μ bond in A_mB_n binary unit, the f_i (f_c) value is defined as:

$$f_{\mathrm{i}}^{\mu}=\left(C^{\mu}\right)^{2}\cdot\left(E_{\mathrm{g}}^{\mu}\right)^{-2} \tag{29}$$

$$f_{\mathrm{c}}^{\mu}=\left(E_{\mathrm{h}}^{\mu}\right)^{2}\cdot\left(E_{\mathrm{g}}^{\mu}\right)^{-2} \tag{30}$$

$$C^{\mu}=14.4\cdot b^{\mu}\cdot\left[\left(Z_{\mathrm{A}}^{\mu}\right)^{*}-\frac{n}{m}\left(Z_{\mathrm{B}}^{\mu}\right)^{*}\right]\cdot\exp\left(-k_{s}r_{0}^{\mu}\right)/r_{0}^{\mu}\ \ (n>m) \tag{31}$$

Here, C^{μ} denotes the heteropolar contribution of a given μ bond, E_{g}^{μ} represents its average energy gap, and E_{h}^{μ} corresponds to the homopolar component. $(Z_{\mathrm{A}}^{\mu})^{*}$ and $(Z_{\mathrm{B}}^{\mu})^{*}$ indicate the effective valence electron counts. r_0^{μ} refers to half the bond length derived from Rietveld refinement results. The parameters m and n are those appearing in the binary bond formula A_mB_n. The term $\exp(-k_s\cdot r_0^{\mu})$ gives the Thomas–Fermi shielding factor, which can be acquired from the crystal structure detail. Levine extended the P–V theory to binary multi bond A_mB_n crystals, thus, the macroscopic properties of the crystals are regarded as the sum of microscopic contributions of chemical bonds. In Levine's extension, the macroscopic susceptibility can be divided into the sum of the microscopic bond susceptibility, as shown below:

$$\chi=\sum\nolimits_{\mu}F^{\mu}\cdot\chi^{\mu} \tag{32}$$

Here, F^{μ} represents the proportion of μ-class chemical bonds in the structure; The bond susceptibility of μ-class chemical bonds is represented by χ^{μ}, which is obtained from:

$$\chi^{\mu}=\frac{1}{4\pi}\cdot\left(\frac{\hbar\cdot\Omega_{\mathrm{p}}^{\mu}}{E_{\mathrm{g}}}\right)^{2} \tag{33}$$

$$\varepsilon^{\mu}=4\pi\chi^{\mu}+1 \tag{34}$$

Here, ε^{μ} is the dielectric constant of the two types of chemical bonds in μ; $\Omega_{\mathrm{p}}^{\mu}$ refers to the plasma frequency of the μ-class chemical bond, which can be calculated from previous reports. Following the bond features calculated via P–V–L bond theory, lattice energy (U_{lattice}) and thermal expansion (α_{L}) of any structure can be estimated from ionic part and covalent part:

$$U_{\mathrm{lattice}}=\sum\left(U_{\mathrm{bi}}^{\mu}+U_{\mathrm{bc}}^{\mu}\right) \tag{35}$$

$$U_{\mathrm{bi}}^{\mu}=1270\frac{(m+n)\cdot Z_{+}^{\mu}\cdot Z_{-}^{\mu}}{d^{\mu}}\cdot\left(1-\frac{0.4}{d^{\mu}}\right)\cdot f_{\mathrm{i}}^{\mu} \tag{36}$$

$$U_{\mathrm{bc}}^{\mu}=2100\frac{\left(Z_{+}^{\mu}\right)^{1.64}\cdot Z_{-}^{\mu}}{\left(d^{\mu}\right)^{0.75}}\cdot f_{\mathrm{c}}^{\mu} \tag{37}$$

$$\alpha_{mn}=-3.1685+0.8376\cdot\gamma_{mn} \tag{38}$$

$$\gamma_{mn}=\frac{kZ_{\mathrm{A}}N_{\mathrm{cA}}}{U_{\mathrm{lattice}}\Delta_{\mathrm{A}}}\cdot\frac{m\cdot(m+n)}{2n} \tag{39}$$

Here, Z_{+}^{μ} and Z_{-}^{μ} represent the valence state of ions, d^{μ} is the bond length. Δ_{A} is the correction parameter [50], k is the Boltzmann constant, and U_{lattice} is the lattice energy of any bond. In addition, the U_{lattice} value reflects the interionic cohesive energy; a larger value suggests a more robust crystal structure and implies diminished internal losses caused by anharmonic vibrations.

The usage of P–V–L bond theory theory has used to analyze the bonding characteristics in many structures. In $CaWO_4$ crystal, the W–O bond shows higher covalent properties [51] due to the contribution of both the 2p state of O and the 5d state of W to the top of the valence band and the bottom of the conduction band. Zhang's group quantified the maximum covalency of the W–O bond: f_{c} (W–O) = 31.14% > f_{c} (Ca–O) = 24.20% [52]. Furthermore, first principles calculations indicate that the Ln_2TiO_5 system produces a larger ELF value (>0.5) due to localized/non bonded electrons, while the ionicity of the Ln/Ti–O bond is a crucial factor, resulting in a smaller value (<0.5) for delocalized electrons. In the Ti(3d)–O(2p) orbital interaction of the σ bond, the Ti–O bond has higher covalency than the Ln–O bond [53]. Wu's group calculated that the Ti–O bond has the highest covalency [54], also consistent with first principles calculations. In the $Y_3Al_5O_{12}$ structure, Al contains two kinds of coordination lattice points (four coordination and six coordination). Guo's group confirmed that the four coordinated Al ion has stronger covalence than the six coordinated Al ion, and the Y–O bond is more ionic [55] through first principle calculation. Zhang's group quantified the specific

covalence of each bond and agreed with the first principal conclusion: f_c (Al^2–O) = 31.2% > f_c (Al^1–O^1) = 13.1% > f_c (Y–O) = 6.6%.

On the other hand, the correlation between bond characteristics and high-frequency dielectric properties has also received public attention. Ohsato's group has associated covalency with dielectric constant and reported that the low dielectric properties of silicate systems are due to the large covalency of the [SiO_4] tetrahedral skeleton [56]; Li's group calculated that the significant covalent nature of Si–O bonds and the proportion of bond susceptibility reflect the important influence of Si–O bonds on dielectric properties in $CaMgSi_2O_6$ system [57]. Also, Hanuza's group calculated the Raman vibration peaks at 901 cm^{-1}, 650 cm^{-1}, and 615 cm^{-1} in the $A_2BSi_2O_7$ system (A = Sr, Ca; B = Mg, Zn) through lattice dynamics, indicating that they belong to the symmetric stretching vibration of SiO_3 groups, the symmetric stretching vibration of Si–O–Si (O represents bridge oxygen), and the bending vibration of SiO_3 groups. Especially for the infrared acoustic mode calculation of $Ca_2ZnSi_2O_7$, it was shown that the maximum contribution to the harmonic oscillator strength ($\Delta\varepsilon$ = 1.497) comes from the *E* mode, which is determined by the bending mode of δ(SiOSi), the bending mode of SiO_3 groups δ(SiO_3), and the symmetric stretching mode of [CaO_8] T'(Ca^{2+}). This result also indicates that Si–O bonds have a significant impact on intrinsic dielectric properties, thus, the bond property parameters can be correlated with microwave dielectric properties [58]. Meanwhile, Jing's team used first principles calculations to demonstrate that the $E_{u(4)}$ mode at 220 cm^{-1} and $E_{u(5)}$ mode at 241 cm^{-1} reflect the octahedral vibration of [TaO_6], where the movement of Ta relative to O and the vibration of oxygen polyhedra contribute 50% of the dielectric constant and 90% of the dielectric loss in the complex perovskite $Ba(Mg_{1/3}Ta_{2/3})O_3$ system [59]. This conclusion is also aligned well with the P–V–L bond theory calculation that Ta–O bonds make majority contribution to the bond susceptibility and lattice stability.

The $U_{lattice}$ is crucial in diverse thermodynamic analysis of the stability of ionic crystals, which refers to the energy absorbed when completely splitting the ionic crystal into gaseous

ions. Under the P–V–L theoretical framework, it can be used to measure the strength of chemical bonds within crystals and the overall stability of the lattice. The higher the lattice energy, the tighter the binding between ions, and the more stable the lattice structure [60]. The lattice stability is found closely associated with $Q \times f$ value in several systems, as detailed in **Table 2** [45, 61-76].

Table 2. Reported ceramics and description of the correlation between $U_{lattice}$ and $Q \times f$ value

ε_r	System	$Q \times f$ value	Description of the correlation between lattice energy and $Q \times f$ value	Ref.
4.90	$Mg_2Al_4(Si_{1-x}Ge_x)_5O_{18}$	128,200 GHz (improved)	Enhancement of lattice energy, covalent bonding, and hexagonal ring symmetry after substitution	[61]
5.04~5.26	$LiLn(PO_3)_4$ (Ln = La, Sm, Eu)	41,607~75,968 GHz	The increase in $Q \times f$ value is attributed to the increase in packing fraction, U_{total} and U_{P-O}	[62]
5.25	$LiRE(PO_3)_4$ (RE = Pr, Nd)	42,939 GHz for $LiPr(PO_3)_4$ 65,718 GHz for $LiNd(PO_3)_4$	The enhancement of $Q \times f$ value in $LiNd(PO_3)_4$ is attributed to the total $U_{lattice}$ and packing fraction	[63]
6.03	$CaB_{2+x}O_{4+3x/2}$	12,832 GHz → 37,962 GHz	The $[BO_3]$ group is a bridge connecting the $[CaO_8]$ group and U_{B-O} contributes immensely to stability	[64]
7.13	$LiMg_{0.9}Zn_{0.06}Ni_{0.04}PO_4$	153,500 GHz (improved)	U_{P-O} plays a decisive role in the $Q \times f$ value	[65]
7.43	$BaZn_{0.94}Ni_{0.06}P_2O_7$	102,538 GHz (improved)	The optimized $Q \times f$ value stems from the increased U_{P1-O} and U_{Zn-O} and the larger band gap	[66]

11.4	$Nd_2Zr_3(MoO_4)_9$	186,300 ± 8900 GHz (($Bi_{0.5}Ta_{0.5}$)$^{4+}$, improved)	Lattice energy associated with the Mo(2)–O(5) bond closely parallels the $Q\times f$ values	[67]
14.6	ZnV_2O_6	46,000 GHz	The U_{V-O} dominates the total lattice energy, which is the primary reason for the maximum $Q\times f$	[68]
22~24	Y_2MgTiO_6	74,821 GHz (Nd^{3+}, improved) 67,068 GHz (Sm^{3+}, improved)	Doping ions optimize the $Q\times f$ value by regulating the $U_{lattice}$	[69]
25~27	$AZrNb_2O_8$ (A=Zn, Co, Mg, Mn)	52,000~52,500 GHz	The $Q\times f$ value of the ceramics could be predicted by the $U_{lattice}$	[70]
24.58~ 27.27	ATa_2O_6 (A = Mg, Ni)	27,610~109,203 GHz	Ta–O bonds contribute the most to the lattice stability	[71]
39~44	$A_{0.75}Ti_{0.75}Ta_{1.5}O_6$ (A=Ni, Co, Zn, Mg)	16,796~25,051 GHz	The $Q\times f$ value is correlated with the lattice energy of Ta–O bond	[72]
35.96~ 40.31	$Zn_{0.5}Ti_{0.5}NbO_4$ (Co^{2+}/Ta^{5+} doping)	24,573~·43,642 GHz	The variation of $Q\times f$ value is closely related with the total $U_{lattice}$ and average grain size	[45]
45.25	$Ba_{1-x}Sr_x(Zn_{1/3}Nb_{2/3})O_3$	72,704 GHz (improved)	The full width at half-maximum and lattice energy jointly contributed to improving the $Q\times f$ value	[73]
34.81~ 70.8	$Co_{0.5}(Ti_{1-x}Sn_x)_{0.5}NbO_4$	9528~12,479 GHz	The increase of dielectric loss is attributed to the decrease of total $U_{lattice}$	[74]
75.9	$Zn_{0.15}Nb_{0.3-x}Ta_xTi_{0.55}O_2$	22,050 GHz (improved)	$U_{lattice}$ is important to understand the variations of intrinsic losses	[75]
127	$SrTiO_3$ (Ce and Al/Ta codoping)	16,367 GHz (improved)	Co-doping enhances the $U_{lattice}$, providing an intrinsic explanation for the improvement in the $Q\times f$ value	[76]

Based on Eqs. 35-39, a comparison between the theoretical and experimental α_L values is presented in **Fig. 5.** Although the theoretical predictions for most crystals exhibit good agreement with experimental data, notable deviations exist for some. These discrepancies are attributed to mechanisms not fully captured by bonding considerations alone, such as the rotation of polyhedra within the crystal structure, which can lead to abnormal thermal expansion. Previous study indicated that the thermal expansion in quartz crystals is largely driven by the rotation of [SiO_4] tetrahedra [50].

The P–V–L bond theory provides a quantitative tool for understanding the structure performance relationship by decomposing macroscopic properties into microscopic chemical bonds. Although there are limitations in dealing with extremely complex systems or special physical mechanisms such as abnormal thermal expansion, it has become an important tool of analyzing microwave dielectric ceramics, in terms of covalent properties, lattice energy, dielectric response, and thermal properties through mutual verification with experimental data and first principles calculations.

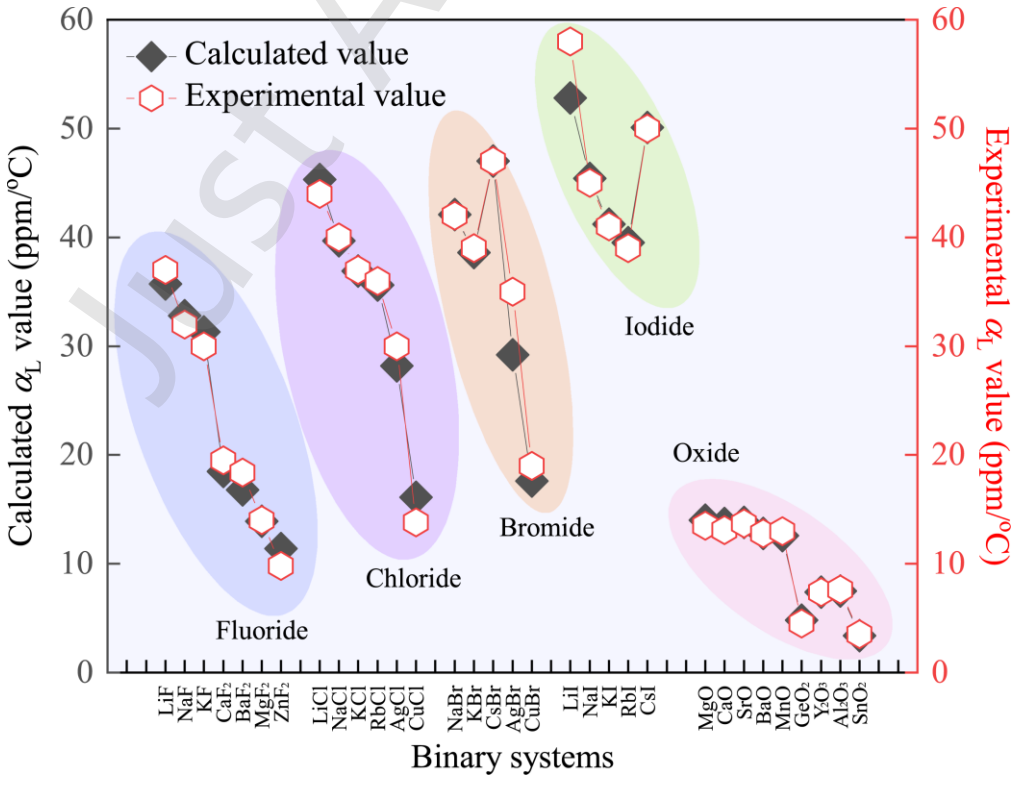

Figure 5. Comparisons between calculated and experimental α_L value.

Despite its wide applicability, the P–V–L bond theory has several inherent limitations when applied to complex multi-component microwave dielectric ceramics. Firstly, the accuracy of bond characteristics relies heavily on high-quality crystal structure refinements from X-ray or neutron diffraction. For systems with significant atomic disorder, non-stoichiometry, or poorly crystallized phases, the derived bond characteristics may carry substantial uncertainty since the decomposition of a multi-component crystal into binary A_mB_n units is not strictly unique; different decomposition strategies can yield slightly different bond ionicity or lattice energy values, introducing ambiguity in comparative studies. Also, the P–V–L bond theory is essentially static and electronic-structure-based, capturing the ground-state bonding characteristics but not explicitly accounting for anharmonic lattice vibrations, phonon damping, or temperature-dependent effects such as rattling or phase transitions, which are known to critically influence microwave dielectric properties. Following that, the P–V–L framework treats the perfect crystal lattice and does not incorporate the contributions of extrinsic defects, such as oxygen vacancies, grain boundaries, and ordered domains that often affect the measured $Q \times f$ value. Consequently, while the P–V–L theory provides valuable semi-quantitative insights into bond-ionicity, lattice energy, and polarizability trends, its predictions should be interpreted in conjunction with other complementary approaches to achieve a more holistic understanding of microwave dielectric behavior.

2.2.2 Lattice Dynamics

Lattice dynamics studies the influence of lattice vibrations on the physical properties of crystals. A deeper understanding of the physical properties of crystals can be achieved by studying the relationship between atomic vibration modes and properties [77]. Addressing the limitations of traditional XRD in detecting lattice dynamic behavior and directly analyzing atomic vibration modes, a Raman scattering coupled with Infrared reflection and phonon spectrum calculation tripartite characterization system is established. Through precision polishing of sample surfaces, high energy resolution laser excitation (0.1 cm^{-1}), low-temperature/polarization measurements,

and rapid data acquisition (~5 s), background scattering was effectively suppressed and characteristic peak separation enhanced, achieving a detection limit for impurity phases as low as 10^{-5} mol/cm^3. Infrared reflectance spectra were acquired via segmented measurement (50~400 cm^{-1} and 370~5000 cm^{-1}) followed by splicing, with the 100~1200 cm^{-1} range, less affected by multiple reflections, selected for analysis. A low excitation power of 5 mW was employed to avoid sample damage and signal saturation. This system combines the strengths of Raman spectroscopy in detecting non-polar vibrations, infrared spectroscopy in probing polar dielectric responses, and first-principles phonon calculations in assigning vibration modes and providing theoretical parameters such as frequencies, atomic displacement vectors, and phonon density of states. The integrated approach enables comprehensive and precise analysis of the lattice dynamics of microwave ceramics, offering critical experimental and theoretical support for elucidating the structure–phonon–property correlation mechanism from the perspective of vibrational spectroscopy.

In the 1970s and 1980s, researchers such as Petzelt and Wakino pioneered the application of vibrational spectroscopy to dielectric ceramics. However, early work was largely confined to phase identification and structural characterization, lacking in-depth analysis of phonon features or the establishment of intrinsic correlations between phonon behavior and material properties. Unlike organic materials, which exhibit distinct functional group fingerprints (e.g., hydroxyl, carboxyl), inorganic non-metallic oxides, particularly microwave dielectric ceramics, present formidable challenges in vibrational spectroscopy. These include complex cationic coordination in the lattice, high structural diversity arising from processing and compositional variations, and pronounced spectral phenomena such as multimode coupling, peak overlap, and broadening. As a result, accurate identification and systematic interpretation of lattice vibration peaks in Raman and infrared spectra have long remained difficult. This bottleneck in phonon characterization has constrained the development of a lattice dynamics based understanding and tailored control of dielectric properties.

Lattice vibrations are inherently governed by symmetry. Wave vectors define distinct symmetry coordinates within the Brillouin zone, linking vibrational behavior to the intrinsic relationship between crystal structure and dielectric properties, key to analyzing the phonon characteristics of materials where cations have complex oxygen environments in the spatial lattice. To overcome severe peak overlap and ambiguous mode assignment in inorganic non-oxide and oxide ceramics, a group theory driven phonon analysis framework integrating crystal structure analysis, symmetry matching, and first-principles calculations were proposed. By combining structural refinement, space group symmetry, and DFT derived vibrational parameters, including frequencies, displacement vectors, and irreducible representations, the method enables systematic identification and classification of phonon modes according to their symmetry (e.g., infrared-active F_{1u}, Raman-active A_{1g}). This approach not only assigns spectral peaks to specific bond vibrations and atomic motions, but also visualizes three-dimensional lattice dynamics, such as vibration type, intensity, frequency shift, full width at half maximum (FWHM), and spectral peak evolution, providing a robust theoretical basis for spectroscopic studies of complex oxides. In other words, addressing the problem of traditional spectral identification relying on empirical formulas, the team established a five-fold verification method of structure refinement, crystal field effect, symmetry matching, group theory symmetry analysis, and first-principles verification, systematically improving the accuracy and reliability of phonon mode identification. Firstly, the space group was determined via crystal structure refinement. Then, crystal field effect analysis determines vibration mode attribution through splitting energy calculations, e.g., F_{2g} mode in $Ba[Mg_{(1-x)/3}Zr_xNb_{2(1-x)/3}]O_3$ splits into $A_{1g}+E_g$ in Zhang's study [78]. Followed by that, screening active modes based on the character table of the space group, e.g., 9 Raman-active vibration modes $4A_{1g}+5E_g$ and 16 infrared-active vibration modes $7A_{2u}+9E_u$ in the $(Ba_{1-x}Sr_x)(Zn_{1/3}Nb_{2/3})O_3$ system was determined [79]. Next, group theory symmetry analysis identifies active vibration modes through irreducible representation decomposition, 7 Raman-active modes and 3 infrared-active modes of

$Ba(Mg_{1/3}Ta_{2/3})O_3$ through group theory analysis, where A_{1g}(O) mode at 745 cm^{-1} was confirmed to originate from the ZrO_6 octahedron breathing vibration; Lv distinguished Raman peaks of scheelite $CaWO_4$: 82 cm^{-1} (B_g mode to Ca–O vibration), 757 cm^{-1} (A_g mode to W–O stretching), with a FWHM error < 0.5 cm^{-1} [80, 81]. Subsequent, first-principles verification uses the CASTEP module to calculate phonon dispersion curves to verify frequency accuracy (error <2%), e.g., Xiao constructed a supercell model containing 128 atoms, predicting the E_u mode (150.21 cm^{-1}) with an error controlled within ±2% compared to the experimental value (150.18 cm^{-1}) [82, 83].

Using the classical harmonic oscillator model, the intrinsic dielectric properties of microwave ceramics were fitted, enabling the dielectric response mechanism to be elucidated at the atomic and molecular level. A novel theory of phonon gradient-induced polarization was proposed, which encompasses three key components. The first one is anionic polarization. Phonon gradients drive asymmetric deformation of electron clouds around anions, generating local dipole moments that contribute 15~30% to ε_r. Following that is the ionic displacement polarization. Low-frequency phonons induce periodic cation shifts near equilibrium positions, dominating the low-frequency dielectric response in the microwave regime. Then, the interfacial relaxation polarization is also considered, where stress field gradients in grain boundary regions, induced by phonon excitation, trigger charge redistribution and relaxation, which is identified as a critical source of high-frequency dielectric loss.

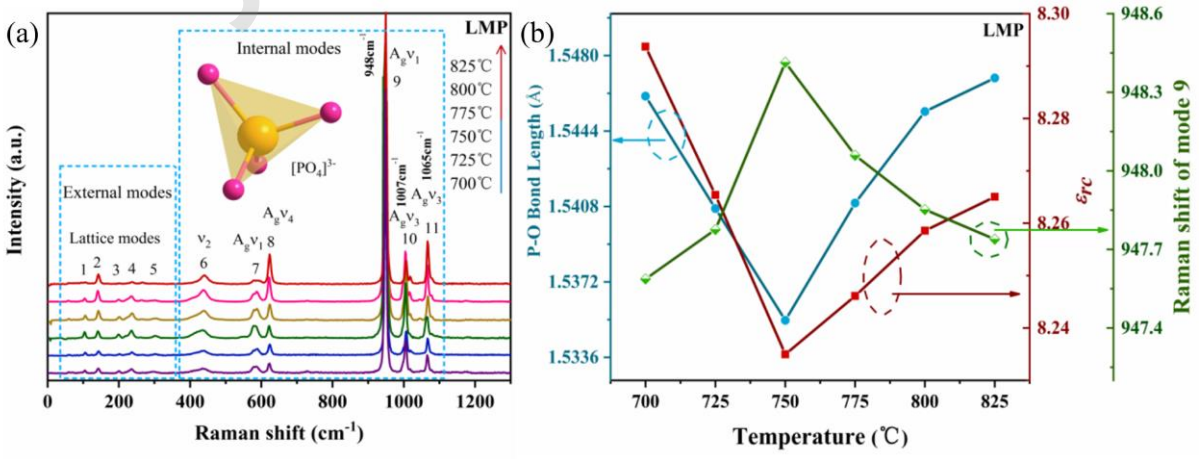

Figure 6. (a) Raman spectra of $LiNiPO_4$ ceramics at different temperatures; (b) Relationship between P–O bond length and Raman shift. Reproduced with permission from Ref. [86], © The American Ceramic Society 2019.

In the $SrWO_4$ system, an exponential correlation was established between the Raman intensity of the W–O bond stretching vibration mode (ν_3) and the dielectric loss, challenging the conventional assumption that non-polar Raman modes are uninvolved in dielectric response [84]. Similarly, in scheelite $Ca_{0.99}WO_4$ ceramics, the FWHM of the B_g (83 cm^{-1}) mode exhibited an exponential relationship with the $Q \times f$ [85]. For $BaTiO_3$ ceramics, the FWHM of the E_g mode (518 cm^{-1} assigned to Ti–O antisymmetric stretching) was positively correlated with dielectric loss, confirming lattice vibration disorder as a key microscopic loss mechanism. In $BaMoO_4$ ceramics, external modes (<500 cm^{-1}) were found to dominate $Q \times f$, with the FWHM of the E_g mode again showing an exponential dependence on $Q \times f$, further reinforcing the dominant role of low-frequency phonon damping in loss behavior. These findings provide a direct optimization criterion for quality factor enhancement. For olivine-structured $LiMnPO_4$ ceramics, internal modes (>500 cm^{-1}) govern ε_r; notably, a red shift of 0.3 cm^{-1} in the ν_1 mode corresponds to an ε_r increase of 0.08, establishing a quantitative link between vibrational frequency shift and polarization intensity. This offers cross-system validation of the energy-domain and property correlation. In a related olivine $LiNiPO_4$ system, precise analysis of the 9 characteristic Raman peaks of the $[PO_4]^{3-}$ tetrahedron revealed, for the first time, a direct linear relationship between P–O bond length and ε_r, as shown in **Fig. 6**, uncovering the structural origin of the dielectric constant at the chemical bond level [86]. Furthermore, Shi's group elucidated the coupling relationship between crystal structure and dielectric properties of $BaCu(B_2O_5)$ added $CaMgGeO_4$ ceramics based on lattice vibration [87]. Based on the crystal structure characteristics, including grain size, interface state, oxygen octahedral distortion, chemical bonding, and ordered/disordered distribution, the influence of phonon scattering, vibration frequency shift and loss is analyzed, as shown in **Fig. 7**.

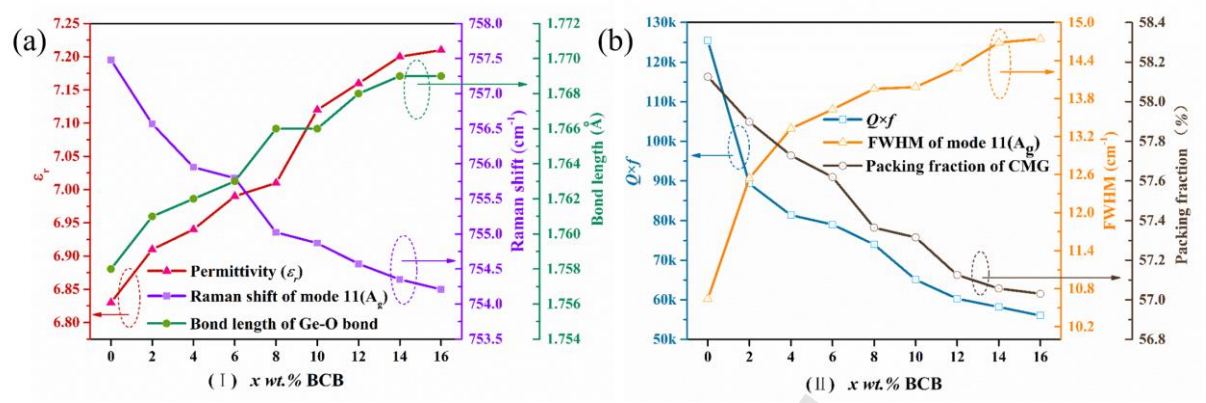

Figure 7. The coupling relationship between phonon characteristics and (a) ε_r and (b) $Q\times f$ of microwave ceramics

The frequency-dependent division of labor among phonons and their respective contributions to dielectric properties were systematically clarified. Taking infrared-active vibrational modes in $Ca_{1+x}WO_4$ ceramics as a case study, fitting results demonstrate that low-frequency acoustic branch vibrations (< 400 cm^{-1}, e.g., the 67.6 cm^{-1} mode) account for up to 68% of dielectric loss, whereas high-frequency optical branch vibrations (800~1200 cm^{-1}, e.g., the 890.8 cm^{-1} assigned to W–O stretching mode) dominate the dielectric constant, contributing as much as 72%. This reveals a clear functional division: low-frequency vibrations govern loss, while high-frequency vibrations drive polarization.

The microscopic origin of the τ_f was also elucidated in terms of lattice dynamics. A linear correlation was established between τ_f and the temperature drift rate of lattice vibrational frequency ($d\omega/dT$). For instance, when the drift rate of the Mg–O bond vibration decreased from -0.08 cm^{-1}/°C to -0.04 cm^{-1}/°C, the τ_f value improved from -59.06 ppm/°C to -2.27 ppm/°C. Furthermore, it was clarified that the dielectric response of $Ca_{1+x}WO_4$ ceramics originates from distorted [WO_6] octahedral vibrations, a finding that challenges the long-held view that infrared vibration modes are relevant only to dielectric properties and bear no relation to crystal structure [88]. Together, these results affirm that microwave dielectric properties are primarily governed by phonon behavior and the ionic polarization arising from lattice vibrations.

Addressing the inability of the traditional Debye model to handle multi-mode coupling, a modified model containing the following parameters was proposed:

$$\varepsilon_{\mathrm{r}}(\omega) = \varepsilon_{\infty} + \sum_{j} \frac{S_j}{(\omega^2 - \omega_{Lj}^2) + i\gamma_j \omega} \tag{40}$$

The Four-Parameter Semi-Quantum model (FPSQ) was developed, achieving precise analysis and performance prediction of the intrinsic dielectric response of microwave ceramics. By fitting, parameters for each vibration mode are obtained: strength coefficient S_j (reflecting mode importance), resonance frequency ω_j (related to bond force constant), damping coefficient γ_j (characterizing energy dissipation). In the far-infrared band, the FPSQ model has been successfully applied to the fitting of intrinsic dielectric properties and guidance of process optimization for multiple ceramic systems. In the $LiMg_{1-x}Ni_xPO_4$ system, the error between fitted and measured values is <5% when x = 0.1[89]. In $Ca_{0.99}WO_4$ ceramic, the ε_r predicted by the FPSQ model (10.19) has an error <3% compared to the experimental value, and the loss factor coincidence reaches 92% [85]. In $BaMoO_4$ ceramic, the phonon electromagnetic wave absorption characteristics are revealed, by using Kramers–Krönig conversion to obtain phonon parameters, the complex dielectric constant response behavior of infrared vibration modes was analyzed, and the linear reaction function of physical systems was interpreted. It was believed that the $Q \times f$ depends on the chemical bond in the oxygen octahedron. This indicates that the dielectric properties of ceramics in the microwave frequency range mainly come from internal ion displacement polarization and lattice vibration, as shown in **Fig. 8** [83]. These all demonstrate the guiding value of theory for processes.

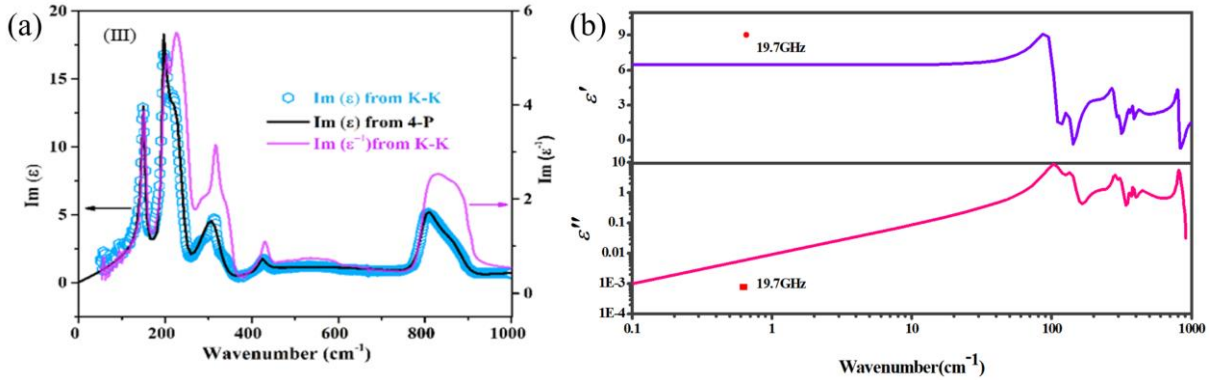

Figure 8. (a) Fitting of infrared reflectance spectrum using FPSQ model; and (b) Real and imaginary parts of complex dielectric function. Reproduced with permission from Ref. [83], © The Chinese Ceramic Society and Elsevier B.V. 2018.

Compared to the classical Debye model, FPSQ improves fitting accuracy by an average of about 42% when dealing with multi-phonon coupling materials in the<10 THz frequency band, significantly enhancing the description capability for dielectric behavior of complex systems. This model not only provides a reliable theoretical tool for extracting intrinsic dielectric parameters from vibrational spectroscopy data but also embodies the research paradigm of phonon theory guiding process optimization, strongly supporting the rational design and controllable preparation of high-performance microwave ceramics.

Raman scattering, infrared reflection spectroscopy and first-principles phonon calculations are highly synergistic and complementary, forming a robust framework for precise characterization of lattice vibrations in microwave ceramics. Raman scattering is sensitive to nonpolar optical phonons, enabling identification of crystal symmetry, lattice distortion and trace impurities, and revealing vibrational disorder. Infrared reflection spectroscopy targets polar vibrations and dielectric responses, allowing direct characterization of ionic polarization–related active modes and quantitative extraction of intrinsic dielectric parameters.These two experimental methods cover the full vibrational spectrum and overcome mode overlap and ambiguous assignment encountered in single-spectroscopy approaches. Phonon calculations, based on space group symmetry and group-theory analysis, provide theoretical vibrational frequencies, atomic displacement vectors and mode symmetries, supporting accurate

assignment and calibration of Raman and infrared peaks. Together, they establish a closed loop of experimental detection, theoretical identification and cross-validation, enabling reliable correlation between lattice dynamics and dielectric performance for structure–property relationship studies.

By accurately assigning phonon modes and establishing quantitative correlations between spectral features, lattice characteristics, and dielectric performance, the underlying response mechanisms and their structural sensitivities can be elucidated at the atomic level. This enabled the clarification of composition–process–structure–property relationships from a lattice-dynamics perspective.

2.2.3 A defect perspective on microwave dielectric loss

Controlling the dielectric loss is a critical objective in microwave dielectric ceramics, and has long been a central focus for both researchers and industry. Based on the physical origins of dielectric loss, it has traditionally been classified into intrinsic and extrinsic losses. Intrinsic loss arises from the anharmonic lattice vibrations of a perfect crystal, whereas extrinsic loss originates from various "imperfect" factors, such as porosity, secondary phases, grain boundaries, lattice defects, etc [90, 91]. Since the earliest microwave dielectric ceramics were Ti-containing materials such as TiO_2 and $BaTi_4O_9$ [92-95], it was naturally observed that Ti^{4+} undergoes partially reduction during high-temperature sintering, generating oxygen vacancies:

$$2\mathrm{Ti}_{\mathrm{Ti}}^{\times} + \mathrm{O}_{\mathrm{O}}^{\times} \rightarrow 2\mathrm{Ti}_{\mathrm{Ti}}' + V_{\mathrm{O}}^{\cdot\cdot} + \frac{1}{2}\mathrm{O}_2 \uparrow \quad (41)$$

This process can be visually assessed through color changes (called color centers) in the sintered ceramics. Based on early empirical knowledge, oxygen vacancies were believed to increase the dielectric loss of ceramics, which could be controlled through process optimization. This understanding has continued to influence research on microwave dielectric ceramics ever since. In addition, it was recognized early on that order–disorder transitions occur in complex perovskite systems such as $Ba(Zn_{1/3}Ta_{2/3})O_3$ (BZT) ceramics [96]. In some systems, the

ordering degree shows a clear positive correlation with the $Q \times f$ value, suggesting that domain structures also affect dielectric loss. In summary, the contribution of multiscale defects to microwave dielectric loss has consistently attracted considerable research attention. In recent years, with the continuous advancement of characterization techniques, a deeper understanding of the dielectric responses of defects has been achieved. Therefore, this section reviews the mechanisms underlying microwave dielectric loss and its regulation from a defect perspective.

The influence of macroscopic defects on microwave dielectric properties is readily quantifiable. For instance, pores and secondary phases can both be regarded as acting through a two-phase composite effect, which is generally described by mixing rules. The mixing rule for ε_r can be expressed as:

$$\varepsilon_r^a = V_1 \varepsilon_{r1}^a + V_2 \varepsilon_{r2}^a \tag{42}$$

where ε_{r1} and ε_{r2} are the ε_r of the ceramic matrix and the secondary phases, respectively; V_1 and V_2 are the volume fraction of the secondary phase; and a is a constant. The parallel and series models are obtained when a = 1 and -1, respectively. The logarithmic mixing rule is obtained when a approaches zero:

$$\log \varepsilon_r^a = V_1 \log \varepsilon_{r1} + V_2 \log \varepsilon_{r2} \tag{43}$$

The mixing rule for dielectric loss (or equivalently, the Q value) is more complex in form. Chen et al. [97] and Cao et al. [98] proposed respective expressions, with the one derived by Cao et al. [98] given as follows:

$$Q^{-1} = \frac{V_1 \varepsilon_{r1}^a Q_1^{-1} + V_2 \varepsilon_{r2}^a Q_2^{-1}}{V_1 \varepsilon_{r1}^a + V_2 \varepsilon_{r2}^a} \tag{44}$$

These models agree well with experimental results from some two-phase composite systems like $ZnNb_2O_6$-TiO_2 and $Mg_{0.95}Zn_{0.05}TiO_3$-$Ca_{0.6}La_{0.8/3}TiO_3$, as shown in **Fig. 9(a)** [97]. The parameter a in Eq. 43 was found to have a clear physical meaning, representing the connectivity of the secondary phase. It was validated by finite element simulations: a larger a value indicates a more uniform electric field distribution within the composite ceramics, as shown in **Fig. 9(b)**

[98]. However, they fail to explain why the $Q \times f$ value of the composite ceramics is lower than that of both single phases, which likely arises from the interface or the subtle compositional diffusion between the two phases.

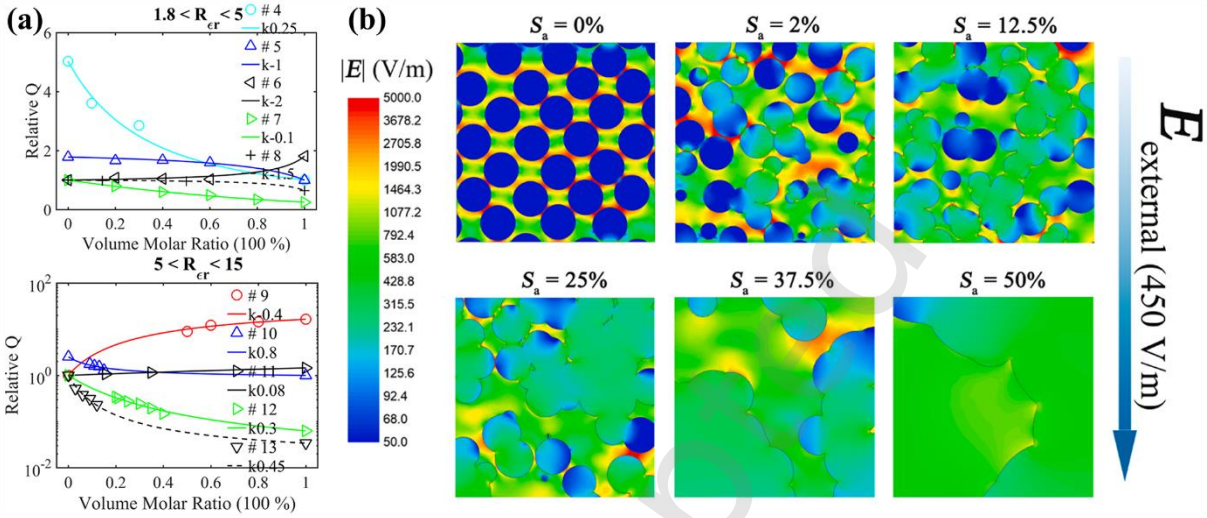

Figure 9. Effect of secondary phases and pores on the microwave dielectric loss. (a) The comparison between the reported relative Q values (Q_2/Q_1) and calculation ones, where $R_{\varepsilon r}$ represents $\varepsilon_{r2}/\varepsilon_{r1}$, and k represents parameter a in Eqs. 42 and 44. The order number #4 ~ #13 means $Ca_4MgNb_2TiO_{12}$–$CaTiO_3$, $ZnNb_2O_6$–TiO_2, $ZnTa_2O_6$–TiO_2, $BaNd_2Ti_4O_{12}$–$BaZn_2Ti_4O_{11}$, $Li_2ZnTi_3O_8$–TiO_2, $Mg_4Nb_2O_9$–$CaTiO_3$, $BaMg_2V_2O_8$–TiO_2, $ZnMoO_4$–TiO_2, $Mg_{0.95}Zn_{0.05}TiO_3$–$Ca_{0.6}La_{0.8/3}TiO_3$, and $Mg_2Ti_{0.95}Sn_{0.05}O_4$–$CaTiO_3$, respectively [97]. (b) Simulated electric field distribution in $CaTiO_3$ porous ceramics varied with the ceramic connectivity S_a [98]. Reproduced with permission from Ref. [98], © Acta Materialia Inc. and Elsevier Ltd. 2023.

Grain boundary is another type of defect that has been widely discussed in the literature. Ceramics with larger grains and fewer grain boundaries are generally considered to exhibit lower dielectric loss, as defects such as dangling bonds tend to accumulate at grain boundaries. A typical observation is that the dielectric loss of polycrystalline ceramics is significantly higher than that of single crystals. However, a study published by Alford et al. in 2009 [99] suggested that the dielectric loss contributed directly by grain boundaries themselves is likely negligible. The microwave dielectric properties of single-crystal and bi-crystal MgO (at 9.37 GHz) showed that the only difference was that the bi-crystal exhibited a loss peak at low temperatures (~45 K), which was attributed to the relaxation of defect dipoles. It was implied that clean grain

boundaries have almost no impact on microwave dielectric properties at room temperature. Therefore, the discussion regarding the grain boundaries or grain size should be based on further characterization of impurity segregation and lattice defects at the grain boundaries, while also carefully excluding other factors such as densification and oxygen loss at high temperatures.

As medium-range defects, domain structures also exert a critical influence on microwave dielectric properties. Unlike the polar domains commonly found in ferroelectric ceramics (which would introduce significant relaxation loss when switched in the microwave band), microwave dielectric ceramics are typically nonpolar. In this context, the primary focus has been on nonpolar ordered domains in complex perovskites. BZT is a widely used commercial microwave dielectric ceramic. Early studies found that prolonged sintering or annealing could induce a 1:2 ordered structure, leading to a marked improvement in the $Q\times f$ value [96, 100]. Slight non-stoichiometry design or minor cation substitution can also induce order–disorder transitions, thereby enabling the tuning of $Q\times f$ values [101, 102]. Chen et al. [103-112] conducted extensive and in-depth research on order–disorder engineering in complex perovskite microwave dielectric ceramics. They discovered that the order degree, the ordered domain size and distribution, and the domain boundary structure influence the $Q\times f$ value together, as shown in **Figs. 10(a-d)**, which can all be tailored through the design of sintering and annealing processes [110]. Through ordered-domain engineering, a series of ceramics with excellent microwave dielectric properties have been developed, such as $Ba[(Zn_{0.8}Mg_{0.2})_{1/3}Nb_{2/3}]O_3$ ($Q\times f$ increased from 51,000 GHz to 118,000 GHz) [110], $Ba(Mg_{1/3}Ta_{2/3})O_3$ ($Q\times f$ increased from 30,700 GHz to 71,900 GHz) [111], and CuO-doped $Ba(Co_{0.7}Zn_{0.3})_{1/3}Nb_{2/3}O_3$ ($Q\times f$ increased from 21,200 GHz to 69,300 GHz) [113]. The ordered structure in complex perovskites also contributes to enhanced thermal conductivity and breakdown strength, and plays a certain role in adjusting τ_f [108, 109, 111]. Other types of domain structures have gradually been identified in microwave dielectric ceramics. For example, Guo et al. observed crystallographic shear planes and their clusters in rutile TiO_2

ceramics, as shown in **Figs. 10(e-g)**, which were strongly depended by sintering temperature [114]. These defects greatly affect lattice vibration behavior, resulting in a sharp decrease in $Q \times f$ value. Wu et al. [115] observed structures resembling ferroelastic domains in $Sm(Nb_{0.7}P_{0.3})O_4$ ceramics, as shown in **Figs. 10(h-i)**, with their effect on dielectric properties remaining unclear. Furthermore, the high-entropy strategy is widely considered effective for reducing microwave dielectric loss [116-118]. However, unlike in ferroelectric energy-storage ceramics, no analogous domain behavior has been observed in high-entropy microwave dielectric ceramics, and the underlying mechanism still requires further investigation. Nevertheless, it is clear that high entropy contributes to phase stability and sluggish diffusion effects (leading to reduced grain size) in microwave dielectric ceramics. The chemical disorder inherent in high-entropy design has even been found to enhance the temperature stability of the 1:2 ordered phase in complex perovskites [112].

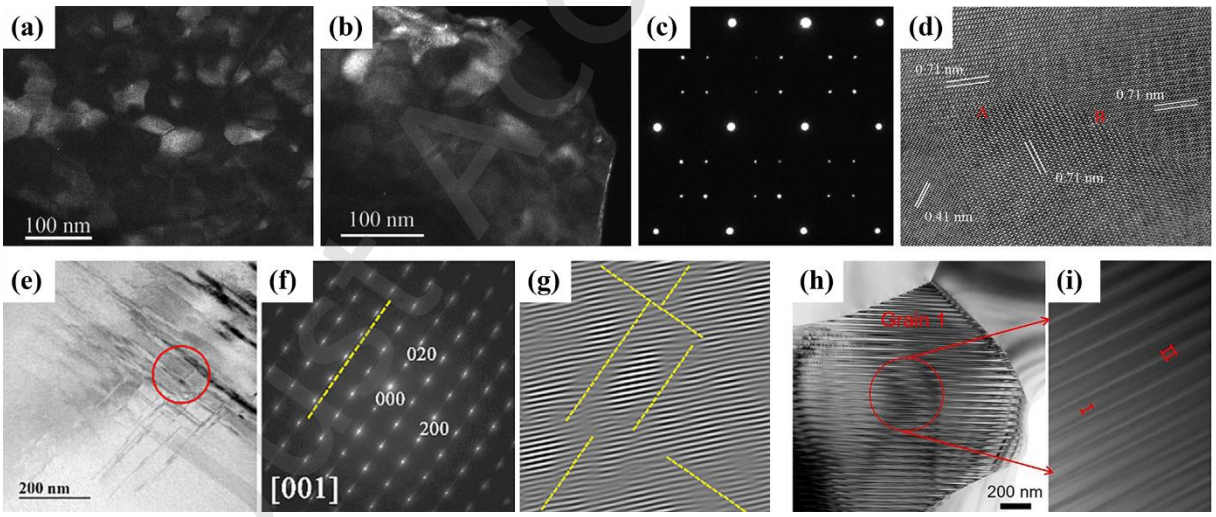

Figure 10. Domain structures in microwave dielectric ceramics. (a-d) Domain structures in $Ba[(Zn_{0.8}Mg_{0.2})_{1/3}Nb_{2/3}]O_3$ ceramics: dark-field TEM images of the ceramics annealed at (a) 1350 °C for 24 h and (b) 1450 °C for 24 h; (c) SAED patterns of the ceramics annealed at 1350 °C for 24 h along $[110]_c$; (d) HRTEM images of the ceramics annealed at 1350 °C for 24 h viewed along $[110]_c$ [110]. Reproduced with permission from Ref. [110], © The American Ceramic Society 2023. (e-g) Domain structures in rutile TiO_2 ceramics sintered at 1150 °C in air: (e) morphology, (f) SAED patterns, and (g) FFT-filtered (110) crystal face morphology [114]. Reproduced with permission from Ref. [114], © The American Ceramic Society

2025. (h-i) Domain structures in $Sm(Nb_{0.7}P_{0.3})O_4$ ceramics [115]. Reproduced with permission from Ref. [115], © Wiley-VCH GmbH 2025.

The influence of point defects on dielectric loss involves the most complex mechanisms. Such defects typically arise from substituted ions, non-stoichiometry, or valence changes during high-temperature sintering, with oxygen vacancies and defect dipoles being the most frequently discussed. In particular, the notion that "oxygen vacancies degrade the $Q \times f$ value" has become a widely accepted view, yet direct evidence has remained elusive. This is partly because the defect concentration in microwave dielectric ceramics is extremely low, making accurate characterization challenging with conventional techniques such as TEM, XPS, and EPR. Moreover, isolating the specific contribution of point defects to dielectric loss is very difficult. Far-infrared reflection spectra are commonly considered to reflect "intrinsic" dielectric responses, but point defects such as oxygen vacancies inevitably influence anharmonic lattice vibrations and thereby alter the dielectric response in the infrared range. This means that the so-called "intrinsic" response is inevitably mixed with "extrinsic" contributions. In principle, infrared spectroscopy measurements conducted near 0 K could help separate the contributions of the lattice and point defects due to their different temperature dependencies. However, such experiments are technically challenging, and the results have shown limited consistency with theoretical predictions [119, 120]. With the application of new characterization techniques such as thermally stimulated depolarization currents (TSDC) and terahertz time-domain spectroscopy (THz-TDS) to microwave dielectric ceramics, the mechanisms by which point defects affect microwave dielectric loss have become increasingly clear, providing important guidance for the design of low-loss microwave dielectric ceramics.

TSDC is a semi-quantitative and highly sensitive technique for charged defect characterization. During the measurement shown in **Fig. 11(a)**, the ceramic sample is first polarized at a polarization temperature (T_p) under a polarization field (E_p) for a certain duration (t_p). It is then rapidly cooled to "freeze" the polarized state. After removing the electric field,

the depolarization current is measured while the sample is heated at a constant rate [121]. Based on how the relaxation peaks vary with T_p and E_p, the relaxation process can be identified as originating from defect dipoles, trapped charges, or space charges (typically oxygen vacancies). For example, the relationship between the depolarization current (J_D) of defect dipoles and measured temperature (T) can be described by the following equation [122, 123]:

$$J_D = \frac{N\mu^2 E_p}{k_B T_p \tau_0} \exp\left(-\frac{E_a}{k_B T}\right) \exp\left[-\frac{1}{\beta\tau_0}\int_{T_0}^{T} \exp\left(-\frac{E_a}{k_B T'}\right) dT'\right] \quad (45)$$

where N, μ, k_B, τ_0, E_a, and β represent the dipole density, the electric dipole moment, the Boltzmann constant, the pre-exponential factor, the activation energy, and the heating rate. It can be derived from Eq. 44 that the E_a value can be calculated using the initial rise portion of J_D, which helps to further identify the defect type [122]:

$$\ln|J_D| = \text{const.} - \frac{E_a}{k_B T} \quad (46)$$

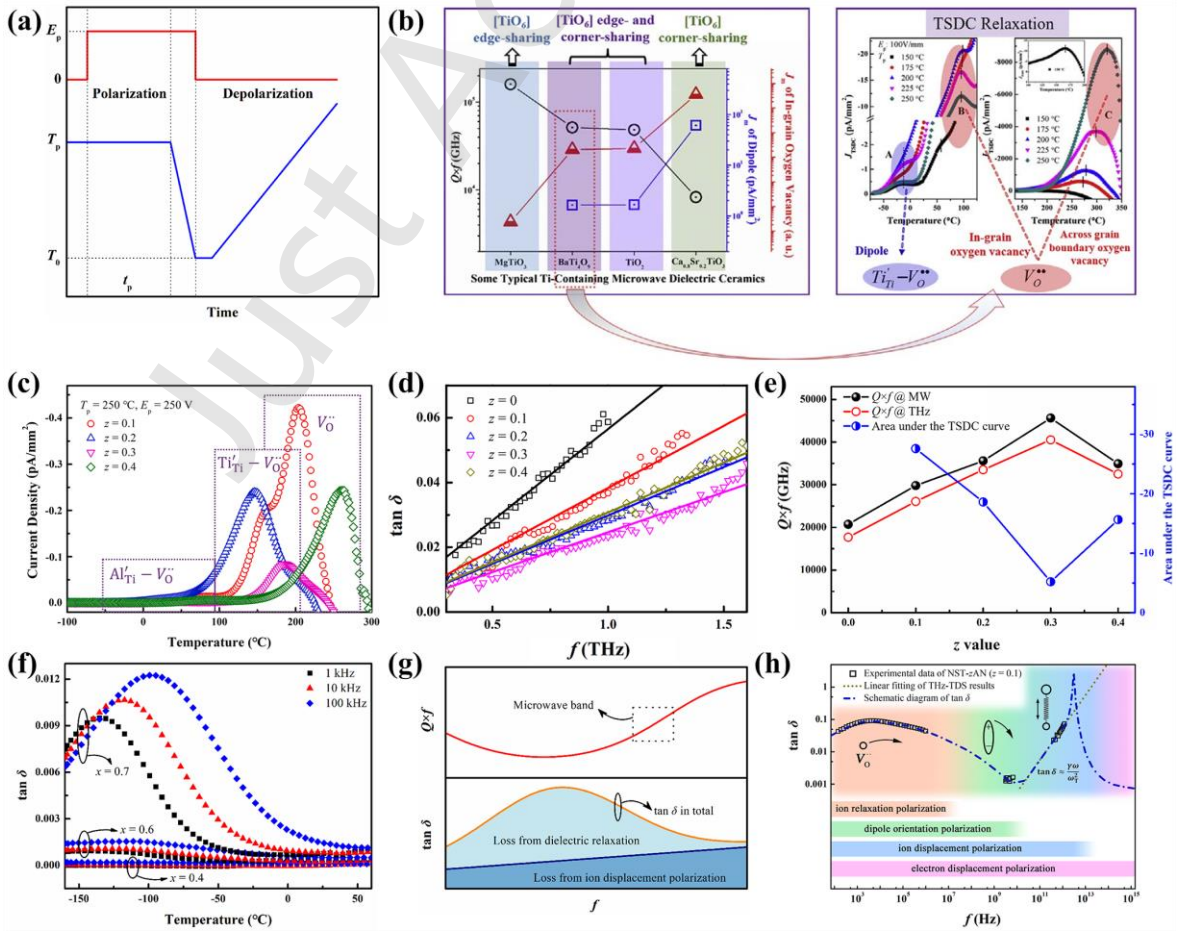

Figure 11. Effect of point defects on the microwave dielectric loss. (a) Measurement process of TSDC. (b) TSDC and $Q\times f$ values of Ti-containing ceramics [124]. Reproduced with permission from Ref. [124], © Elsevier Ltd. 2017. (c-e) TSDC, THz-TDS, and their relationship of $Ca_{0.6}Sm_{0.27}Ti_{1-z}Al_{4z/3}O_3$ ceramics, respectively [125]. Reproduced with permission from Ref. [125], © Elsevier Ltd. 2022. (f) Low-temperature and low-frequency dielectric relaxations in $Ca_{1-x}Sm_{2x/3}TiO_3$ ceramics. (g) Diagram of the frequency dispersion in $Q\times f$ values [126]. Reproduced with permission from Ref. [126], © Elsevier Ltd. 2025. (h) Illustration of the dielectric response and polarization mechanisms of $Na_{1/2}Sm_{1/2}Ti_{1-z}(Al_{1/2}Nb_{1/2})_zO_3$ ($z = 0.1$) ceramics [127]. Reproduced with permission from Ref. [127], © Acta Materialia Inc. and Elsevier Ltd. 2023.

TSDC technique was first introduced into the study of dielectric ceramics by Randall et al. in 2008 [128]. Since 2014, Yue and Zhang, et al. began reporting TSDC investigations on microwave dielectric ceramics [107, 124, 125, 127, 129-138]. Combining TSDC with other characterization methods such as dielectric spectroscopy and impedance spectroscopy, semi-quantitative defect analysis has been achieved for common microwave dielectric ceramic systems, including titanates, niobates, and silicates. It has been observed that among ceramics with similar structures or compositions, a higher defect concentration tends to correlate with a lower $Q\times f$ value. Taking ceramics containing $[TiO_6]$ octahedra as an example, the concentrations of oxygen vacancies and defect dipoles (as indicated by TSDC peak intensity), as well as the $Q\times f$ values, show a strong correlation with the connectivity of the $[TiO_6]$ octahedra, as shown in **Fig. 11(b)**. $MgTiO_3$ ceramics, featuring edge-sharing $[TiO_6]$ octahedra with the strongest bonding configuration, exhibit low defect concentrations and high $Q\times f$ values. $BaTi_4O_9$ and TiO_2 ceramics, where both edge-sharing and corner-sharing configurations coexist, show moderate defect concentrations and $Q\times f$ values. In contrast, $Ca_{0.8}Sr_{0.2}TiO_3$ ceramics, characterized by corner-sharing octahedra with the weakest bonding configuration, display the highest defect concentrations and the lowest $Q\times f$ values [124, 131-133]. These findings build upon the established understanding that "oxygen vacancies degrade the $Q\times f$ value", offering a further perspective: charged defects are closely related to the interionic bonding strength and likely influence microwave dielectric loss by affecting lattice vibration behavior.

In recent years, terahertz technology has provided new support for the relationship between defects and dielectric loss in microwave dielectric ceramics. The terahertz properties of microwave dielectric ceramics have attracted attention due to the potential application prospects of 6G technology. Although a fundamental breakthrough in low-loss ceramic materials for the terahertz band has not yet been achieved, the substantial number of reported terahertz data has prompted a deeper understanding of the mechanisms underlying dielectric loss. According to the classical harmonic oscillator model, when the frequency (ω) is much lower than ω_T (referred to as the intrinsic frequency of phonon vibration), the dielectric loss originating from ionic displacement polarization satisfies the following relationship:

$$\tan\delta \approx \frac{\omega\gamma}{\omega_T^2} \tag{47}$$

where γ represents the damping factor of phonon vibration. Since the ω_T of ceramics generally lies in the infrared band, the dielectric loss spectra in the terahertz band can be fitted linearly through the origin based on Eq. 46. The slope of the fitted line reflects the magnitude of γ, and the reciprocal of the slope corresponds to the $Q\times f$ value. For most microwave dielectric ceramics, the measured $Q\times f$ values in the microwave and terahertz bands are relatively close, suggesting that the dielectric loss in both bands originates from anharmonic lattice vibrations associated with ionic displacement polarization. Taking $Ca_{0.6}Sm_{0.27}Ti_{1-z}Al_{4z/3}O_3$ ceramics as an example, as shown in **Figs. 11(c-e)**, the difference in $Q\times f$ values between the two bands is within 10%, and TSDC measurements reveal a clear negative correlation between charged defect concentration and $Q\times f$ value. This is attributed to the substitution of Al^{3+}, which results in shorter bond lengths and a more compact crystal structure, thereby inhibiting the formation of oxygen vacancies and reducing defect concentration. These factors lead to decreased damping of anharmonic lattice vibrations and consequently an increase in $Q\times f$ value [125]. A similar relationship among defects, lattice vibrations, and dielectric loss has been confirmed in systems such as Zr/Hf-substituted $Ba_4Sm_{9.33}Ti_{18}O_{54}$, $Zn_{0.17}Nb_{0.33}Ti_{0.5}O_2$, (La, Al) co-doped

$(Ba,Sr)La_4Ti_4O_{15}$, and Ge-substituted $CaMg_{0.9}Zn_{0.1}Si_2O_6$ [134, 138-140], indicating that defects influence dielectric loss by affecting lattice vibration behavior, an effect closely related to interionic bonding strength. The oxygen vacancy-affected dielectric loss is essentially analogous to other perspectives discussed in the article: the P–V–L theory suggests that lattice energy strongly affects $Q\times f$ value, fundamentally by changing anharmonic lattice vibration behavior. A strong rattling effect tend to induce low $Q\times f$ values, which also originates from weak interionic bonding that enhancing the damping of lattice vibrations. Furthermore, THz-TDS can accurately characterize the dielectric response in the low-wavenumber region of the far-infrared spectra, serving as an important complement to lattice dynamics theory.

However, some microwave dielectric ceramics exhibit frequency dispersion in $Q\times f$ values [141-143], and significant discrepancies have also been revealed between $Q\times f$ values measured in the microwave and terahertz ranges for certain systems [126, 127]. For instance, in the cubic pyrochlore $Bi_{1.5}ZnNb_{1.5}O_7$ system, Wang et al. [144] observed that its microwave dielectric loss is much higher than the values extrapolated from terahertz–far-infrared measurements, and a pronounced low-temperature dielectric relaxation was detected in the low-frequency temperature-dependent dielectric spectra. This relaxation behavior is thought to be associated with the hopping of disordered A-site cations. Such dielectric relaxation may account for the anomalously high dielectric loss or frequency dispersion of $Q\times f$ values in the microwave range. $BaZrO_3$ exhibits a $Q\times f$ value of only 5,731 GHz in the microwave band [145], which is far lower than that of other microwave dielectric ceramics with comparable permittivity. Pulphol et al. [146] also observed low-temperature dielectric relaxation in this material. Similar dielectric relaxations have been found in $Ca_{1-x}Sm_{2x/3}TiO_3$ ceramics, as shown in **Fig. 11(f)**. By combining defect characterization together with THz-TDS, this effect becomes even clearer. In $Na_{1/2}Sm_{1/2}Ti_{1-z}(Al_{1/2}Nb_{1/2})_zO_3$ ceramics, the $Q\times f$ values in the microwave and terahertz bands show opposite trends with various substitution content, and the $Q\times f$ value of the substituted ceramics exhibits frequency dispersion in the microwave range, whose mechanism is illustrated

in **Fig. 11(g)**. TSDC and dielectric spectra indicate that the reason is the relaxation behavior of new defect dipoles introduced by ion substitution, as shown in **Fig. 11(h)** [127]. Therefore, this series of dipole-like dielectric relaxations most likely contribute to the degradation of $Q \times f$ values in the microwave band.

Thus, from the perspective of point defects, microwave dielectric loss can be classified into the loss arising from ionic displacement polarization and that arising from defect relaxation, rather than a simple "intrinsic" or "extrinsic" division. Although oxygen vacancies do not participate in the polarization processes at microwave frequencies, they are closely related to anharmonic lattice vibration. Meanwhile, the relaxation behavior of defect dipoles may operate within the microwave frequency range and therefore deserves careful consideration in the development of microwave dielectric ceramics.

2.2.4 Influence mechanism of τ_f value

The τ_f value is a critical parameter for evaluating the thermal stability of microwave dielectric materials, which is defined as:

$$\tau_f = \frac{1}{f_0} \cdot \frac{\Delta f}{\Delta T} \tag{48}$$

Here, f_0 denotes the initial resonant frequency, Δf is the change in resonant frequency, and ΔT is the temperature change. For a dielectric resonator, τ_f is expressed as [147]:

$$\tau_f = -\left(\frac{\tau_\varepsilon}{2} + \alpha_{\mathrm{L}} \right) \tag{49}$$

Here, α_{L} is the linear thermal expansion coefficient and τ_ε is the temperature coefficient of dielectric constant. While α_{L} is typically around 10 ppm/°C and often considered secondary, it can be significant in materials like $LnNbO_4$-based ceramics (α_{L} > 15 ppm/°C) or negative in zirconium tungstates [148-150]. Therefore, its contribution cannot be ignored. τ_ε, which reflects the temperature dependence of permittivity, is derived from the Clausius–Mossotti equation as [151]:

$$\tau_{\varepsilon} = \frac{1}{\varepsilon_{\mathrm{r}}}\left(\frac{\partial \varepsilon_{\mathrm{r}}}{\partial T}\right)_{P} = \frac{(\varepsilon_{\mathrm{r}}-1)(\varepsilon_{\mathrm{r}}+2)}{\varepsilon_{\mathrm{r}}}(A+B+C) \tag{50}$$

$$A = \frac{1}{\alpha_{\mathrm{m}}}\left(\frac{\partial \alpha_{\mathrm{m}}}{\partial T}\right)_{V};\ B = \frac{1}{3\alpha_{\mathrm{m}}}\left(\frac{\partial \alpha_{\mathrm{m}}}{\partial V}\right)_{T}\left(\frac{\partial V}{\partial T}\right)_{P};\ C = -\frac{1}{3V}\left(\frac{\partial V}{\partial T}\right)_{P} \tag{51}$$

Here, term A reflects the effect of temperature on polarizability at constant volume, which is usually negative. Term B is the effect of thermal expansion on polarizability, which is positive, and term C represents the effect of volume change on dipole concentration, which is negative. Bosman concluded that the sign and magnitude of τ_{ε} are primarily governed by term A.

Harrop proposed that if terms A and B cancel ($\tau_{\alpha m} = 0$), τ_f should be proportional to ε_r ($\tau_f \sim \alpha_L\varepsilon_r/2$) [152, 153]. This mechanism suggests that reduced ionic polarizability lowers ε_r and τ_f value, explaining why most high-ε_r (≥ 20) materials exhibit positive τ_f. While observed in some K_2NiF_4-type systems (e.g., $SrLaAl_{1-x}(Zn_{0.5}Ti_{0.5})_xO_4$), this mechanism fails to explain negative τ_f value or the sign change from negative to positive, indicating its limited applicability [154-156].

To address negative τ_f value, Colla and Reaney identified octahedral tilting and structural phase transitions as key factors in complex perovskites [157, 158]. They linked τ_f to the tolerance factor (t). Subsequent work showed that adjusting ferroelastic-paraelastic phase transition temperatures via ion substitution can tune τ_f from negative to positive (e.g., in $BiVO_4$ and $LnNbO_4$ systems) [90, 159-162]. However, conventional phase transition theory cannot explain all anomalies: some room-temperature ferroelastic phases show unexpectedly positive τ_f, while paraelastic phases show negative τ_f [148-150, 163]. Furthermore, anomalous τ_f behavior in systems without phase transitions (e.g., vanadate) suggests other unidentified factors [164, 165].

Lee proposed that increased unit-cell volume alters lattice potential energy, increasing τ_{ε} and thus reducing τ_f, which explained negative τ_f in ANb_2O_6 ceramics [166]. However, contradictory trends exist. In scheelite-type $Ca_{1-x}(Li_{0.5}Nd_{0.5})_xWO_4$, τ_f increases with volume expansion [167].

Similarly, opposite τ_f trends with volume change in Ba- and Sr-based complex perovskites indicate this mechanism is not universally applicable [166].

The relationship between octahedral/tetrahedral distortion and τ_f is inconsistent. Some studies (e.g., on $BiNbO_4$, $MgTiO_3$, $LiBO_2$) report that greater distortion lowers τ_f [168-171]. Conversely, other work on $(Al_{1/2}Ta_{1/2})O_2$–TiO_2 or $AZrNb_2O_8$ shows that increasing distortion can raise τ_f or shows no direct correlation [172-174]. These conflicting results highlight the complexity of this factor.

Li Lingxia's group used complex chemical bond theory to show that τ_f decreases with increasing ionicity of Nb/Ta–O bonds [175]. Studies on silicates and molybdates suggest higher bond energy leads to a lower α_L, which increases τ_ε and drives τ_f toward zero [176, 177]. In $RETiTaO_6$ ceramics, the ionic/covalent character of RE–O bonds significantly influences both ε_r and τ_f.

Bond valence theory is widely applied, with the general assumption that higher bond valence strengthens interionic bonding, counteracts thermal restoring forces, increases τ_ε, and thus lowers τ_f. While some studies (e.g., on Pb-based and Ca-based perovskites, $A_6B_5O_{18}$ compounds) support a correlation between increased B-site bond valence and reduced τ_f, significant issues remain, including inaccurate structural data leads to erroneous bond valence calculations, the assumption that higher bond valence always drives τ_f toward zero is flawed, as τ_f is not bounded by zero, and using average bond valences for mixed-site occupancies obscures the individual contributions of specific cations [178].

In 2020, Fang Liang's group fabricated dense $A_3Y_2Ge_3O_{12}$ (A = Ca, Mg) microwave dielectric ceramics with cubic garnet structures [179]. $Ca_3Y_2Ge_3O_{12}$ adopts a normal garnet structure, where Ca^{2+} occpuies the dodecahedral A-site, Y^{3+} is on the octahedral B-site, and Ge^{4+} is on the tetrahedral C-site, exhibiting ε_r = 10.8, $Q \times f$ = 97,126 GHz, and τ_f = -40.6 ppm/°C. In contrast, $Mg_3Y_2Ge_3O_{12}$ crystallizes in an inverse garnet structure, where A-site is co-occupied by Mg^{2+} and Y^{3+}, and B-site is occupied by Mg^{2+}, showing a higher ε_r of 14.1, a lower

$Q \times f$ value of 12,600 GHz, and anomalously positive τ_f value of 120.5 ppm/°C. Bond-valence analysis reveals that Mg^{2+} in $Mg_3Y_2Ge_3O_{12}$ has a bond valence of only 1.25, significantly below its theoretical value of 2, indicating a pronounced "rattling" effect within the eight-coordinated dodecahedral sites. The concept of rattling cations, originally introduced by Dunitz and Orgel, describes cations too small for their coordination cavity, leading to loose bonding and off-center displacements, as illustrated in **Fig. 12** [180]. When constrained by crystal symmetry, such displacements increase bond lengths and thermal vibrations, generating anomalously high polarizability. These rattling or compressed states can be quantitatively characterized by bond valence: values above theoretical indicate compression; below indicate rattling.

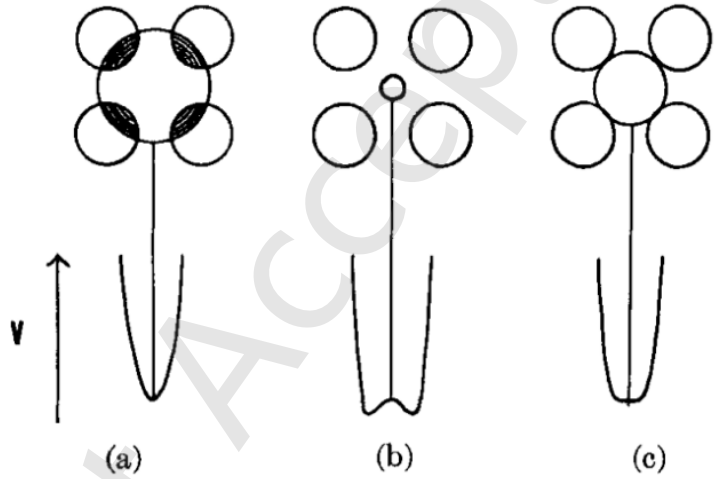

Figure 12. Variation of potential energy with displacement of a metal ion from the center of a fixed oxide octahedron (for clarity shown in two dimensions): (a) large ion, (b) small ion, (c) ion of intermediate size [151]. Reproduced with permission from Ref. [151], © American Physical Society 1963.

Shannon demonstrated that rattling effects lead to underestimation of ionic polarizability and dielectric constant, while compressed effects cause overestimation [31]. Although rattling effects have been reported in various microwave dielectric systems, their explicit link to τ_f remained unexplored. In our garnet systems, opposite trends between theoretical and measured ε_r, along with anomalous τ_f behavior, led us to hypothesize that rattling influences the temperature coefficient of ionic polarizability ($\tau_{\alpha m}$), consequently affecting τ_ε and τ_f [155, 181]. Due to the pronounced rattling of Mg^{2+} in $Mg_3Y_2Ge_3O_{12}$, ionic polarizability is significantly

enhanced, yielding measured ε_r approximately 30% higher than theoretical estimates. To quantify how rattling affects τ_ε and τ_f, we combined terms A and B from the Clausius-Mossotti derivation and introduced $\tau_{\alpha m}$, as follows [182, 183]:

$$\tau_\varepsilon = \frac{1}{\varepsilon_r}\left(\frac{\partial \varepsilon_r}{\partial T}\right) = \frac{(\varepsilon_r - 1)(\varepsilon_r + 2)}{3\varepsilon_r}\left(\frac{1}{\alpha_m}\frac{d\alpha_m[T,V(T)]}{dT} - \frac{1}{V}\frac{dV}{dT}\right) \quad (52)$$

$$\tau_{\alpha m} = \frac{1}{\alpha_m}\frac{d\alpha_m[T,V(T)]}{dT} \quad (53)$$

The relationship simplifies to τ_ε depending on ε_r, $\tau_{\alpha m}$, and the linear thermal expansion coefficient α_L. The sign of τ_ε and thus τ_f is determined by the difference between $\tau_{\alpha m}$ and the volumetric expansion coefficient ($3\alpha_L$ for cubic systems) [184]. From experimental τ_f and α_L values, we calculated $\tau_{\alpha m}$ values ranging from 37.33 ppm/°C to 14.36 ppm/°C, revising earlier estimates. For $Ca_3Y_2Ge_3O_{12}$, $\tau_{\alpha m}$ is a large positive value exceeding $3\alpha_L$, resulting in strongly negative τ_f. In $Mg_3Y_2Ge_3O_{12}$, $\tau_{\alpha m}$ is significantly reduced, yielding anomalously positive τ_f. Raman spectroscopy reveals that A-site occupation by Mg^{2+} and Y^{3+}, ions with markedly different radii and polarizabilities, induces local distortion and enhances anharmonic vibrations, increasing dielectric loss and reducing $Q \times f$. Low-frequency infrared modes (67.8 and 122.6 cm^{-1}), attributed to translational vibrations of A-site cations, dominate dielectric polarization in $Mg_3Y_2Ge_3O_{12}$. To further verify the rattling effect's influence, we investigated $Ca_{3-x}Mg_xYb_2Ge_3O_{12}$ ($0 \le x \le 3$) solid solutions [183]. The ionic-radius difference at the A-site ($\Delta r_A = r_{Yb} - r_{Mg} = 0.095$ Å) is smaller than in the Y-analog (0.125 Å), predicting weaker rattling. For $0 \le x \le 2$ (normal garnet), ε_r increases gradually from 10.3 to 11.8, $Q \times f$ decreases from 98,000 GHz to 78,000 GHz, and τ_f fluctuates between -40 ppm/°C and -56 ppm/°C. At $x > 2$ (inverse garnet), ε_r jumps to ~13.5, $Q \times f$ drops sharply to ~19,800 GHz, and τ_f shifts from negative to positive (70.5 ppm/°C), with near-zero τ_f achieved at $x = 2.5$.

Calculated results show that rattling can be modulated by A-site cation selection, altering $\tau_{\alpha m}$ and enabling τ_f tuning. For normal garnet compositions ($x \le 2$), $\tau_{\alpha m}$ is positive, reaching

16.88×10^{-6}/°C, exceeding α_L. At $x > 2$, introduction of smaller Mg^{2+} into relatively large A-sites elongates Mg–O bonds, inducing rattling that enhances dielectric polarization and ε_r. With increasing temperature, rattling diminishes, dielectric polarization weakens, and $\tau_{\alpha m}$ decreases sharply to -1.22 ppm/°C in $Mg_3Yb_2Ge_3O_{12}$, where $\tau_{\alpha m} < 3\alpha_L$ causes ε_r to decrease, τ_ε to become negative, and τ_f to become positive.

In other garnet systems, stronger rattling effects drive τ_f toward highly positive values. In $Ca_{3-x}Mg_{1+x}LiV_3O_{12}$, larger A-site ionic-radius difference induces stronger rattling, shifting τ_f from -64.1 ppm/°C to 267.2 ppm/°C. In $Y_{3-x}Ca_xGa_{5-x}Ti_xO_{12}$, substituting smaller Y^{3+} with Ca^{2+} elongates Y–O bonds, enhancing rattling of Y^{3+}, increasing ε_r from 10.4 to 15.9, and shifting τ_f from -54.7 ppm/°C to -8.3 ppm/°C [185]. On the contrary, in garnets where rattling is suppressed by stronger chemical bonding in low-coordination environments (B-site, C-site), τ_f remains strongly negative despite slightly elevated ε_r [186, 187].

Under microwave frequencies, polarization is primarily ionic displacement polarization. Using a harmonic oscillator model, as shown in **Fig. 13**, in the rattling state (bond elongation), the restoring force points opposite to displacement, increasing ionic polarizability (α_m) and ε_r. As temperature increases, enhanced restoring force rapidly reduces ionic polarizability, causing $\tau_{\alpha m}$ and τ_ε to decrease, which increases τ_f.

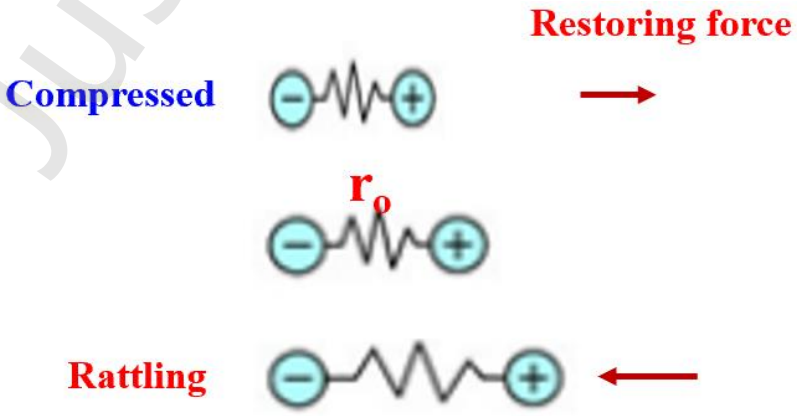

Figure 13. The restoring force of the simple harmonic oscillator model in compressed, equilibrium position and rattling state, respectively.

The rattling effects have been verified in other systems. For instance, in tetragonal scheelite $Ca_{1-x}(Li_{0.5}Eu_{0.5})_xMoO_4$ and $Ca_{1-x}(Li_{0.5}Eu_{0.5})_xWO_4$ solid solutions, A-site substitution with smaller $(Li_{0.5}Eu_{0.5})^{2+}$ induces strong rattling of Li^+ (bond valence 0.524~0.540, below theoretical) [188]. This causes measured ε_r to exceed Clausius-Mossotti predictions by 4.6% up to 41.2%, while τ_f shifts dramatically from negative to highly positive values (-14.4 ppm/°C to 128.42 ppm/°C) in $Ca_{1-x}(Li_{0.5}Eu_{0.5})_xMoO_4$ ($0.1 \le x \le 0.5$) ceramics, as shown in **Fig. 14.** Near-zero τ_f is achieved at specific compositions. The anomalous decrease in $\tau_{\alpha m}$ from positive to strongly negative drives this τ_f shift, contradicting classical expectations that anharmonic bond softening necessarily enhances polarization.

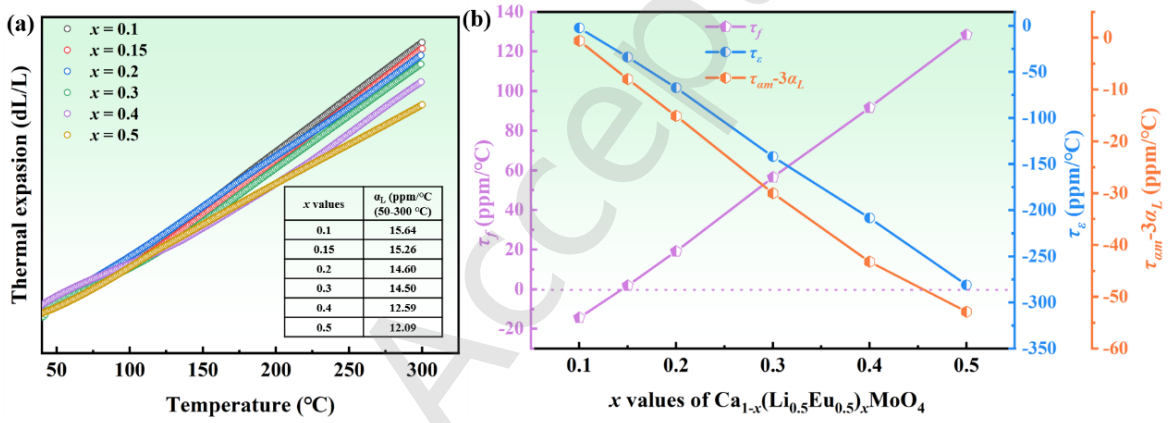

Figure 14. (a) Thermal expansion data; (b) The relationship between the values of τ_ε, τ_f and $\tau_{\alpha m}$-$3\alpha_L$ for $Ca_{1-x}(Li_{0.5}Eu_{0.5})_xMoO_4$ ceramics. Reproduced with permission from Ref. [188], © Elsevier Ltd. 2024.

Also, in monoclinic fergusonite $(Ce_{1-x}Ca_x)(Nb_{1-x}W_x)O_4$, substitution induces a structure transition from monoclinic fergusonite to tetragonal scheelite [189]. Measured ε_r values are lower than Clausius-Mossotti predictions due to A-site compressed effects (Ca^{2+}, Ce^{3+}). As x increases, elongation of [Nb/WO_6] octahedra enhances B-site rattling, while A-site compression weakens. Consequently, τ_f increases from -11 ppm/°C to 87.8 ppm/°C. Furthermore, as shown in **Fig. 15** [190], in tetragonal K_2NiF_4-type systems, the $SrEuAlO_4$ and $SrGdAlO_4$ exhibit near-zero τ_f (1.7 ppm/°C and 4.3 ppm/°C) with ε_r of 19.2. Strong rattling of Eu^{3+} and Gd^{3+} shifts τ_f closer to zero compared with other $SrLnAlO_4$ compositions. The significantly lower $Q \times f$ of $SrGdAlO_4$ is attributed to the high magnetic moment of Gd^{3+}. In

$CaREAlO_4$ (RE = Eu, Ho, Er, Yb) ceramics, τ_f variations are governed by competing rattling of RE^{3+} and compressed effects of Ca^{2+}.

The rattling effect's influence on τ_f has been also verified across diverse crystal systems: hexagonal $SrGe_4O_9$ ($\Delta\varepsilon_r$ = 37.3%, τ_f = -11.7 ppm/°C), tetragonal $LiInO_2$ ($\Delta\varepsilon_r$ = 14.7%, τ_f = 9.8 ppm/°C), $LiYbO_2$ ($\Delta\varepsilon_r$ = 45.1%, τ_f = 56.5 ppm/°C), and rare-earth oxide solid solutions $Nd_{2-x}Sm_xO_3$ ($\Delta\varepsilon_r$ = 0~13.1%, τ_f = -43 to 34.1 ppm/°C) [170, 171, 184, 191]. Notably, $SrGe_4O_9$ maintains high $Q\times f$ (52,500 GHz) despite strong Sr^{2+} rattling, owing to single A-site cation species avoiding mixed-cation anharmonic vibrations. In AB_2O_4-type systems ($SrYb_2O_4$, ASc_2O_4), weakened rattling from larger Sr^{2+} simultaneously improves τ_f while preserving ultra-high $Q\times f$ (≥107,000 GHz) [192].

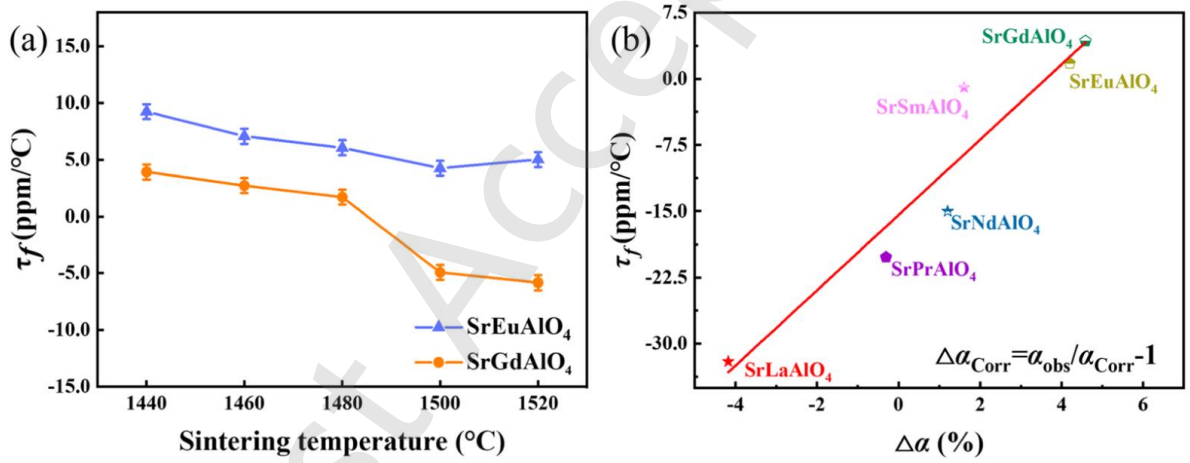

Figure 15. (a) τ_f values of $SrEuAlO_4$ and $SrGdAlO_4$ ceramics as a function of sintering temperature. (b) the relationship of τ_f and $\Delta\alpha$ in $SrLnAlO_4$ (Ln = La, Pr, Nd, Sm, Eu, and Gd) ceramics[190]. Reproduced with permission from Ref. [190], © Elsevier Ltd. 2024.

In cubic fluorite $Ce_{1-x}Ca_xO_{2-x}$ ceramics, measured ε_r decreases with Ca content, but much more slowly than Clausius-Mossotti predictions, yielding increasing deviations ($\Delta\varepsilon_r$ up to 84%) [193]. Bond-valence analysis reveals Ce^{4+} as rattling cations and Ca^{2+} as compressed cations. A weighted parameter $\Delta\alpha_m$, reflecting combined rattling and compressed effects on ionic polarizability, was introduced. $\Delta\alpha_m$ is defined as follows:

$$\Delta\alpha_{\mathrm{m}} = (1-x)\frac{d_i(\mathrm{Ce}^{4+})\alpha(\mathrm{Ce}^{4+})}{V_{\mathrm{Ce(ideal)}}} - x\frac{d_i(\mathrm{Ca}^{2+})\alpha(\mathrm{Ca}^{2+})}{V_{\mathrm{Ca(ideal)}}} + (2-x)\frac{d_i(\mathrm{O}^{2-})\alpha(\mathrm{O}^{2-})}{V_{\mathrm{O(ideal)}}} \quad (54)$$

As x increases, $\Delta\alpha_{\mathrm{m}}$ decreases, indicating progressively weaker Ce^{4+} rattling, explaining the growing deviation between measured and theoretical ε_{r}. Since 2023, multiple research groups have reported rattling effects on τ_f. In MSO_4 (M = Ca, Sr, Ba) systems, enhanced M^{2+} rattling increases ε_{r} and τ_f while decreasing $Q\times f$ [194]. In perovskite $Ba_{1-x}Sr_xHfO_3$ and $Sr_{1-y}Ca_yHfO_3$ systems, as tolerance factor decreases, the dominant τ_f tuning mechanism shifts from phase transition and ionic-polarizability dilution to rattling [195]. The rattling effect has also been validated in Si-substituted garnet $Y_{3-x}Mg_xAl_{5-x}Si_xO_{12}$ systems [196].

This summary systematically reviews the established structural factors influencing τ_f, including the ionic polarizability dilution mechanism, phase transition mechanism, unit cell volume effects, oxygen polyhedral distortion, bond energy/ionicity, and bond valence. Based on recent observations in normal and inverse garnet systems without phase transformations, where the measured dielectric constant trends opposite to theoretical estimates and τ_f anomalously shifts from negative to positive, a new mechanism affecting τ_f is proposed: the cation rattling effect. This effect not only enhances polarization and increases ε_{r} but also shifts τ_f positively and reduces the $Q\times f$ value, and has been validated across various material systems. The concept of the temperature coefficient of ionic polarizability ($\tau_{\alpha\mathrm{m}}$) is introduced, simplifying the relationship between the temperature coefficient of permittivity (τ_ε) and crystal structure into its dependence on ε_{r}, $\tau_{\alpha\mathrm{m}}$, and α_{L}. Additionally, a weighting function for total ionic polarizability deviation is proposed to evaluate the combined rattling and compressed effects of the entire molecule on ε_{r}. It is concluded that rattling cations located in high-coordination sites with weak chemical bonding are the primary factors governing the overall microwave dielectric polarization and loss of materials.

2.3 Innovative Technology for Energy Efficient Fabrication: Cold Sintering Process

Generally, the sintering of ceramics requires high temperatures (typically >1000 °C), which pose various challenges, such as material loss of volatile elements and excessive consumption of energy, contradicting the objectives of eco-friendly manufacturing [197]. Subsequently, there is a strong need to develop low temperature sintering technologies to density ceramics without harming the climate [198]. Consistent efforts resulted in the invention of a cutting-edge sintering technique by Randall's team at Pennsylvania State University, known as cold sintering process (CSP), in 2016 [199]. CSP not only enables the densification of ceramics at ultra-low temperatures but also manipulate their performances [200-202]. Compared to traditional sintering, where densification is predominantly influenced by the diffusion process, CSP is based on a dissolution-precipitation mechanism. With an aqueous environment under mild pressures, particles undergo localized dissolution, followed by bonding and precipitation with the assist of transient liquid [203, 204]. CSP has become the research focus as an energy-saving and versatile sintering technology befitting for ceramics and ceramic based composites [205]. CSP has recently gained enormous attention due to its potential to co-sinter microwave dielectric ceramics with polymers, glasses, and metal electrodes, which have low melting points [206]. Co-firing ceramics with low-melting-point electrodes is an indispensable requirement for the passive devices and packaging of active components [207, 208]. A large number of material systems have been efficiently densified by CSP, achieving relative densities (> 90%) at ultra-low temperatures while sustaining superior dielectric properties [209-212]. These outcomes indicate that CSP facilitates densification of MWDCs and prevents the decomposition and volatilization of the phase associated with conventional sintering at high temperatures.

CSP is commonly referred to as a nature-inspired process due to its aqueous conditions with mild temperatures and pressures, which appears like a process of rock formation primarily driven by viscous flow, plastic deformation, and pressure-solution creep [213]. However, the rock formation under natural conditions requires centuries, whereas CSP densifies a diverse range of materials in a few hours or even minutes. CSP promotes the compaction of ceramics

and their composites at extremely low sintering temperatures using an aqueous medium [214]. Randall and his team proposed the concept of dissolution-precipitation for cold sintering mechanism [200]. In general, prospective CSP involves two types of phases, including pristine powder phase to develop a ceramic body, and a liquid phase which serves as a mobility channel for particles [206]. Contributing factors during CSP are primarily temperature, pressure, and transient liquid, which can vary depending on the material [215, 216]. When a suitable temperature is provided under a uniaxial pressure, a capillary force provided by a transient liquid alters the distribution of particles and fills the interfacial spaces between particles [217].

Generally, the following steps are involved in CSP, as shown in **Fig. 16** [215] [218, 219]. Initially, a transient liquid (typically < 30 vol.%) is introduced into ceramic powder to moisten the powder. Depending on the materials, homogeneity can sometimes be achieved by adding a transient liquid using a vapor transport method [220]. Afterwards suitable temperature is provided, and uniaxial pressure is simultaneously applied and sustained for a specific time. In 2nd step, compaction is facilitated through mass transportation in the liquid with dissolution precipitation process, where the particles move from the regime with high chemical potential to the regime with low chemical potential [214, 221]. Consequently, other phenomena may also occur, such as viscous flow, grain growth, lattice diffusion, and plastic deformation, under the continuous supply of heat and pressure [222]. In some scenarios, unusual grain growth can be observed during the volatilization of the transient liquid, even at low temperatures. Such anomalous grain growth can be attributed to mass transfer in the presence of a transient liquid [223].

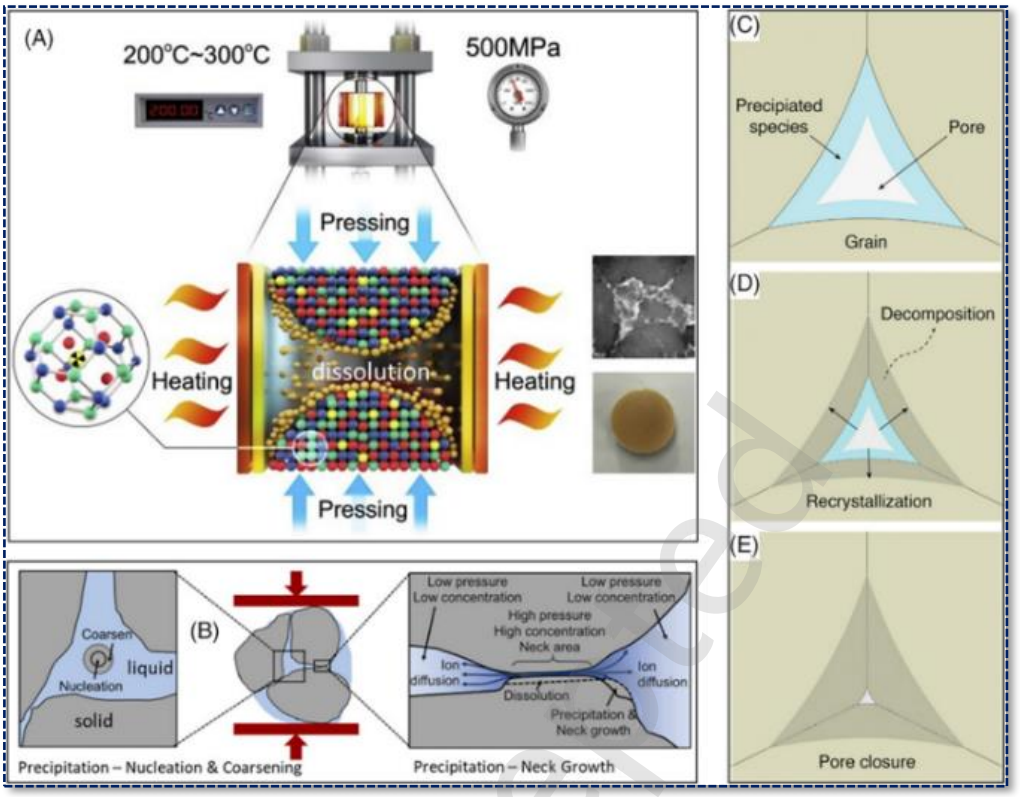

Figure 16. Schematic illustration of major events of the cold-sintering process: (A) dissolution[218] Reproduced with permission from Ref. [218], © Elsevier B.V. 2019., (B) precipitation[207], (C) precipitation occurs at the pore, (D) recrystallization of precipitated species and decomposition of organic species, and (E) pore closure[219]. Reproduced with permission from Ref. [219], © Elsevier Ltd. 2022.

The parameters that affect CSP and reaction pathways for densification of materials include the following aspects: First, the physicochemical properties of the starting materials, such as particle size, surface chemistry, and agglomeration, have a significant impact on the sintering behaviors of microwave dielectric ceramics [224]. Additionally, transient solvents have both physical and chemical effects, contributing to densification [225]. Furthermore, temperature has a pivotal role in compaction, grain growth, mass transport, and solvent evaporation. Depending on the material systems, the temperature generally varies from room temperature to 300°C [204]. Another fundamental factor for densification using CSP is the optimal pressure, typically a few hundred MPa. The pressure offers a greater driving force that facilitates dissolution, precipitation, and mass mobility, consequently increasing grain growth and densification [202]. Optimal pressure boosts the chemical potential difference, particularly at

particle contact sites, thereby increasing the solubility of particles. When a low pressure is applied, particles merge gradually with limited contact points; In contrast, high pressure results in Ostwald ripening and dissolution-precipitation [220]. Dwell time for CSP is typically less than that for conventional sintering, depending on solubility and volatilization during the CSP. Typically, materials with a high solubility require a short time for CSP [226].

In wireless communication systems, suitable dielectric, mechanical and thermal properties together with low sintering temperatures are required for microwave dielectric ceramics [4]. Kähäri et al densified Li_2MoO_4 microwave dielectric ceramics at room temperature under a uniaxial pressure of 130 MPa [227]. Relative densities of 87~93% were obtained with good microwave dielectric properties after post annealing (ε_r = 4.6~5.2 and $Q\times f$ =10,200~18,500 GHz). Guo et al. proposed cold sintering process and densified a wide variety of microwave dielectric ceramics with CSP at 120~300 ℃, such as Li_2MoO_4, $Na_2Mo_2O_7$, $K_2Mo_2O_7$, and $K_2Mo_2O_7$ [199]. Later on, the cold sintering process of a vast number of microwave dielectric ceramics were investigated, such as oxides, molybdates, tungstates, chlorides and borates, as listed in **Table 3** [209, 211, 222, 228-250]. Compared with conventional high temperature sintering, cold sintered ceramics show comparable or even better microwave dielectric properties. The low sintering temperature of CSP make it feasible to co-fire high-performance ceramics with low-melting metal electrodes, which are promising for wireless communication applications.

Table 3. CSP parameters and microwave dielectric properties of cold-sintered MWDCs

Material	ST (°C)	Pressure (MPa)	Liquid (%)	Time (h)	Post annealing (°C)	Densification (%)	ε_r	$Q\times f$ (GHz)	τ_f (ppm /°C)	Ref.
Na_2WO_4	120	120	0.3-10	1	300	>96	5.7	70,000	−70	[228]
Na_2WO_4	240	400	2	1	200	92	5.8	22,000	−70	[229]

(1-*x*)$MgTiO_3$–*x*Bi_2O_3	200	250	0.6	1	1100	96	14.5	39,000	-54	[230]
$Li_2Mg_3TiO_6$	180	300	20	1	950	96	15.5	47,960	–26	[231]
x$MgTiO_3$–(1-*x*)NaCl	235	450	3	0.5	120	90	7.2	29,500	-136	[232]
LiF–$CaTiO_3$	150	350	10	1	800	96	10.9	26,580	3	[233]
Al_2O_3	150	375	10	1	1575	94	9.7	100,220	− 55	[234]
TiO_2	300	350	16.7	4	1000	98	98.4	31,900	431	[211]
HBO_2	180	25	------	2	------	>80	2.1	32,700	−43	[235]
H_3BO_3	25	100	10	0.16	------	98	2.8	146,000	−242	[236]
Al_2O_3–H_3BO_3	25	400	10	0.16	------	96	5.4	12,924	-73	[237]
HBO_2–II	120	500	10	0.16	------	94.7	4.2	47,500	−70	[238]
$Zn_3B_2O_6$	200	300	20	1	550	95	5.95	20,620	-67	[239]
$(Mg_{1-x}Ni_x)_3B_2O_6$	150	800	15	1.5	1100	92	6.9	24,336	−53	[240]
NaCl	25	300	4	0.17	-----	94	5.6	49,600	−173	[222]
LiF	150	250	10	1	800	92	8.2	110,800	−135	[209]
LiF	25	900	10	0.5	825	95.4	8.5	118,400	−154	[241]
ScF_3	150	400	10	0.5	-----	93.2	5.3	14,700	−58	[242]
$Na_2Mo_2O_7$–hBN	180	250	25	2	200	96	7.3	16,000	−13	[243]
$LiWVO_6$–K_2MoO_4	160	300	10	1	700	98	6.8	7180	−49	[244]
$(Ca_{0.65}Bi_{0.35})(Mo_{0.65}V_{0.35})O_4$	150	300	4-9	1	120	92	11.4	7070	−7	[245]

$Na_{0.5}Bi_{0.5}MoO_4$ –Li_2MoO_4	150	200	5-10	0.5	120	96	17.4	7470	–5	[246]
$CaSnSiO_5$–K_2MoO_4	180	400	15	1	120	99	9.2	6240	−1	[247]
$NaCa_2Mg_2V_3O_{12}$–Li_2MoO_4	200	450	10-15	0.83	120	94	7.0	13,400	–118	[248]
Li_2MoO_4–20 vol%TiO_2	25	150	-----	-----	120	88	8.7	4000	20	[249]
Li_2MoO_4–50 wt% Garnet	250	450	15	0.83	120	95	7.6	2300	−124	[250]

Based on cold sintering process, several hybrid sintering processes have been proposed, such as microwave cold sintering (MW-CSP) and cold sintering assisted spark plasma sintering (SPS-CSP). Cold sintering assisted hybrid sintering process is a multistep densification process, which involves the coupling of chemical potential and multi-physical fields, as shown in **Fig. 17** [251]. Since the concept of cold sintering assisted hybrid sintering process was proposed very recently, the research of sintering mechanism is still in the initial stage. The major mechanism may include dissolution-precipitation, microwave resonance heating or heating from the pulse/DC current.

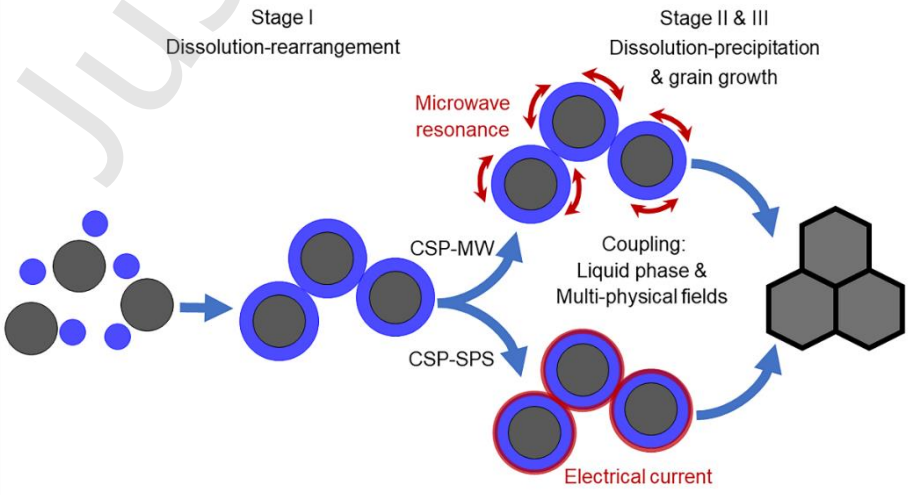

Figure 17. Schematic diagram of microwave cold sintering and cold sintering assisted spark plasma sintering[251]. Reproduced with permission from Ref. [251], © The American Ceramic Society 2023.

Recently, microwave cold sintering process, has successfully achieved efficient densification of high-performance ceramics under mild conditions. This process combines a transient liquid-phase-assisted dissolution-precipitation mechanism with the microwave resonance effect to achieve rapid, low-temperature, pressureless sintering of a variety of ceramics, including chlorides, oxides, phosphates, and molybdates. TEM and phase-field simulation results demonstrate that the combination of transient liquid phase and microwave resonance improves the driving force of sintering. The transient liquid phase not only promotes particle rearrangement and dissolution-precipitation processes, but its resonant behavior in high-frequencies also significantly improves the overall heating efficiency and atomic migration rate, synergistically accelerating the densification of ceramics.

In terms of performances, ceramics prepared via MW-CSP exhibit significant advantages, as shown in **Fig. 18** [252]. The Vickers hardness of the MW-CSP NaCl ceramic is 95.2% higher than that of conventionally sintered samples. Compared with other sintering technologies, the microwave dielectric properties of TiO_2, Li_2MoO_4, and $MgMoO_4$ ceramics prepared by microwave cold sintering process are similar or even better. The MW-CSP KDP ceramic exhibits ferroelectric phase transition behavior comparable to that of previous works using traditional fabrication methods. Notably, compared with other pressureless sintering techniques, MW-CSP reduces energy consumption by more than 97%, lowers sintering temperatures by 225~500 °C, and shortens sintering time by 12.8~21.5 hours. It is demonstrated that MW-CSP opens a new path for preparing low-carbon, energy-efficient, and high-performance ceramics with broad application prospects. It is anticipated that more research groups worldwide will expand the range of applicable material systems with energy-efficient sintering.

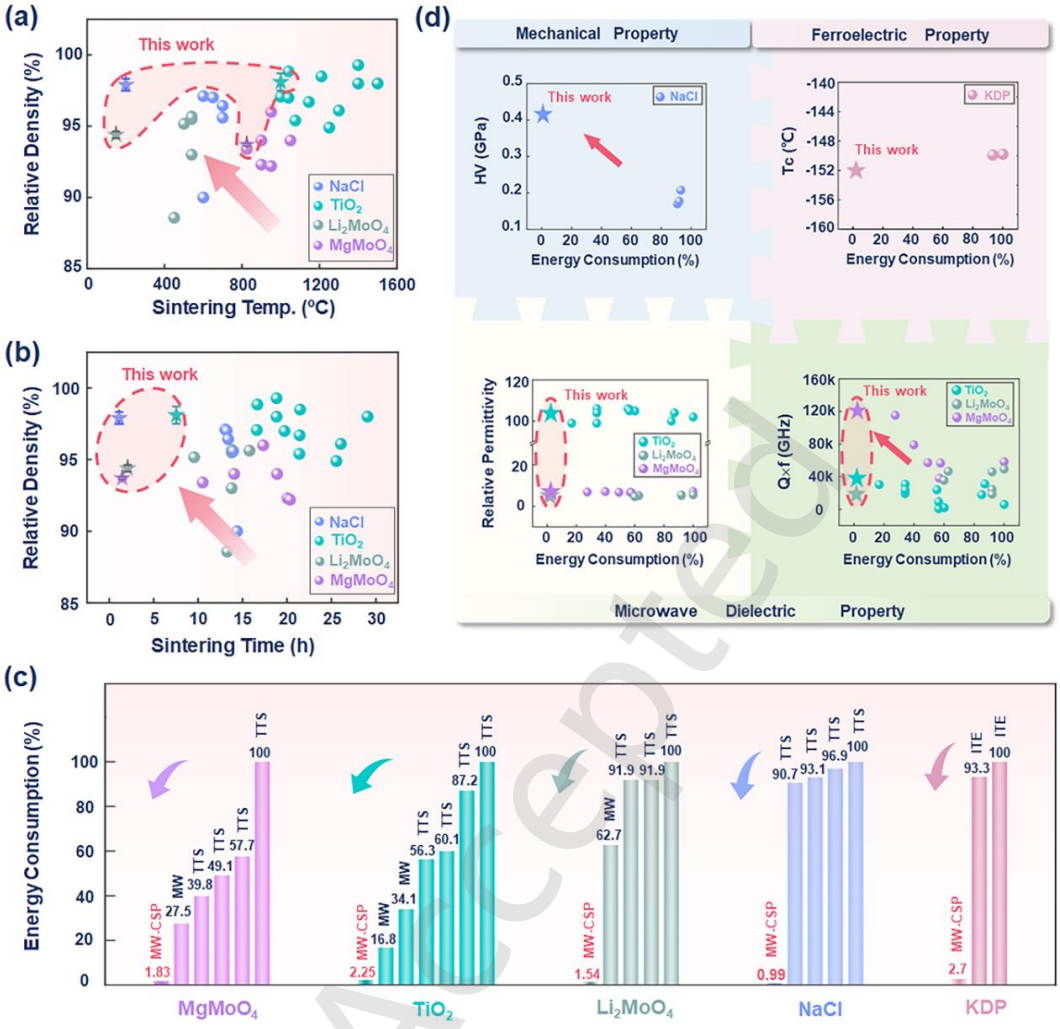

Figure 18. Energy efficiency comparisons. Summary of relative density vs (a) sintering temperature and (b) sintering time for NaCl, $MgMoO_4$, TiO_2 and Li_2MoO_4 ceramics regarding to various pressureless sintering techniques. Comparisons of (c) energy consumptions after normalization and (d) performances of densified ceramics using various pressureless sintering techniques. MW-CSP, TTS, MW, and ITE represent microwave cold sintering, traditional thermal sintering, microwave sintering, and isothermal evaporation method, respectively[252].

A number of groups have developed high-performance ceramics using cold sintering assisted spark plasma sintering. However, there no few works about microwave dielectric ceramics prepared via SPS-CSP, and thus, ZnO semiconducting ceramic is selected as a typical example to demonstrate the features of SPS-CSP, as shown in **Fig. 19** [253]. SPS yields ceramics with short times and low pressures, however, the sintering temperatures are usually high. CSP could densify ceramics at low temperatures, however, mild or high pressures may be utilized during

CSP. SPS-CSP combines the advantages of both SPS and CSP, which could densify ceramics with low sintering temperatures, short times, and low pressures. It is anticipated that in the future there will be microwave dielectric ceramics fabricated via SPS-CSP.

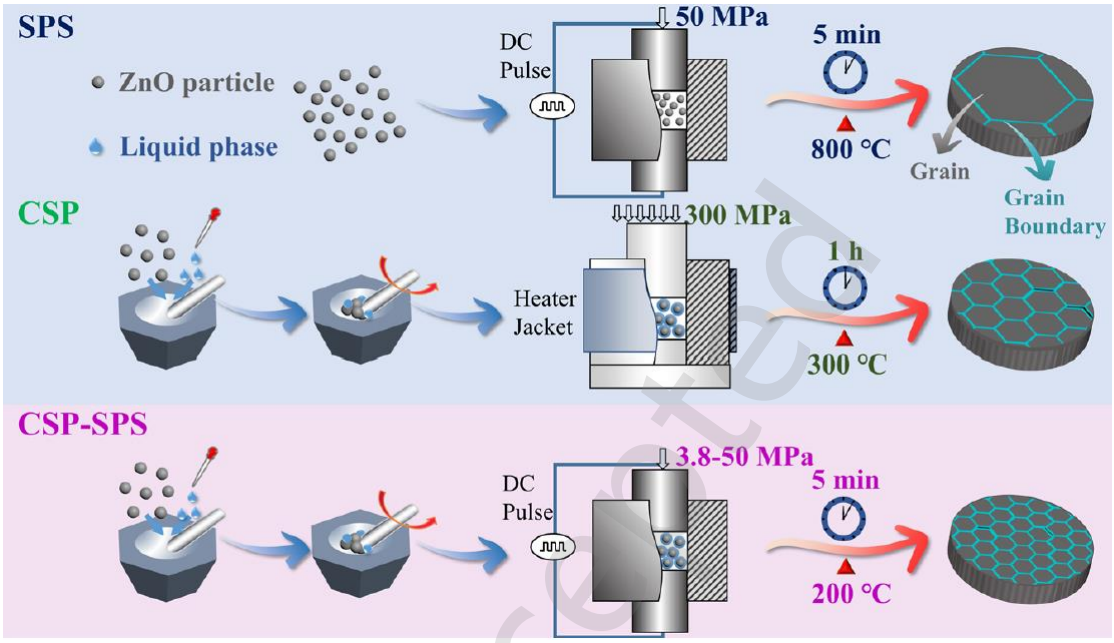

Figure 19. Schematic sintering process for SPS, CSP and SPS-CSP (or CSP-SPS)[253]. Reproduced with permission from Ref. [253], © Elsevier Ltd. 2022.

In conclusion, cold sintering process is a low temperature sintering technique with the assist of transient liquid phase, and there are a number of cold sintered microwave dielectric ceramics and devices developed so far. The low sintering temperature, high sintering efficiency and low energy consumptions make it promising for LTCC and ULTCC applications. It is feasible to fabricate microwave dielectric materials that are easily to be decomposed or chemically react at high temperatures. Besides, cold sintering process enables multi-material strategy for the integration of ceramics with other materials. However, various problems still need to be resolved for cold sintering process, such as optimization of transient liquid phase, material designs with comprehensive performances, further understanding of sintering mechanism, and large-scale production.

Up to date, a large number of microwave dielectric ceramics have been densified using cold sintering process at lower sintering temperature, shorter time and reduced energy consumption,

as shown in **Fig. 20**. The low sintering temperature makes microwave dielectric ceramics compatible with most of the metal electrodes. Compared with traditional thermal sintering, the cold sintered chloride, fluoride, calcite, borate and Al_2O_3 have better microwave dielectric properties, while molybdate, tungstate, phosphate, vanadate, titanate and TiO_2 prepared via cold sintering process show lower or comparable microwave dielectric properties. It is anticipated that with further understanding of cold sintering process, more and more microwave dielectric ceramics with better performances will be developed in the future.

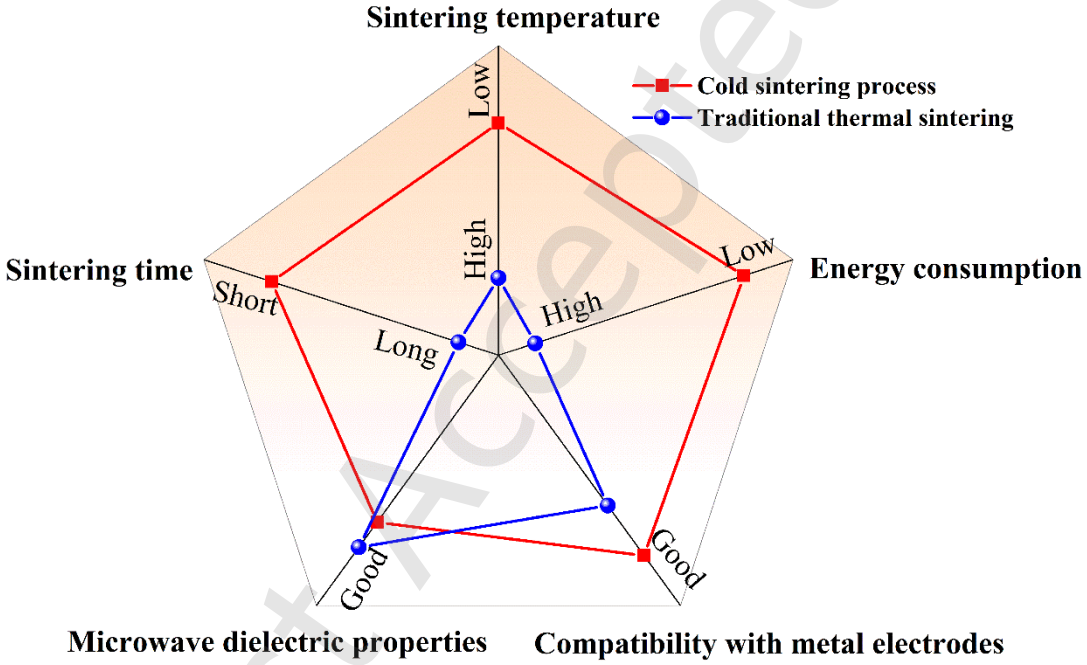

Figure 20. Comparisons of cold sintering process and traditional thermal sintering in the field of microwave dielectric ceramics.

Following perspectives are proposed for future research:

Cold sintered material designs. New material developments need to optimize both cold sintering conditions and material formula, such as combinations of new transient liquid phase and entropy designs. Except microwave dielectric properties, more comprehensive performances such as thermal and mechanical properties are required for future applications. AI may accelerate the screening process of sintering parameters and material compositions.

Mechanism investigation and parameter optimization. Collaborations between computational modeling and experimental science together with in-situ characterizations are essential for detailed sintering mechanism study. Cold sintering assisted hybrid sintering process provides another route for energy efficient fabrications of microwave dielectric materials.

Cold sintered device designs. The rapid developments of wireless communications put forward higher requirement for microwave devices. Systematic investigations into interfacial engineering and structure-process-property relationships under CSP conditions may address the technical barriers of cold sintered devices and packaging.

2.4 Application of Microwave Devices

The dielectric parameters of microwave dielectric ceramics (ε_r, $Q\times f$, τ_f) strongly influence the electromagnetic performance and application scenarios of microwave passive devices. Among these parameters, the relative permittivity ε_r, or the effective permittivity ε_{eff}, determines the propagation velocity and guided wavelength of electromagnetic waves in dielectric media. For quasi-TEM transmission structures such as microstrip lines and dielectric substrates, the phase velocity v_p and guided wavelength λ_g can be expressed as [254]:

$$v_p = \frac{c_0}{\sqrt{\varepsilon_{eff}}} \tag{55}$$

$$\lambda_g = \frac{c_0}{f_0\sqrt{\varepsilon_{eff}}} \tag{56}$$

where c_0 is the speed of light in vacuum, ε_{eff} is the effective permittivity, and f_0 is the operating or resonant frequency. As indicated by Eqs. 55 and 56, a lower permittivity is beneficial for high-speed electromagnetic-wave propagation, whereas a higher permittivity shortens the guided wavelength, thereby facilitating the miniaturization of microwave devices such as antennas, resonators, filters, and duplexers. In addition, the quality factor Q is a key parameter for evaluating the low-loss characteristics of microwave dielectric ceramics. For a resonator,

when external loading effects are neglected, the fractional bandwidth (FBW) is inversely related to the unloaded quality factor Q_0 [254]:

$$\mathrm{FBW} = \frac{1}{Q_0} \tag{57}$$

where Q_0 is closely associated with the dielectric quality factor Q. Although a higher Q value helps reduce dielectric loss and increase the unloaded quality factor Q_0 of the resonator, a higher Q_0 will lead to a narrower FBW when other loss mechanisms and coupling conditions are comparable. Furthermore, according to Eq. 48 in Section 2.2.4 [147], the temperature coefficient of resonant frequency (τ_f) determines the thermal stability of the resonant or center frequency of the device.

Based on the above parameter characteristics, microwave dielectric ceramics with different permittivity ranges are suitable for different types of microwave devices. Low-ε_r microwave dielectric ceramics ($\varepsilon_r \leq 10$) exhibit low signal transmission delay and are therefore suitable as substrate materials for transmission-type and radiation-type passive devices [255]. In addition, low-ε_r ceramics are widely used as dielectric tape layers and packaging substrates in LTCC devices. Through multilayer stacking and three-dimensional interconnection, they enable low-loss interconnects and embedded passive components, thereby further reducing device volume and improving integration density [256]. Medium-ε_r ceramics ($10 < \varepsilon_r < 40$) provide a favorable balance among device miniaturization, low loss, and temperature stability, and are therefore widely used in microwave devices such as dielectric resonators, dielectric resonator antennas, dielectric filters, and duplexers. By simultaneously achieving a high Q value and near-zero τ_f, this class of materials can realize low insertion loss and good frequency–temperature stability [257], making them suitable for high-performance miniaturized devices in communication and radar systems. High-ε_r ceramics ($\varepsilon_r \geq 40$) are mainly used in resonators, filters, and integrated passive devices with more stringent miniaturization requirements [258]. They can significantly shorten the guided wavelength and reduce device dimensions, although optimization of

bandwidth, loss, and processing window is typically required. Moreover, high-permittivity materials can increase capacitance density per unit volume and are therefore widely applied in consumer electronics, automotive electronics, Internet of Things terminals, and other fields where high integration density and miniaturization are strongly demanded.

Ceramic-substrate components typically use ceramics as the supporting and dielectric platforms, where metallized patterns are employed to realize transmission, radiation, or coupling functions. Such components offer advantages including low loss, environmental robustness, and good thermal stability. In terms of component types, ceramic substrates can be used for patch antennas, planar filters, duplexers, couplers, power dividers, combiners, and phase shifters. Among these, ceramic dielectric patch antennas (DPAs) and planar filters are commonly adopted for validating the dielectric performance and application potential of emerging microwave dielectric ceramic materials. In DPAs, the ε_r of the substrate determines the effective electrical size and the resonant dimensions of the antenna, and the initial dimensions of a rectangular patch antenna can be estimated using Eqs. 58-61 [259]:

$$w_p = \frac{c_0}{2f}\sqrt{\frac{2}{\varepsilon_r}} \tag{58}$$

$$l_p = \frac{c_0}{2f\sqrt{\varepsilon_{eff}}} - 2\Delta L \tag{59}$$

$$\varepsilon_{eff} = \frac{\varepsilon_r + 1}{2} + \frac{\varepsilon_r - 1}{2\sqrt{1 + \frac{12h}{w_p}}} \tag{60}$$

$$\Delta L = 0.412h\frac{(\varepsilon_{eff} + 0.3)(\frac{w_p}{h} + 0.264)}{(\varepsilon_{eff} - 0.258)(\frac{w_p}{h} + 0.8)} \tag{61}$$

where f, ε_r, and ε_{eff} denote the resonant frequency, the dielectric constant of the substrate, and the effective dielectric constant, respectively. h, w_p and l_p represent the thickness of the substrate, the width and length of the metal patch, respectively, and ΔL is the correction length. In general,

a dielectric substrate with a higher ε_r can significantly reduce the physical size of a patch antenna; however, this miniaturization is often accompanied by degraded bandwidth, gain, and radiation efficiency due to factors such as stronger field confinement within the dielectric, reduced radiation resistance, and enhanced surface-wave modes.

In addition, a lower tanδ is typically beneficial for suppressing dielectric dissipation loss and improving radiation efficiency and gain. The radiation efficiency (η_{rad}) of an antenna can be expressed as [254]:

$$\eta_{rad} = 1 - \frac{P_{loss}}{P_{in}} \tag{62}$$

where P_{loss} and P_{in} are the loss power and input power, respectively. A lower tanδ reduces the dielectric loss power in the ceramic substrate, thereby increasing the antenna radiation efficiency. Furthermore, tanδ also affects the antenna gain. The gain G is related to the radiation efficiency by [254]:

$$G = \eta_{rad} D \tag{63}$$

where D is the directivity. Therefore, a lower tanδ leads to higher η_{rad}, and consequently contributes to a higher antenna gain. These relationships indicate that both ε_r and tanδ should be carefully considered when designing ceramic dielectric patch antennas, because they jointly determine the trade-off among miniaturization, bandwidth, radiation efficiency, and gain.

Guided by these design principles, a range of patch antennas have recently been designed and fabricated based on newly developed ceramics [260-288]. Depending on the feeding configuration, patch antennas can be categorized into microstrip-line feeding, aperture-coupled (slot-coupled) feeding, and coaxial-probe feeding. In Ref. [260], a microstrip-line-fed patch antenna operating at 6.3 GHz was designed on a $Y_{2.9}Mg_{0.1}Al_{4.9}Si_{0.1}O_{12}$-6wt%$TiO_2$ composite ceramic substrate for WiFi 6E/7 applications, as shown in **Fig. 21(a)**. Aperture-coupled feeding can effectively suppress feed-line radiation, improve isolation, and enhance the feasibility of multiband/wideband designs, and is therefore suitable for high-performance and highly

integrated systems; however, it features a relatively complex structure and imposes stricter requirements on interlayer alignment and fabrication precision. In Ref. [273], a rectangular aperture-coupled patch antenna was designed via simulation based on a 0.75LAB+0.25$CaTiO_3$ ceramic, as shown in **Fig. 21(b)**. It exhibits a center frequency of 6.54 GHz and a bandwidth of 140 MHz, with an antenna efficiency exceeding 87% and a maximum gain of 7.86 dBi, demonstrating the application potential of this dielectric antenna in microwave communications. Coaxial-probe feeding facilitates localized excitation and impedance matching, and is particularly suitable for thick substrates, array elements, and designs requiring flexible adjustment of the feed-point position. In Ref. [274], a coaxial-probe-fed patch element and its array were designed via simulation using a $LiGaSiO_4$ ceramic substrate; the structural model and $|S_{11}|$ are shown in **Fig. 21(c)(i)**. At a center frequency of 36 GHz, the array achieves a bandwidth of 1.17 GHz with a peak gain of 18.3 dBi. The normalized radiation patterns in **Fig. 21(c)(ii)** indicate sidelobe levels of -17 dB in the H-plane and -12.5 dB in the E-plane, suggesting low sidelobe radiation. Combined with the three-dimensional far-field gain distribution in **Fig. 21(c)(iii),** the array is further verified to exhibit a well-defined main-beam pointing along $\theta = 0°$.

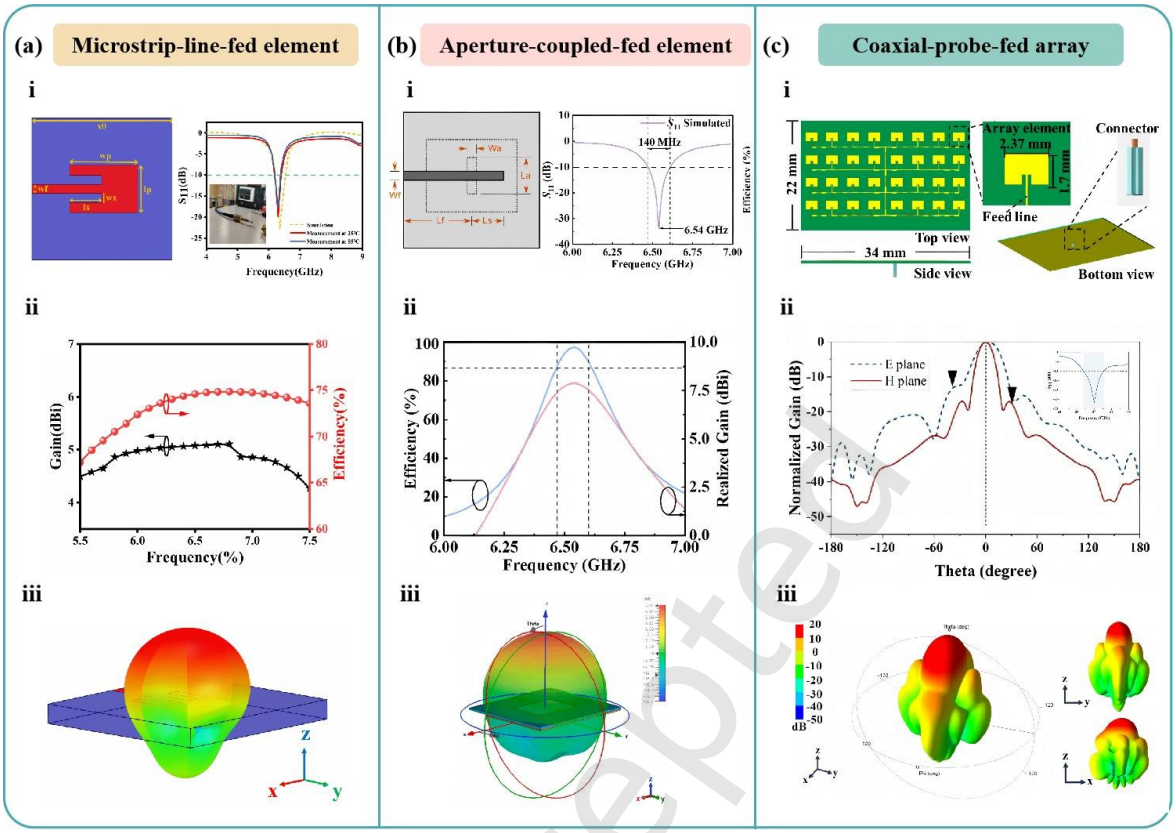

Figure 21. Patch antennas with different feeding configurations: (a) a microstrip-line-fed antenna element[260](Reproduced with permission from Ref. [260], © Elsevier Ltd. 2024.)and (b) an aperture-coupled antenna element[273](Reproduced with permission from Ref. [273], © Elsevier Ltd. on behalf of The editorial office of Journal of Materials Science & Technology 2025.), showing i) the model and reflection coefficient $|S_{11}|$, ii) gain and radiation efficiency, and iii) the 3D radiation pattern. (c) A coaxial-probe-fed antenna array [274](Reproduced from Ref. [274], © 2025 The Authors. Published by Elsevier B.V.), showing i) the model and reflection coefficient $|S_{11}|$, ii) normalized gain, and iii) the 3D radiation pattern.

Bandpass filters are employed to confine the operating band of a system, suppress out-of-band interference and noise, enhance receiver selectivity, and improve transmitter spectral purity, and thus represent the most commonly used filter type in RF front ends. Planar bandpass filters based on dielectric substrates can be broadly classified into distributed-parameter types, substrate integrated waveguide (SIW) types, and lumped-element types. Among them, distributed-parameter filters are constructed from half-wavelength or quarter-wavelength resonators of transmission lines such as microstrip lines and coplanar waveguides (CPWs) (e.g.,

parallel-coupled lines, interdigital, hairpin, open-loop, and stepped-impedance resonators). For coupled resonators, the coupling coefficient K can be calculated as [289]:

$$K = \frac{f_2^2 - f_1^2}{f_2^2 + f_1^2} \tag{64}$$

where f_1 and f_2 denote the lower and higher resonant frequencies, respectively. The signs $K < 0$ and $K > 0$ correspond to electric and magnetic coupling, respectively. The external quality factor (Q_e) can be expressed as [289]:

$$Q_e = \frac{\omega_0 \cdot \tau S_{11}(\omega_0)}{4} \tag{65}$$

where $\tau S_{11}(\omega_0)$ represents the group delay at the center angular frequency ω_0. Distributed-parameter planar filters feature mature structures, well-established design methodologies, and facile integration with planar circuits and antennas. Therefore, they provide a useful platform for evaluating the dielectric properties and application potential of newly developed microwave dielectric ceramic substrates. In recent years, a variety of distributed planar filters have been designed based on emerging microwave dielectric ceramics [290-295].

Ref. [295] reported a hairpin-type distributed bandpass filter fabricated on a $BaSc_2O_4$ ceramic, as illustrated in **Fig. 22(a)**. Simulation results indicate that at the operating frequency of 2.381 GHz, the return loss and insertion loss are −44.4 and 0 dB, respectively. Notably, the filter shows an unconventional positive temperature-coefficient frequency response: as the ambient temperature increases from -40 °C to 120 °C, the center frequency shifts from 2.36 GHz to 2.42 GHz, corresponding to an overall temperature coefficient of center frequency of 0.46 ppm/°C. This capability to tune the operating frequency without modifying the circuit topology arises from the synergistic effect between the temperature coefficient of resonant frequency of $BaSc_2O_4$ (τ_f = 167 ppm/°C) and the thermal expansion of metal electrodes. With increasing temperature, the substrate permittivity decreases, leading to an upward frequency shift. This feature offers distinctive potential for wireless communication systems operating over a wide temperature range.

In addition, substrate integrated waveguide (SIW) bandpass filters offer advantages such as high-quality factors and low radiation loss. Their cavity structures can be approximately modeled as dielectric-filled rectangular waveguide cavities. For a rectangular waveguide cavity, the resonant frequency of the TE/TM modes, f_{0mnp}, can be expressed as [296]:

$$f_{0mnp} = \frac{c_0}{2\sqrt{\mu_r \varepsilon_r}} \sqrt{\left(\frac{n}{w}\right)^2 + \left(\frac{m}{h}\right)^2 + \left(\frac{p}{l}\right)^2} \tag{66}$$

where μ_r is the relative permeability of the dielectric medium, and w, h, and l are the width, height, and length of the cavity, respectively. The integers n, m, and p denote the mode indices along the width, height, and length directions, respectively. Since microwave dielectric ceramics are generally non-magnetic materials, μ_r is usually taken as 1. When an SIW bandpass filter operates in the TE_{101} mode, its center resonant frequency can be obtained from the equivalent rectangular waveguide cavity model [297]:

$$f_{TE_{101}} = \frac{c_0}{2\sqrt{\mu_r \varepsilon_r}} \sqrt{\left(\frac{1}{w_{eff}}\right)^2 + \left(\frac{1}{l_{eff}}\right)^2} \tag{67}$$

where the effective width w_{eff} and effective length l_{eff} of the SIW cavity are given by [297]:

$$w_{eff} = w - \frac{d^2}{0.95s} \tag{68}$$

$$l_{eff} = l - \frac{d^2}{0.95s} \tag{69}$$

where s is the center-to-center spacing between two adjacent metallized via holes, and d is the diameter of the metallized via holes. The coupling coefficient K and external quality factor Q_e of SIW resonators can also be extracted using Eqs. 10 and 11, respectively.

Ref. [298] proposed a single-layer substrate integrated waveguide (SIW) resonator bandpass filter featuring negative coupling and a simple fabrication process, as shown in **Fig. 22(b)**. The design aims to reduce manufacturing complexity: the negative coupling is realized by introducing only a single slot on one side of the substrate, without increasing the number of substrate layers. With the proposed negative-coupling configuration, a single-layer SIW filter

with transmission zeros can be achieved without raising the fabrication difficulty. Nevertheless, SIW filters impose stringent requirements on via-hole machining accuracy and dimensional control, and their physical size remains relatively large.

Lumped-element filters employ interdigital capacitors, metal–insulator–metal (MIM) capacitors, and spiral or meander inductors to form equivalent LC resonators or networks. For an LC bandpass filter, the center resonant frequency f_{0LC} is determined by the resonant inductance L and capacitance C, and can be expressed as [299]:

$$f_{0LC} = \frac{1}{2\pi\sqrt{LC}} \tag{70}$$

when the capacitance C is realized using a dielectric structure, it can be written as:

$$C = \varepsilon_0 \varepsilon_r \frac{A}{d_c} \tag{71}$$

where ε_0 is the vacuum permittivity, A is the effective overlapping area of the two electrodes, and d_c is the thickness of the dielectric layer. When the inductance L and geometric dimensions are fixed, a higher ε_r leads to a larger capacitance C, thereby reducing the center resonant frequency f_{0LC}. Conversely, for a fixed target center frequency, increasing ε_r can reduce the electrode area A required to realize the desired capacitance, which is beneficial for the miniaturization of LC bandpass filters. Lumped-element filters offer compact size and are well suited for low-frequency miniaturization. However, their high-frequency performance and power-handling capability are often constrained by parasitic effects and the finite Q factors of lumped elements. To overcome these limitations, hybrid filters, also referred to as lumped–distributed filters, combine lumped and distributed parameters by loading capacitors or inductors onto transmission-line resonators, or by jointly leveraging stepped-impedance sections and lumped elements to realize resonance and coupling.

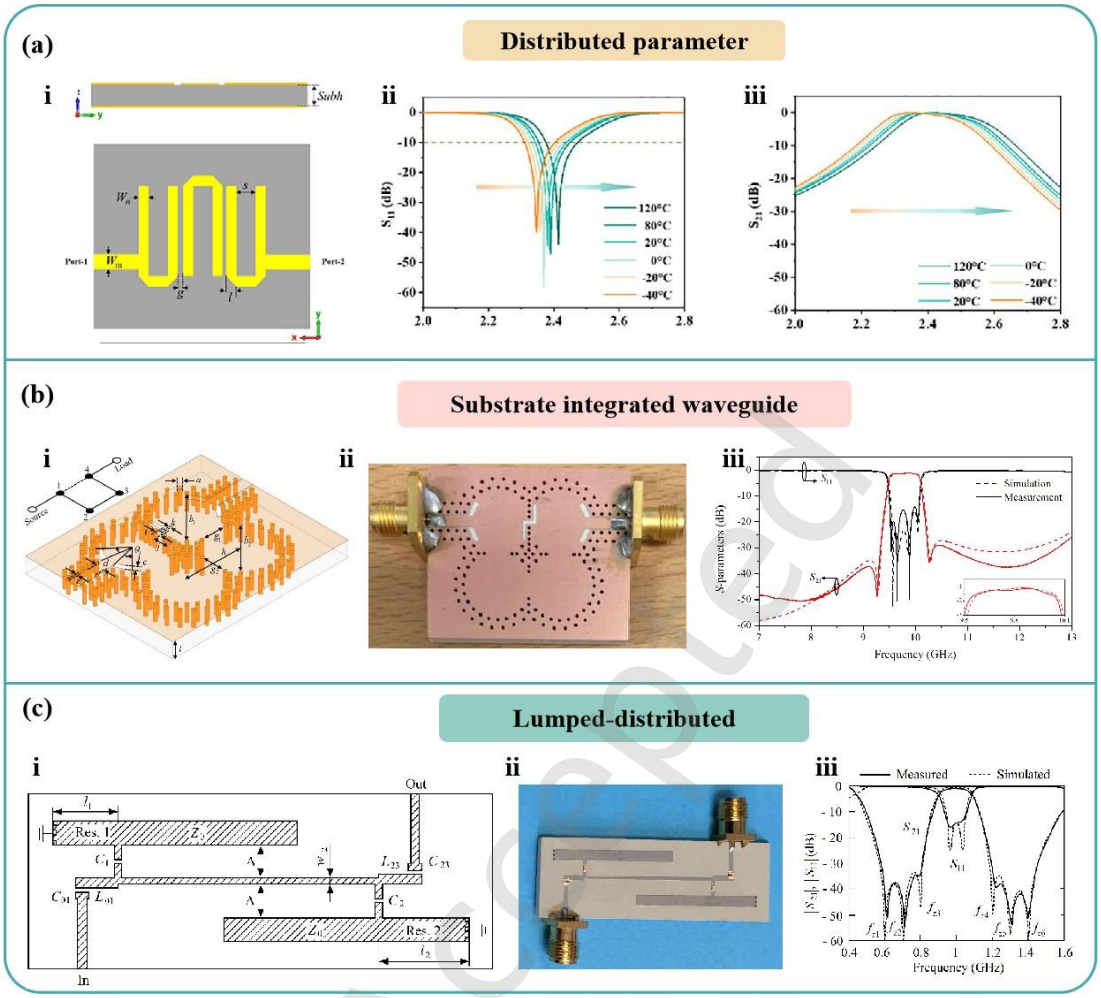

Figure 22. Planar bandpass filters with different architectures: (a) distributed-parameter filter: i) model, ii) $|S_{11}|$ at different temperatures, and iii) $|S_{21}|$ at different temperatures [295]. Reproduced with permission from Ref. [295], © Wiley-VCH GmbH 2026. (b) substrate integrated waveguide (SIW) filter: i) model and topology, ii) photograph of the fabricated prototype, and iii) S-parameter performance [298]. Reproduced with permission from Ref. [298], © IEEE 2025. (c) lumped–distributed filter: i) model, ii) photograph of the fabricated prototype, and iii) S-parameter performance [299]. Reproduced with permission from Ref. [299], © IEEE 2024.

Ref. [299] presented three types of lumped–distributed resonators; **Fig. 22(c)(i)–(iii)** show the structural model of the bandpass filter, a photograph of the fabricated prototype, and its S-parameters. These resonators introduce two transmission zeros (TZs) at finite frequencies in the transfer function of an in-line bandpass filter (BPF). When such resonators are used in a mixed-coupling bandpass filter without cross coupling, the number of transmission zeros can be increased from (N+1) to (3N+1), strengthening out-of-band suppression and improving filter

selectivity. In addition to antennas and filters, ceramic dielectric substrates are also widely used in passive components such as power dividers, duplexers, phase shifters, and couplers [300-303].

While the above examples mainly involve planar ceramic-substrate components, further miniaturization and functional integration can be achieved through LTCC technology, which enables multilayer stacking and three-dimensional interconnection by co-firing low-temperature sintered dielectric media with embedded metal electrodes. It can integrate transmission lines, resonant structures, passive networks, and packaging functions within a compact footprint, making it an important route toward RF front-end modularization. Compared with single-layer ceramic substrates, LTCC components offer smaller size and higher integration density, which in turn requires material systems to simultaneously satisfy co-firability, thermal-expansion matching, and long-term reliability. In recent years, passive components designed based on LTCC technology have primarily focused on typical architectures such as filters, antennas, duplexers, power dividers, couplers, and phase shifters.

LTCC filters can be regarded as multilayer implementations of dielectric-substrate filters, and they can be categorized into three types: lumped-element, substrate integrated waveguide (SIW), and distributed-parameter structures. Ref. [304] proposed a novel dual-band bandpass filter (D-BPF), as shown in **Fig. 23(a),** featuring two independently controllable transmission zeros (TZs). Closed-form equations were derived via even-/odd-mode analysis to validate the proposed theory. As a demonstration, a dual-band bandpass filter targeting 5G applications was designed, fabricated, and measured with center frequencies of 3.32/5.17 GHz and 3-dB fractional bandwidths of 25.45%/14.20%, respectively. Implemented using an LTCC process, the component occupies only 11.4 mm × 6 mm × 0.94 mm. Measurements indicate minimum insertion losses of 1.38 dB/1.53 dB at the two center frequencies, with return losses of 28 dB/23 dB, confirming both the feasibility of the proposed structure and its favorable performance.

To achieve high performance in the millimeter-wave band, Ref. [305] presented a low-loss, self-packaged Ka-band LTCC filter based on an artificial multimode SIW resonator, as depicted in **Fig. 23(b)**. Two ridges and two metal strip lines are densely integrated within a single SIW cavity, forming an artificial quad-mode resonator. Benefiting from the shielding of the SIW cavity, the resonator exhibits a high Q, enabling very low loss for the Ka-band filter. To verify the proposed approach, a 28-GHz filter was fabricated using LTCC technology. The measured insertion loss is as low as 0.8 dB, demonstrating strong appeal for millimeter-wave applications.

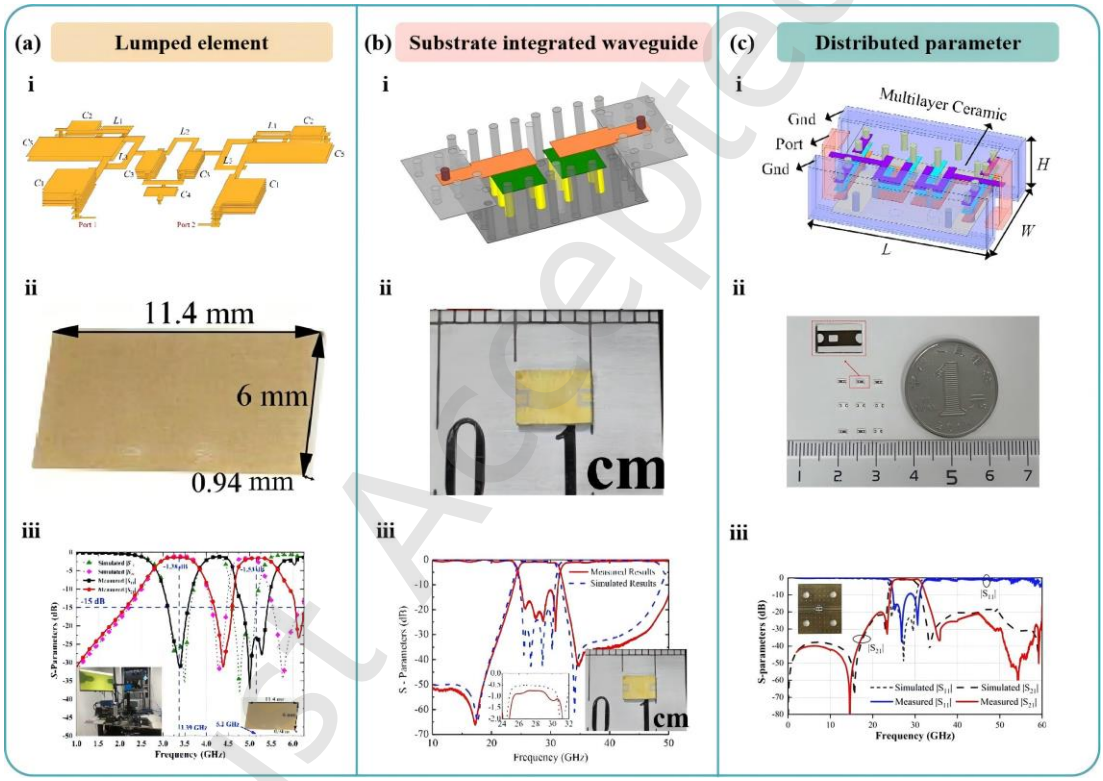

Figure 23. LTCC filters of different types: (a) lumped-element [304]; Reproduced with permission from Ref. [304], © IEEE 2022. (b) substrate integrated waveguide (SIW) [305]; Reproduced with permission from Ref. [305], © IEEE 2023. (c) distributed-parameter [306]. Reproduced with permission from Ref. [306], © Elsevier Ltd. 2024. For each filter: i) model; ii) fabricated prototype photograph; iii) S-parameter performance.

Furthermore, to realize a compact footprint and improved performance at millimeter-wave frequencies, Ref. [306] proposed a new highly selective, low-loss, and miniaturized millimeter-wave bandpass filter enabled by a $LiMg_{0.9}(Ni_{0.2}Co_{0.2}Zn_{0.2}Cu_{0.2}Mn_{0.2})_{0.1}PO_4$ ceramic and LTCC

processing, as shown in **Fig. 23(c).** The filter employs folded half-wavelength and quarter-wavelength stepped-impedance resonators (SIRs), and the multilayer integration capability of LTCC is leveraged to effectively reduce the size. To enhance selectivity, an additional cross-coupling path was introduced on top of a partial cross-coupling topology to form a fully cross-coupled topology. The design was analyzed using coupling-matrix synthesis and an equivalent-circuit model, yielding three transmission zeros in the vicinity of the passband. To validate the proposed design methodology, a 28-GHz bandpass filter was designed and fabricated, achieving a minimum insertion loss as low as 0.61 dB. Three transmission zeros are introduced on both sides of the passband, resulting in skirt selectivities of 25.50 dB/GHz and 10.47 dB/GHz, respectively, which improves frequency selectivity. The effective circuit area is only 1.44 mm × 1.0 mm (0.134 λ_0 × 0.093 λ_0), demonstrating miniaturization at millimeter-wave frequencies.

Beyond filters, LTCC technology is also highly attractive for antenna integration. Leveraging multilayer LTCC co-firing, the dielectric layers, metal layers, cavity structures, vertical interconnects, and feeding networks of antennas can be monolithically integrated in a three-dimensional manner. This endows LTCC antennas with clear advantages in millimeter-wave arrays, antenna-in-package (AiP), substrate integrated waveguide (SIW) slot arrays, and integrated horn implementations. In addition, the low-loss microwave dielectric ceramics used in LTCC reduce conduction and dielectric losses, enhancing radiation efficiency and gain. Current research mainly focuses on broadband and multi-band designs, circular-polarization realization, and co-optimization of array feeding networks and packaging [307-313]. For instance, Ref. [312] proposed a D-band dual-frequency SIC slot-antenna array for 6G IoT applications such as V2V/V2I. Dual-band radiation is achieved by exciting two higher-order radiation modes and arranging four radiating slots on the top layer of the cavity, while a vertically arranged SIW feeding network is adopted to reduce the overall size. The fabricated LTCC 2×2 array achieves gains of 12.1/12.4 dBi at 150.8/166.5 GHz, respectively, and the 1×4 array realizes beam pointing at -25° and -20° at 147.95/163.25 GHz with gains of 7.2 and 10.3

dBi, respectively. Ref. [313] presented a metasurface phased-array antenna (MSPAA) synthesis approach based on metasurface antenna (MSA) unit cells. To simultaneously achieve low profile, wide impedance bandwidth, and large-angle scanning, a patch–via-wall and blind-cavity configuration was introduced, and an 8×8 array was implemented using LTCC packaging with a profile height of only 0.1λ. Over 8~12 GHz (40%), the array supports ±45° scanning with active VSWR < 2.5, delivering a peak gain of 24.9 dBi and aperture efficiency exceeding 80%, while maintaining cross-polarization below -42.9 dB.

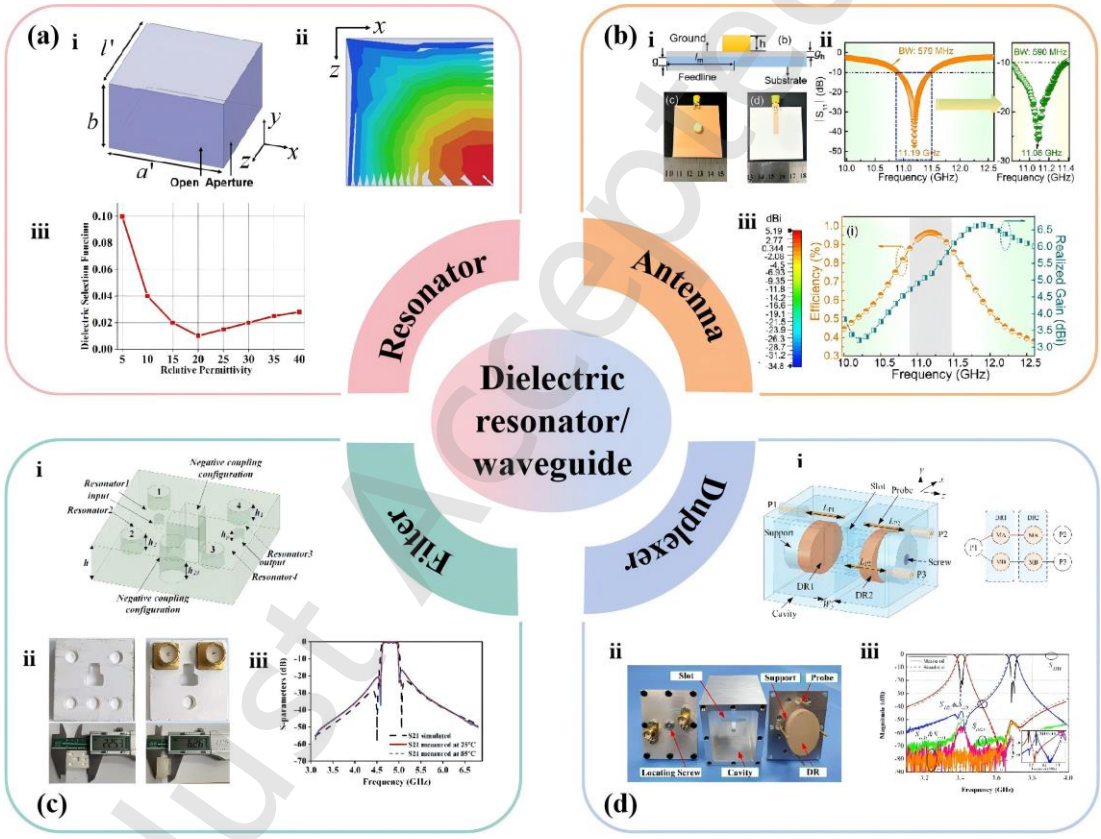

Figure 24. Dielectric resonant and dielectric waveguide components of different types: (a) resonator: i) model; ii) top view of the electric-field distribution for the TE_{101} mode; iii) dielectric selection function versus relative permittivity (ε_r), indicating that the material with $\varepsilon_r = 20$ is the most suitable [314]. Reproduced with permission from Ref. [314], © IEEE 2025. (b) dielectric resonator antenna: i) model; ii) simulated and measured $|S_{11}|$; iii) simulated gain and radiation efficiency [315]. Reproduced with permission from Ref. [315], © IEEE 2026. (c) dielectric waveguide filter: i) model; ii) fabricated prototype photograph; iii) simulated and measured $|S_{21}|$ at different temperatures (25 °C and 85 °C) [316]. Reproduced with permission from Ref. [316], © Elsevier Ltd. 2023.© 2023 Elsevier Ltd. All

rights reserved. (d) dielectric duplexer: i) model; ii) fabricated prototype photograph; iii) simulated and measured S-parameter performance [317]. Reproduced with permission from Ref. [317], © IEEE 2021.

In contrast to ceramic-substrate and LTCC components, where ceramics primarily serve as dielectric platforms or multilayer integration media, dielectric resonant and dielectric waveguide components employ high-Q dielectric ceramics as the core resonant elements and exploit electromagnetic standing-wave resonances to realize functions such as frequency selectivity and radiation. Therefore, they represent an important technological route toward low insertion loss in microwave passive components. Such components typically require materials with high $Q\times f$ and near-zero τ_f to reduce insertion loss and suppress temperature drift. Meanwhile, by tuning the ε_r and the structural dimensions, a trade-off between miniaturization and bandwidth can be achieved. Representative forms include dielectric resonators, dielectric resonator antennas, dielectric filters, and dielectric duplexers, as exhibited in **Fig. 24** [314-317].

Rectangular and cylindrical dielectric resonator antennas are commonly used to validate the dielectric properties and application potential of newly developed microwave dielectric ceramics. For a rectangular dielectric resonator antenna, the lowest-order resonant mode (TM_{101}) is often employed, and its resonant frequency can be expressed as [259]:

$$f_{r101}^{\mathrm{TM}}=\frac{c_0}{2\sqrt{\mu_r\varepsilon_r}}\sqrt{\left(\frac{1}{a}\right)^2+\left(\frac{1}{2d}\right)^2} \tag{72}$$

where a and d denote the lateral dimension and height of the rectangular dielectric resonator antenna, respectively, with d being the height perpendicular to the ground plane.

For a cylindrical dielectric resonator antenna, the commonly used modes include the $TE_{01\delta}$, $TM_{01\delta}$, and $HE_{11\delta}$ modes, whose resonant frequencies can be expressed as [259]:

$$f_{r01\delta}^{\mathrm{TE}}=\frac{c_0}{2\pi a_R}\left(\frac{2.327}{\sqrt{\varepsilon_r+1}}\right)\left[1+0.2123\left(\frac{a_R}{h}\right)-0.00898\left(\frac{a_R}{h}\right)^2\right];\quad 0.125\le\frac{a_R}{h}\le 5 \tag{73}$$

$$f_{r01\delta}^{\mathrm{TM}}=\frac{c_0}{2\pi a_R}\left(\frac{1}{\sqrt{\varepsilon_r+2}}\right)\sqrt{\left[(3.83)^2+\left(\frac{\pi}{2}\right)^2\left(\frac{a_R}{h}\right)^2\right]};\quad 0.125\le\frac{a_R}{h}\le 5 \tag{74}$$

$$f_{r11\delta}^{\mathrm{HE}}=\frac{c_0}{2\pi a_R}\left(\frac{6.324}{\sqrt{\varepsilon_r+2}}\right)\left[0.27+0.18\left(\frac{a_R}{h}\right)+0.005\left(\frac{a_R}{h}\right)^2\right];\quad 0.125\le\frac{a_R}{h}\le 5 \tag{75}$$

where a_R and h represent the radius and height of the cylindrical dielectric resonator antenna, respectively. Therefore, the initial dimensions of a dielectric resonator antenna can be estimated according to the target resonant frequency and the dielectric constant of the ceramic material. In addition, for dielectric waveguide resonators, filters, and duplexers, the initial resonator dimensions can be estimated using Eq. 66, while the coupling coefficient K and external quality factor Q_e can be extracted using Eqs. 64 and 65, respectively. These initial values can then be further optimized through full-wave electromagnetic simulation to meet the required frequency response, bandwidth, and insertion-loss specifications.

As for the synergistic design of metamaterial topology for novel electromagnetic responses, the expansion of microwave dielectric ceramics into metamaterials is not merely a substitution of materials but introduces a new, synergistic design dimension. The intrinsic properties of the ceramic, specifically its complex permittivity (the real part ε_r and the imaginary part represented by the $Q\times f$ value), become active tuning parameters alongside the geometric dimensions of the meta-atom. This synergy enables access to exotic electromagnetic states that are difficult to achieve otherwise. A prime example is the excitation of anapole states, characterized by a suppressed far-field radiation pattern due to destructive interference between fundamental multipole moments, which can be harnessed for strong near-field confinement and perfect absorption. Luo *et al.* pioneered the realization of such states in a monolithic ceramic system. They designed a metamaterial comprising an array of high-ε_r ceramic ($Ba_4Eu_1Nd_{8.33}Ti_{17}Al_{0.4}Ga_{0.6}O_{53.5}$) meta-atoms. By strategically designing the meta-atom's geometry (acting as a capacitive element) and synergistically exploiting the dielectric loss (tunable via the ceramic's $Q\times f$ value), they constructed a hybrid anapole mode (In some research, it is called Lattice Anapole, but from this design perspective rather than physics, we believe that Hybrid Anapole is more appropriate). In **Fig. 25**, the loss acts as a lumped resistance

in an equivalent circuit model, allowing critical coupling to be achieved. This integrated insulated materials-by-design approach resulted in perfect absorption (A ≈ 99%) in the millimeter-wave band (near 30 GHz), as conclusively demonstrated by the measured scattering parameters and the derived impedance matching condition ($Z_{eff} \approx 1$). Furthermore, owing to the excellent temperature stability of the tailored tungsten bronze ceramic ($\tau_f \approx +6.6$ ppm/°C), the anapole metamaterial absorber maintained high performance (> 95% absorbance) up to 220 °C with minimal frequency drift. This work fundamentally shifts the perspective on dielectric loss: in this context, it is not a passive, undesirable material parameter but a crucial, active degree of freedom for tailoring the electromagnetic response of the metamaterial. It illustrates a co-design philosophy where ceramic synthesis targets specific (ε_r, $Q \times f$) pairs to enable desired metamaterial functionalities, a significant departure from the traditional goal of minimizing loss for resonator applications [318].

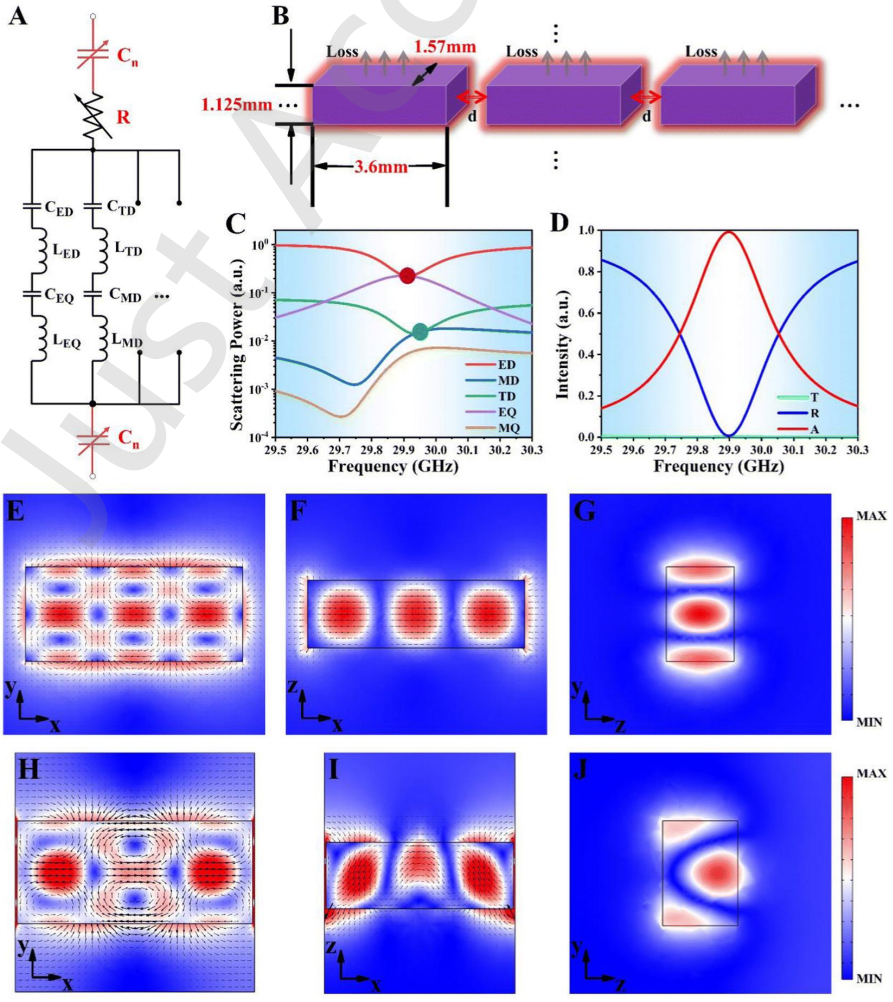

Figure 25. (A) Lumped element equivalent circuit model of metamaterial perfect absorber based on BENT-AG ceramics. (B) Details and geometric parameters of metamaterial perfect absorber. (C) Multipole decomposition results and (D) simulated transmittance, reflectance, and absorbance of BENT-AG-based metamaterial perfect absorber in free space. Combined performance for $\varepsilon_r = 70$, $Q \times f = 6200$ GHz, and the period is 3.66 mm. E-field distribution (E–G) based on eigenmode analysis and (H–J) in meta-atom array in *xy*, *xz*, and *yz* planes, respectively [318]. Reproduced with permission from Ref. [318], © Royal Society of Chemistry 2023.

From discrete components to monolithic, extreme-environment metamaterials, the application of microwave dielectric ceramics has transcended their traditional role as passive resonators or substrates in conventional electronics. A transformative frontier is their direct integration as the sole constituent in architecting all-dielectric, all-ceramic metamaterials. This approach directly addresses a critical bottleneck in the deployment of functional electromagnetic devices, such as perfect absorbers or sensors, in extreme environments involving high temperatures, thermal shock, and oxidizing atmospheres. Conventional metamaterials often rely on multi-material composites (e.g., metal-dielectric stacks or supported functional layers) where mismatched thermal expansion coefficients and material degradation under thermal stress lead to catastrophic failure. The innovative work by Luo et al. demonstrates a paradigm where the metamaterial itself is a monolithic, single-phase ceramic piece engineered with sub-wavelength features. In their seminal work, a "desymmetrized" metamaterial was fabricated from a tungsten bronze-based ceramic plate into which a periodic array of blind holes was machined with high precision. This simple, substrate-free design embodies the powerful principle that "the device tolerance temperature equals the material tolerance temperature." The microwave dielectric ceramic provides not only the desired permittivity and low loss but also the intrinsic high melting point and chemical stability. The metamaterial's functionality arises from a carefully engineered symmetry breaking (D4v), which, within the theoretical framework of bound states in the continuum (BIC) and the generalized Kerker effect, allows for the coherent superposition of odd and even multipolar

modes (e.g., electric and magnetic dipoles/quadrupoles). At a singular point, this interference leads to a transverse scattering mode, manifesting as near-perfect absorption (>99%) with suppressed both reflection and transmission. Crucially, as shown in **Fig. 26**, this absorption performance remains remarkably stable after ten thermal cycles at 1300 ℃ and even after severe thermal shock followed by a repair process [319]. This level of robustness, unattainable with composite or metal-based counterparts, underscores the unique value proposition of using bulk-engineered microwave dielectric ceramics to create ultra-resilient electromagnetic devices for aerospace, propulsion, and energy systems [151].

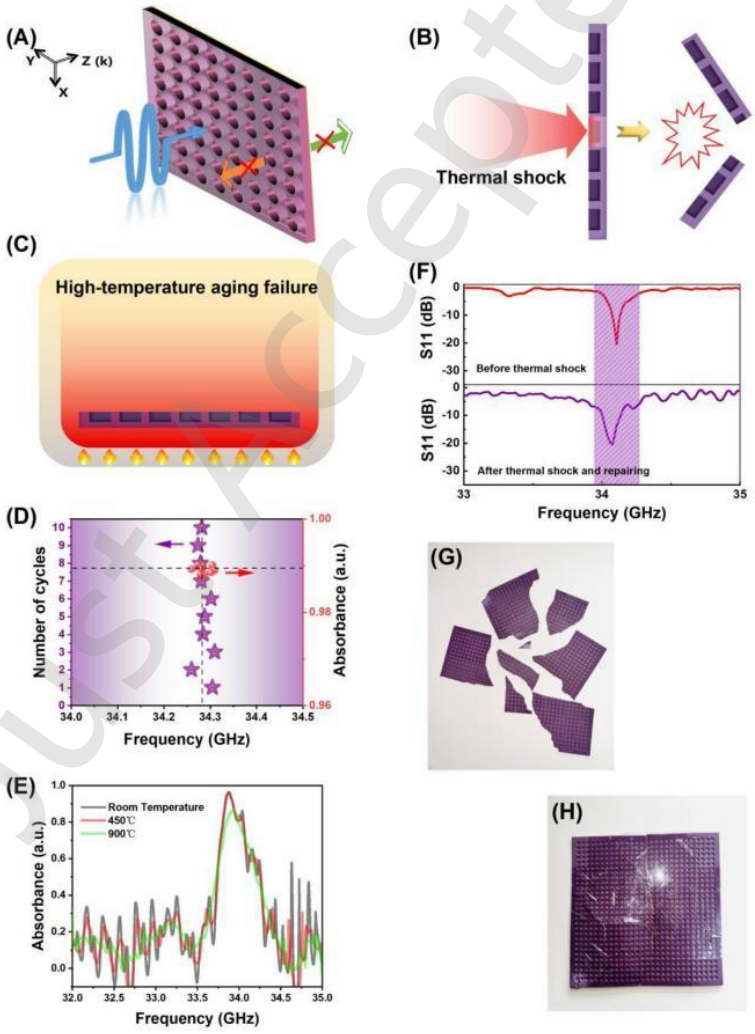

Figure 26. (A) structural and functional diagram of desymmetrized metamaterials. Reliability demonstration: typical matching extreme (high temperature) environments of (B) thermal shock and (C) high-temperature aging failure. (D) 10 cycles of high temperature performance. (D) Results of in-situ absorption measurements from room temperature to 900°C. (F) the S11 results before and after thermal shock and repairing. Images of

sample (G) after thermal shock and (H) repairing [319]. Reproduced with permission from Ref. [319], © Wiley-VCH GmbH 2026.

The foray of microwave dielectric ceramics into the realm of metamaterials represents a profound expansion of their utility. They have evolved from being mere enabling materials to becoming the central, active component in creating artificial materials with unprecedented properties. The demonstrated pathways—constructing monolithic, extreme-environment devices through macroscopic symmetry engineering and accessing novel electromagnetic states like anapoles via synergistic property-structure design—establish microwave dielectric ceramics as a versatile and powerful platform for the next generation of robust, high - frequency, and functional electromagnetic devices.

Although significant progress has been achieved in the component-oriented applications of microwave dielectric ceramics, several challenges remain to enable further advances toward higher-performance component design. For conventional microwave components (substrates, LTCC modules, and dielectric resonators), first, strong capability is required for the co-optimization and batch-to-batch consistency of key dielectric properties, so as to mitigate center-frequency deviations, temperature drift, and yield degradation caused by sintering shrinkage and microstructural fluctuations. Second, to address the demands of high-frequency operation and miniaturization, materials–component co-design for miniaturization should be pursued to alleviate bandwidth narrowing and increased insertion loss that may arise from relying solely on higher ε_r. Third, in packaging and system-integration scenarios such as LTCC/AiP/SiP, joint electromagnetic–circuit co-modeling and optimization across the component, package, and PCB should be advanced, accelerating the transition of passive components from discrete implementations to multifunctional integration, modularization, and system-level high density integration. For emerging metamaterial devices based on microwave dielectric ceramics, additional challenges arise. First, the fabrication of monolithic all-ceramic metamaterials requires high-precision machining (e.g., drilling sub-wavelength hole arrays)

without introducing microcracks or surface defects that degrade dielectric loss. Second, while the co-design of ceramic properties (ε_r, $Q\times f$, τ_f) and meta-atom geometry enables novel electromagnetic responses (anapole states, bound states in the continuum, perfect absorption), a systematic design methodology linking material synthesis targets to metamaterial functionalities is still lacking. Third, although ceramic-based metamaterials demonstrate exceptional thermal stability (e.g., up to 900 °C), long-term reliability under cyclic thermal shock, oxidation, and mechanical vibration in real-world extreme environments (aerospace, propulsion) requires further validation. Addressing these challenges will unlock the full potential of microwave dielectric ceramics as a platform for next-generation resilient and functional electromagnetic devices.

2.5 Frontier: Machine Learning Driven Materials Development

As materials science transitions into the data-driven "fourth paradigm", machine learning (ML) offers a transformative pathway for the design of functional ceramics. While traditional trial-and-error and computational methods face limitations in handling complex, high-dimensional design spaces, data-driven approaches enable the extraction of hidden correlations and rapid property prediction. This section reviews the progress in predicting key performance metrics of dielectric ceramics, ε_r, $Q\times f$, and τ_f values, highlighting the evolution from compositional mapping to physics-informed modeling.

Early data-driven predictions of permittivity primarily relied on compositional descriptors and targeted accelerated screening within specific solid-solution systems [320-322]. Regression models such as SVR have effectively balanced high ε_r and near-zero τ_f in systems like (Ca,Nd)TiO_3 and cordierite by navigating narrow composition windows (**Fig. 27a and 27b**) [323, 324]. With growing interest in capturing more complex composition-property relationships, deep learning approaches began to attract attention. An attention-integrated CNN developed for spinel ceramics emulated physical intuition by assigning higher weights to active cations, reducing prediction errors by ~20% compared with baseline models (**Fig. 27c**) [325].

However, when extended to heterogeneous datasets, composition-only models exhibit sharply increased errors [326, 327], revealing that while compositional descriptors capture lattice distortions within isostructural solid solutions, they fail to represent distinct polarization mechanisms associated with different structural units, such as corner-sharing octahedra versus isolated tetrahedra.

To overcome these limitations, recent studies have shifted toward incorporating explicit structural descriptors to capture the underlying physics of polarization. Qin *et al.* [328] incorporated physics-informed features, including molecular dielectric polarizability per unit volume (*ppv*), average bond length (*blm*), and atomic cell volume (*va*), into an SVR model that outperformed the classical Clausius−Mossotti equation (**Fig. 27d and 27e**). These descriptors clarified that lower *ppv* reduces ionic polarization density, while shorter *blm* increases bond stiffness and suppresses cation displacement. Building on this framework, a correction term for the C−M equation was derived via symbolic regression, demonstrating the potential of ML to refine classical dielectric theory [329]. While Sheng *et al.* [330] employed formula-splitting strategies to construct high-dimensional features without explicit structural inputs, enabling descriptor construction when crystallographic information is incomplete. Within specific structure families, models integrating physics-informed features, such as atomic radius, electronegativity, and ionization energy achieved high accuracy for spinels and perovskites [331, 332]. Transitioning from handcrafted descriptors to automated representations, graph neural networks (GNNs) have been introduced to model structure-property relationships directly from crystal topology. Xi *et al.* [333] applied a RGCN to link permittivity in molybdates and vanadates to network connectivity and strong covalent bonding, while Liu *et al.* [334] utilized a CGEN model with GNNExplainer to identify specific elemental contributors in titanates. However, while these models capture lattice connectivity, challenges remain in handling structural disorder. For instance, Riebesell *et al.* [335] identified $Bi_2Zr_2O_7$ using Wren Deep Ensembles but noted discrepancies between predicted ordered structures and

experimentally observed disordered phases, highlighting the limitations of GNNs trained primarily on idealized crystallographic data.

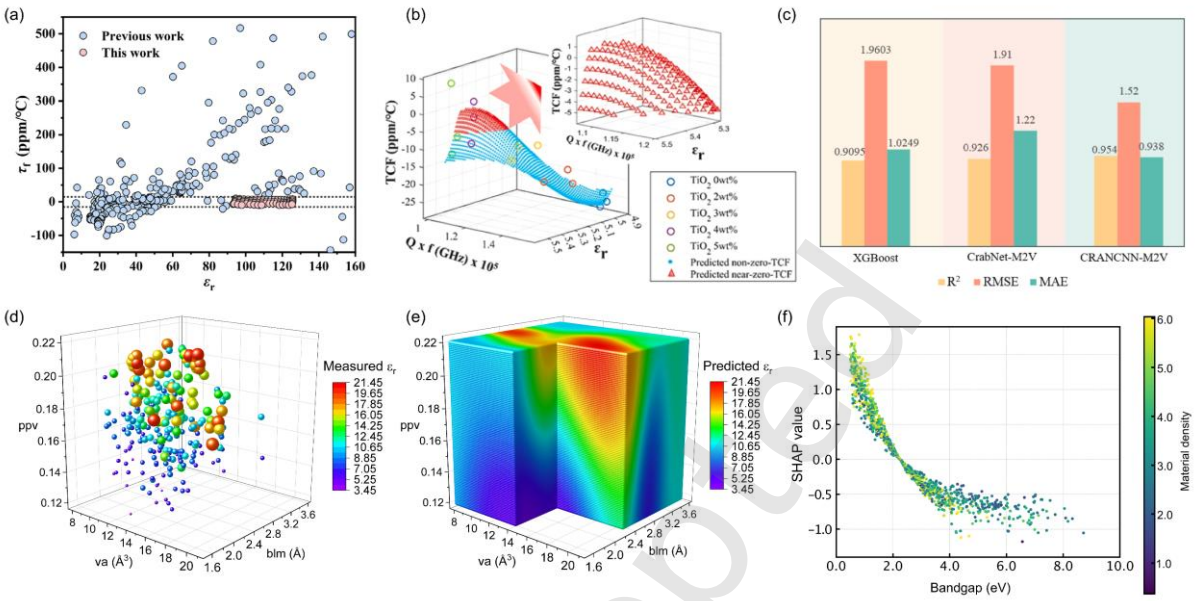

Figure 27. (a) Comparison of microwave dielectric properties between previously reported perovskite and ML-identified $(Ca_{0.7}Nd_{0.2})TiO_3$-based ceramics [323]. Reproduced with permission from Ref. [323], © The American Ceramic Society 2024. (b) Distribution of ML-predicted microwave dielectric properties for $Mg_2Al_3Si_5O_{18}$-TiO_2 based ceramics [324]. Reproduced with permission from Ref. [324], © Elsevier Ltd. 2025. (c) Comparison of model performance for spinel microwave dielectric ceramics [325]. Reproduced with permission from Ref. [325], © Elsevier Ltd. 2025. (d) Measured permittivity in a 3D feature space. (e) Predicted permittivity in 3D feature space [328]. Reproduced with permission from Ref. [328], © The Chinese Ceramic Society and Elsevier B.V. 2021. (f) SHAP values of bandgap to electronic contribution of permittivity [336]. eproduced with permission from Ref. [336], © AIP Publishing 2020.

Bridging the gap between idealized lattice models and experimental performance requires disentangling intrinsic polarization from extrinsic microstructural effects. One strategy introduces processing conditions as indirect descriptors for unmeasured microstructures. Kireeva *et al.*[337] demonstrated that including calcination and sintering parameters improves predictive performance but yields structure-dependent responses; in defect-sensitive systems like X8R $BaTiO_3$ [338] and rock-salt ceramics [339], sintering temperature can become a more critical predictor than composition itself. Liu *et al.*[340] further improved accuracy by

designing physics-informed kinetic descriptors that quantify the thermal budget. In parallel, first-principles calculations provide a complementary route by isolating intrinsic mechanism. Noda *et al.*[341] showed that permittivity arises from an interplay between electronic delocalization and local bonding. To address domain shift in general models, Kim *et al.*[342] showed that retraining with domain-specific data and structural descriptors sensitive to octahedral distortions markedly improves predictive accuracy. Within focused domains, Lin *et al.*[343] and Yao *et al.*[344] established inverse correlations between permittivity and electronic features in quantitative agreement with the classical Penn model. Furthermore, Takahashi *et al.*[345] and Shimano *et al.*[346] showed that electronic polarization depends on macroscopic descriptors, while ionic polarization depends on local heterogeneity. Incorporating such domain knowledge into feature engineering improves both accuracy and interpretability: SHAP analysis revealed that ε_{el} correlates positively with theoretical density and negatively with bandgap (E_g), also in agreement with the Penn model (**Fig. 27f**) [336], enabling the identification of exceptional materials combining high permittivity and wide band gaps [347].

Predicting $Q \times f$ value (or tanδ) is more challenging due to its sensitivity to multiscale structural features, defects, and local symmetry breaking. Traditional heuristics based on lattice rigidity or packing density often fail to provide quantitative guidance, motivating ML approaches to capture non-linear coupling between lattice anharmonicity and dielectric loss. However, early composition-based models, largely adapted from permittivity prediction, struggle to represent defect- and structure-dependent contributions. Within narrowly defined systems, ML models achieved high accuracy for $BaTiO_3$, $(Zr_{0.7}Sn_{0.3})TiO_4$ and $(Ca_{0.7}Nd_{0.2})TiO_3$ ceramics, but these results derived from small and homogeneous datasets primarily reflect local compositional trends and lack generality [320, 322-324]. Recognizing the path-dependent nature of dielectric loss, Liu *et al.*[340] incorporated thermal-history descriptors into a Gaussian kernel ridge model for LTCCs, achieving $R^2 = 0.91$ for design of low-ε_r, low-tanδ ceramics (**Fig. 28a**), underscoring the importance of processing-informed features. To improve physical

interpretability, recent studies quantified local structural environments. Guo *et al.* [348] constructed a self-consistent dataset for the $Li_4SrCaSi_2O_8$ system and built an interpretable decision tree model (**Fig. 28b**). The Si/Li atomic mass ratio, Si/Sr ionic radius ratio, and total cation electronegativity were identified as key descriptors. Increasing the Si/Li mass ratio and Si–O bond covalency suppresses anharmonic lattice vibrations, leading to a Sn^{4+}-doped ceramic with a high $Q \times f$ of 83,526 GHz. Qin *et al.*[349] investigated gillespite-type $(Ca_xSr_{1-x})CuSi_4O_{10}$ ceramics, where substituting Ca^{2+} for Sr^{2+} distorted the $[(Ca,Sr)O_8]$ dodecahedra while preserving the rigid silicate framework. An SVR model identified the A−O2 bond length and bond length variance as decisive, showing that shorter, stiffer bonds and optimized polyhedral distortion suppress lattice vibrations and energy dissipation. This mechanism-based model extrapolated to isostructural $(Ba_ySr_{1-y})CuSi_4O_{10}$ (**Fig. 28c**). However, expanding structural diversity often reduces accuracy due to the difficulty of defining universal descriptors. Mo *et al.*[350] compromised this challenge in the ABO_4 family, which spans scheelite, wolframite, and zircon structures but shares chemical connectivity. Their SVR model balanced generality and accuracy by combining primitive cell volume, molecular polarizability, and average electronegativity, showing that larger cell volumes reduce phonon-phonon collisions and enhance $Q \times f$ (**Fig. 28d**). Broader universality remains challenging. Sheng *et al.* [330] achieved only moderate performance ($R^2 = 0.4$) for 725 quaternary compounds using element-based SISSO descriptors, highlighting the limitations of composition-only models across diverse systems. Given the high computational cost of first-principles dielectric loss calculations, Oba *et al.*[351] employed transfer learning on two-phonon density of states to predict intrinsic $\tan\delta$ ($R^2 = 0.828$), although this approach captures only the thermodynamic lower limit by neglecting extrinsic defects and grain boundaries.

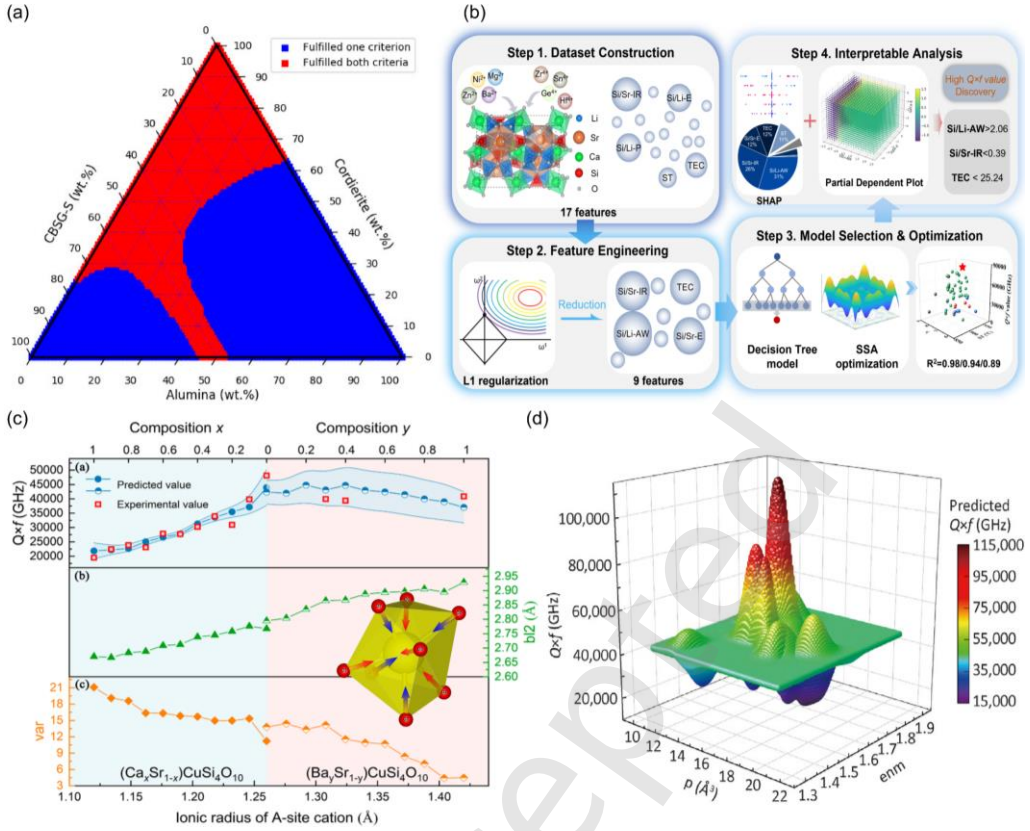

Figure 28. (a) Contour plot of LTCCs composed of CaO-B_2O_3-SiO_2 glass (CBSG-S), cordierite, and alumina [340]. (b) Schematic illustration of an interpretable framework for the $Q\times f$ value prediction of $Li_4SrCaSi_2O_8$ microwave ceramics, where four steps include dataset construction, feature engineering, model selection & optimization, and interpretable analysis. (c) Experimental and predicted Q×*f* values, A−O2 bond length and variance of A−O bond lengths of $(Ca_xSr_{1-x})CuSi_4O_{10}$ and $(Ba_ySr_{1-y})CuSi_4O_{10}$ ceramics [349]. Reproduced with permission from Ref. [349], © American Chemical Society 2021. (d) Model predicted $Q\times f$ values in the virtual space of *p* and *enm* of ABO_4 ceramics [350]. Reproduced from Ref. [350], © 2024 The Authors. Published by Elsevier B.V. on behalf of The Chinese Ceramic Society.

Data-driven modeling of τ_f value is still less developed, as temperature coefficients are derivative properties sensitive to both intrinsic structural distortions and extrinsic processing conditions. Ni *et al.*[323] employed SVR to quantify how site-specific substitutions reduce the τ_f in perovskite ceramics, while Appiah *et al.*[324] demonstrated that sintering temperature is a key descriptor for tuning τ_f in cordierite ceramics, achieving high predictive accuracy (R^2 > 0.94) by capturing phase evolution during firing. However, purely compositional models fail once structural phase transitions occur. Physics-informed descriptors that encode local

distortions have therefore been introduced. Yang *et al.*[352] showed that a bond-length-based tolerance factor of ABO_3 ceramics outperforms traditional ionic metrics by reflecting octahedral tilting, while feature analysis highlighted the role of molecular dielectric polarizability in modulating τ_f via permittivity. For broader ceramic systems, SISSO models relying solely on elemental features achieved limited accuracy ($R^2 = 0.57$), underscoring the inability of pure compositional descriptors to generalize in complex systems [330]. Kireeva *et al.*[337] incorporated calcination and sintering parameters as processing-derived descriptors, achieving a much higher performance ($R^2 = 0.79$) across seven material families. Their analysis showed that processing history influences τ_f much more than permittivity. This reflects that τ_f is more sensitive to processing history than permittivity.

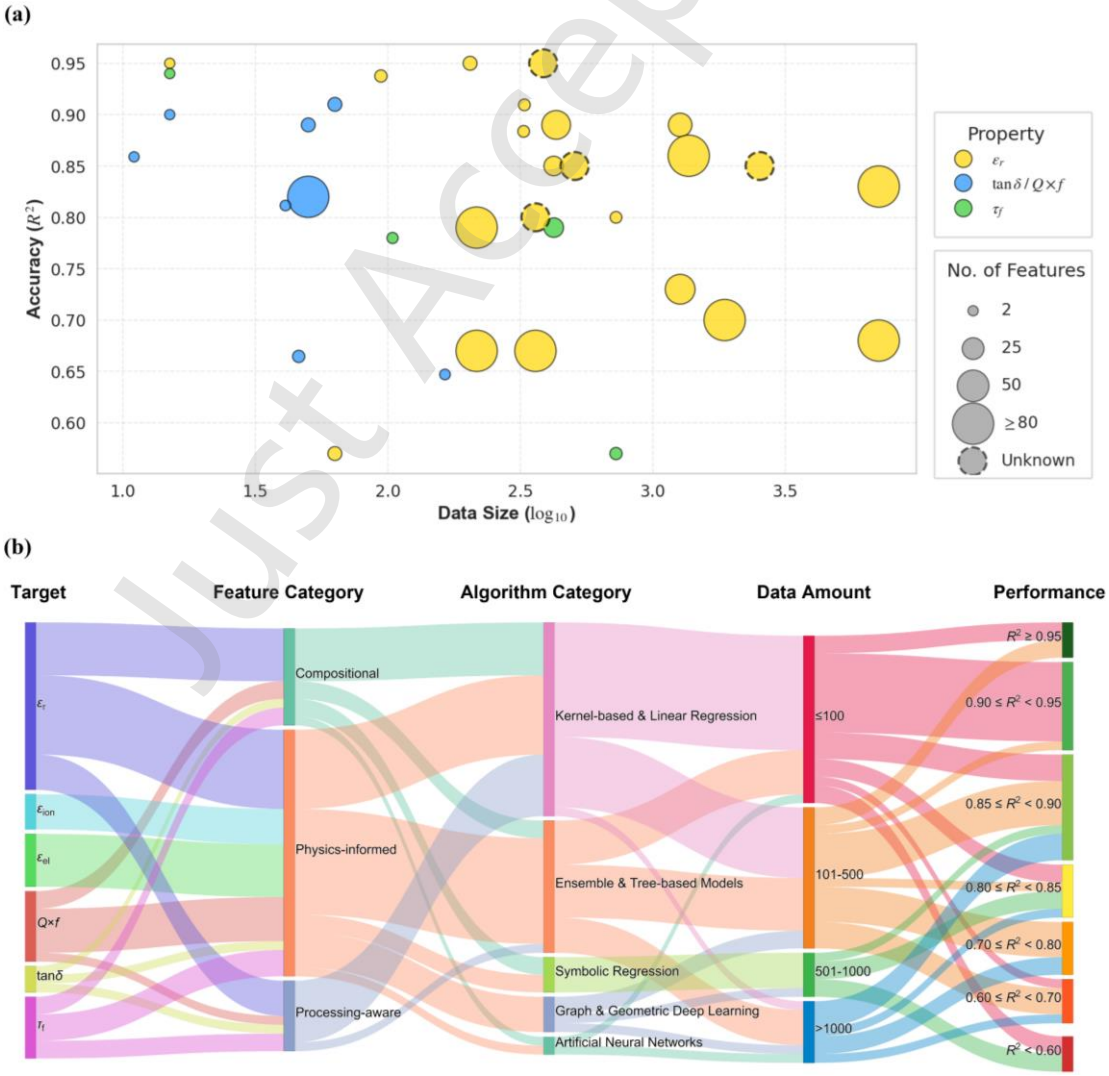

Figure 29. Performance benchmarking of ML models for microwave dielectric properties: (a) Relationship between data size, feature complexity, and predictive accuracy; (b) Sankey diagram illustrating the mapping from targets and features to algorithmic performance.

To evaluate the current modeling capabilities for microwave dielectric ceramics, we systematically cataloged representative machine learning studies in **Table 4** and analyzed their performance landscape in **Fig. 29.** The table summarizes key parameters including material systems, specific dielectric targets, algorithms, data sources, and the dimensionality of feature sets. As visualized in **Fig. 29(a),** the benchmarking results reveal a complex relationship between dataset size, feature complexity, and predictive accuracy (R^2), highlighting both the progress of data-driven approaches and the sparse regions in the current data landscape where further efforts are needed. **Fig. 29(b)** further elucidates the architectural mapping between modeling strategies and outcomes. While ε_r prediction is predominantly driven by physics-informed features, $Q \times f$ and τ_f rely on a more balanced integration of compositional and processing-aware descriptors. In terms of algorithmic deployment, kernel-based and linear regression models are the primary choice for small-scale datasets, frequently delivering high precision ($R^2 > 0.90$). Ensemble methods and deep learning architectures manage larger data volumes, bridging diverse feature categories to maintain robust performance across broader chemical and structural spaces.

In summary, data-driven modeling of dielectric properties is evolving from black-box compositional mapping toward structurally and physically informed frameworks, yet major challenges remain in reconciling idealized lattice physics with experimental reality. While ML can predict permittivity with high accuracy in constrained domains, achieving both universality and precision remains difficult due to topological diversity. Predicting $Q \times f$ and τ_f is further complicated by lattice anharmonicity and derivative effects that static descriptors cannot fully capture. A fundamental limitation across all three properties is the inadequate representation of extrinsic factors, including defects, grain boundaries, and processing history. Future progress

therefore requires hybrid, physics-aware models that integrate comprehensive datasets with domain knowledge to explicitly decouple intrinsic lattice contributions from extrinsic microstructural effects, enabling reliable and generalizable MWDC design.

Table 4. Summary of prediction models for microwave dielectric properties.

Materials	Target	Algorithm	Data Source*	Data Amount	Performance	Key Features (No. of total features)	Ref.
Universality	ε_r	ANN	E	700	RMSE = 16	Molar ratio of elements (16)	[327]
Universality	ε_r	SVR.RBF	E	254	r = 0.7638 RMSE = 2.54	Polarizability per unit volume, Average bond length, Average cell volume per atom (3)	[328]
Five crystal systems	ε_r	SVR.RBF	E	422	R^2 = 0.85 RMSE = 4.84	Compositional, Structural, Atomic, Heat-treatment features (20)	[337]
ABO_3-based	ε_r	SVR.RBF	E	325	R^2 = 0.8837 RMSE = 10.3	Atomic radius, Electronegativity, Ionization energies (5)	[332]
Universality	ε_r	Res-GCN	E	360	R^2 = 0.8 RMSE=1.8726	Encoded atomic features (electronegativity, radii, valence) and bond distances (Crystal Graph)	[333]
Universality	ε_r	CGEN	C+E	506	R^2 = 0.85 RMSE = 3.74 MAE = 2.60	Electron affinity, Outermost electrons, Electronegativity	[334]
$CaTiO_3$-based	ε_r	SVR.RBF	E	20	RMSE = 2	Molar ratio of elements (2)	[323]
Spinel	ε_r	XGBoost	E	327	R^2 = 0.9095 RMSE = 1.96	Atomic radius, Electronegativity, Ionization energies (5)	[331]
Glass ceramics	ε_r	GKRR	E	63	R^2 = 0.57	Concentrations of ceramic filler, Glass phase and processing parameters (9)	[340]
Universality	ε_r	ANN	C	1864	R^2 = 0.7	Magpie descriptors (100)	[347]
Quaternary materials	ε_r	SISSO	E	725	R^2 = 0.8	Element ratio, Coordination number, Mass attenuation coefficient, Chemical potential, Polarizability (5)	[330]
ABO_3-based	ε_r	Partial LSR	C	360	R^2 = 0.67 RMSE = 0.63	Cohesive energy, Ionic radii of A and B cations (1208)	[341]
Spinel	ε_r	CRANCN N-M2V	E	385	R^2 = 0.95 RMSE = 1.52	Data embedding methods	[325]
$BaTiO_3$-based	ε_r	BP-ANN	E	21	r = 0.9998*** RMSE = 19.34	Concentrations of five additives (5)	[320]

$BaTiO_3$-based	ε_r	*k*NN	E	2123	R^2 = 0.961	Dopant concentrations, Sintering temperature, Test temperature (4)	[338]
Rock-salt	ε_r	XGBoost	E	94	R^2 = 0.9376 MAE = 0.5249	Sintering temperature, Atomic ratio, Cationic radius, Electronegativity (6)	[339]
$(Zr_{0.7}Sn_{0.3})TiO_4$+glass	ε_r	SVR.RBF	E	19	r = 0.7897	Composition, Calcination temperature, Sintering temperature (5)	[322]
$Mg_2Al_4(Si_{0.8}Ge_{0.2})_5O_{18}$ + TiO_2	ε_r	SVR.LIN	E	15	R^2 = 0.95	Weight fraction of TiO_2 addition, Sintering temperature (2)	[324]
Universality	ε_{ion}	RF	C	1266	R^2 = 0.73 RMSE = 0.15	Std. of the principal quantum number, Mean neighbor distance variation (45)	[345]
Universality	ε_{ion}	LightGBM	C	7113	R^2 = 0.68 RMSE = 0.26	Band gap, Max packing efficiency (116)	[342]
Oxides	ε_{ion}	SchNet	C	2527	R^2 = 0.85 RMSE = 0.14	Minimum absolute local difference in the number of unfilled electrons, Mean Neighbor Distance Variation	[346]
ABO_3-based	ε_{ion}	LightGBM	C	216	R^2 = 0.67 RMSE = 0.26	Band gap, Max packing efficiency (116)	[342]
Universality	ε_{el}	RF	C	1266	R^2 = 0.89 RMSE = 0.037	Mean atomic mass, Mass density (29)	[345]
Universality	ε_{el}	SVR.RBF	C	1364	R^2 = 0.86 RMSE = 0.99	Bandgap, Mass density, Formation energy (134)	[336]
Universality	ε_{el}	LightGBM	C	7113	R^2 = 0.83 RMSE = 0.12	Band gap, Max packing efficiency (116)	[342]
ABO_3-based	ε_{el}	GBR	C	431	R^2 = 0.89 RMSE = 0.82	Band gap, Density (42)	[343]
ABO_3-based	ε_{el}	ARORF	C	204	R^2 = 0.95 RMSE = 0.11	Radius of the B-site, Electronegativity, Bandgap (9)	[344]
ABO_3-based	ε_{el}	LightGBM	C	216	R^2 = 0.79 RMSE = 0.12	Band gap, Max packing efficiency (116)	[342]
$BaTiO_3$-based	tanδ	BP-ANN	E	21	$r = 0.9998^{***}$ RMSE = 0.0005	Concentrations of five additives (5)	[320]
$(Zr_{0.7}Sn_{0.3})TiO_4$+glass	tanδ	SVR.RBF	E	19	r = 0.8538	Composition of CuO, ZnO and glass (5)	[322]
Glass ceramics	tanδ	GKRR	E	63	R^2 = 0.91 RMSE = 0.0011	Concentrations of ceramic filler, Glass phase and processing parameters (9)	[340]
Binary and ternary insulator	tanδ (100 GHz)	MLP+TL	C	50	R^2 = 0.82	Born effective charge, Two-phonon density of states, Phonon frequency (301)	[351]
ABO_4	$Q\times f$	SVR.RBF	E	164	R^2 = 0.647 RMSE = 13320 GHz	Primitive cell volume (Vm), Molecular dielectric polarizability	[350]

						(p), Average of A- and B-site cationic electronegativity (enm) (3)	
Scheelite ABO_4	$Q\times f$	SVR.RBF	E	41	R^2 = 0.8115 RMSE = 8363 GHz	Vm, p, enm (3)	[350]
Wolframite ABO_4	$Q\times f$	SVR.RBF	E	46	R^2 = 0.6646 RMSE = 16594 GHz	Vm, p, enm, Average bond length, Theoretical density, Polarizability per unit volume (6)	[350]
$ACuSi_4O_{10}$	$Q\times f$	SVR.RBF	E	11	R^2 = 0.8589 RMSE = 4102 GHz	Bond length of A-O2, Variance in A-O bond lengths (2)	[349]
$Li_4SrCaSi_2O_8$-based	$Q\times f$	Decision Tree	E	50	R^2 = 0.89	Si/Li atomic mass ratio, Si/Sr ionic radius ratio, Total electronegativity of cations (9)	[348]
$CaTiO_3$-based	$Q\times f$	PR	E	20	RMSE = 170 GHz	Molar ratio of A and B site substitution (2)	[323]
$Mg_2Al_4(Si_{0.8}Ge_{0.2})_5O_{18}$ + TiO_2	$Q\times f$	SVR.LIN	E	15	R^2 = 0.9	Weight fraction of TiO_2 addition, Sintering temperature (2)	[324]
Five crystal systems	τ_f	SVR.RBF	E	422	R^2 = 0.79 RMSE = 22.53 ppm/K	Pauling Number, Common Neighbor Analysis, Calcination temperature (20)	[337]
Quaternary materials	τ_f	SISSO	E	725	R^2 = 0.57	Element ratio, Coordination number, Chemical potential, Mass attenuation coefficient, Polarizability, Permittivity (6)	[330]
$CaTiO_3$-based	τ_f	SVR.RBF	E	20	RMSE = 7 ppm/K	Molar ratio of A and B site substitution (2)	[323]
$BaTiO_3$-based	$\tau_{\varepsilon\,max}$	BP-ANN	E	21	r = 0.9999*** RMSE = 0.65 ppm/K	Concentrations of five additives (5)	[320]
Cordierite + TiO_2	τ_f	SVR.RBF	E	15	R^2 = 0.94	Weight fraction of TiO_2 addition, Sintering temperature (2)	[324]
ABO_3	τ_f	XGBoost	E	104	R^2 = 0.7799 RMSE = 15.75 ppm/K	Molecular dielectric polarizability, Bond-length-based tolerance factor, Ionic volume, Molecular mass (4)	[352]

* Data Source: E = Experiment; C = Calculation; C+E = Combined experiment and calculation.

3. Conclusions, Future Perspectives and Research Challenges

This review has systematically surveyed the landscape of microwave dielectric ceramics research across five interconnected dimensions: property evaluation, mechanistic understanding, innovative processing, device applications, and data-driven discovery.

Standardized resonant methods, particularly the TE_{011}-mode parallel plate and $TE_{01\delta}$-mode metal cavity techniques, have established themselves as reliable tools for evaluating low-loss materials, with measurement errors for ε_r typically below 1% and tanδ detection limits extending to 10^{-5}. Building on this, understanding of the physical origins of dielectric behavior has matured from qualitative descriptions to quantitative frameworks. The dielectric theory of crystal structure enables the decomposition of macroscopic properties into contributions from individual chemical bonds, while lattice dynamics has clarified the frequency-dependent roles of various vibration modes. A defect perspective further elucidates how multiscale imperfections, from point defects to domain structures, influence anharmonic lattice vibrations and relaxation behavior, providing critical insights into the origins of dielectric loss. More recently, the cation rattling effect has emerged as a new paradigm for understanding and tailoring the temperature coefficient τ_f. On the processing front, innovative technologies are reshaping manufacturing. The cold sintering process, for instance, achieves ceramic densification below 300 °C via dissolution-precipitation mechanisms, reducing energy consumption by over 97% compared to conventional sintering while enabling co-firing with polymers, glasses, and low-melting-point electrodes. The translation of material properties into device performance is clearly demonstrated across applications: low-ε_r ceramics serve as high-speed substrates, medium-ε_r materials form the core of resonators and filters, and high-ε_r compositions enable extreme miniaturization. Finally, machine learning is accelerating the shift from trial-and-error experimentation to rational design. While early compositional models succeeded only within narrow domains, the incorporation of physics-informed descriptors has significantly improved both predictive accuracy and interpretability.

Future research on MWDCs lies at the intersection of material innovation, sustainable manufacturing, and intelligent design. Firstly, there is an urgent need for materials with ultra-low dielectric loss (tan$\delta \leq 10^{-4}$), near-zero temperature coefficient of resonant frequency (τ_f), and low permittivity ($\varepsilon_r \leq 6$) to enable operation in the millimeter-wave (mmWave) and sub-

terahertz (sub-THz) bands, which is critical for achieving ultra-high data rates and low latency. This will necessitate the exploration of novel material systems, such as high-entropy ceramics and complex oxides, and the refinement of existing compositions through advanced doping and composite engineering. Secondly, sustainable and low-energy manufacturing will become increasingly important. Novel processing techniques, such as cold sintering (below 300 °C) and microwave-assisted sintering, etc., offer significant potential to reduce energy consumption and enable co-firing with low-melting-point metals and polymers, facilitating heterogeneous integration. Thirdly, data-driven discovery using machine learning (ML) and artificial intelligence (AI) will accelerate the design and optimization of MWDCs. The integration of machine learning and high-throughput experimentation will accelerate the discovery of new ceramic compositions, moving beyond traditional trial-and-error approaches to enable rational, on-demand material design. Finally, multifunctional integration will be a key trend, where MWDCs are designed to combine dielectric functionality with other properties like thermal conductivity or piezoelectricity, enabling the development of compact, high-performance RF modules for integrated systems.

Despite these promising directions, significant research challenges remain. A primary hurdle is achieving ultra-low loss at high frequencies (above 100 GHz). As operating frequencies increase into the mmWave and sub-THz range, dielectric and conductor losses escalate dramatically, making it difficult to maintain high $Q \times f$. This requires a deeper understanding of loss mechanisms at the atomic and microstructural levels and the development of new characterization techniques for these frequencies. Another critical challenge is manufacturing consistency and scalability. The performance of MWDCs is highly sensitive to processing conditions, and achieving uniform microstructures with minimal defects at the nanoscale remains difficult, especially for large-scale production. Additionally, while ML shows great promise, data scarcity and model interpretability are ongoing challenges. Building comprehensive, high-quality datasets and developing physically interpretable ML models that

can reliably predict properties across diverse material systems are essential for realizing the full potential of AI-driven materials discovery. Finally, integrating MWDCs with emerging device architectures poses significant technical barriers. For 6G communication and chiplet packaging applications, seamless integration with semiconductor processes such as thin-film deposition and 3D fabrication, as well as compatibility with LTCC and organic substrates, are critically required. This requires materials possessing matched thermal expansion coefficients and excellent long-term performance stability. Addressing these challenges will solidify MWDCs' role as foundational materials in next-generation wireless technologies and beyond.

Acknowledgments

This work was supported by the Key Research and Development Program of Shaanxi (No. 2025CY-YBXM-145); the National Natural Science Foundation of China (Nos. 52161145401 and 52562015); the Natural Science Foundation and the Project of Science and Technology Program of Guangxi Zhuang Autonomous Region (Nos. 2024GXNSFFA010013 and AB24010116); the Guangxi Science and Technology Major Special Project (Task No. Guike AA24263001); the "Leading Geese" Research and Development Program of the Department of Science and Technology of Zhejiang Province (No. 2023C01183); the Tsinghua University State Key Laboratory of New Ceramic Materials Project (No. 2025QHTC-ZZKYB002); the Opening Project of Guangxi Key Laboratory of Green Manufacturing for Ecological Aluminum Industry (No. GXGMEA202404), the Natural Science Foundation of Fujian Province (Nos. 2023J011802 and 2023J05301), and the Guangxi BaGui Young Scholars Funding, and Guangxi Special Appointed Experts Funding.

Author Contribution

This article is a result of group effort. Lei Li wrote section 2.1; Hongyu Yang, Chuntao Ou, and Enzhu Li wrote sections 1 and 2.2.1; Hua-ao Sun, Guangran Lin, Wanghuai Zhu, and Feng Shi wrote section 2.2.2; Weijia Guo and Zhenxing Yue wrote section 2.2.3; Ying Tang, Jie Li, Huaicheng Xiang, Weishuang Fang, Huixing Lin, Junfeng Yang, and Liang Fang wrote section

2.2.4; Muhammad Adnan Munir, and Jing Guo wrote section 2.3; Weijia Luo, Huan Liu and Kaixin Song wrote section 2.4, Jincheng Qin and Zhifu Liu wrote section 2.5; Hong Wang wrote the future perspectives and research challenges. Hongyu Yang designed the whole structure of the paper and made the final check.

Availability of Data and Materials

The data that support the findings of this study are available from the corresponding author upon reasonable request.

Declaration of Competing Interest

The authors declare that they have no known competing financial interests or personal relationships that could have appeared to influence the work reported in this paper.

References

[1] Yang Y, Fang W, Lin H, *et al.* $SrGa_{12}O_{19}$: The first low-ε_r Ga-based microwave dielectric ceramic with anomalous positive τ_f. *Journal of Advanced Ceramics* 2024, **13**: 1432–1441.

[2] Sebastian MT, Wang H, Jantunen H. Low temperature co-fired ceramics with ultra-low sintering temperature: A review. *Current Opinion in Solid State and Materials Science* 2016, **20**: 151–170.

[3] Yang J, Lei P, Song X, *et al.* Abnormal dielectric behavior of glaserite-type $Ba_{3-x}Sr_xMgSi_2O_8$ solid solution. *Journal of Advanced Ceramics* 2025, **14**: 9221020.

[4] Xu XY, Wu HT. A Review on the Microwave Dielectric Ceramics Testing Technology and Related Systems. *Advanced Ceramics* 2025, **46**: 247–285.

[5] Zhang X, Zhou L, Yang J, *et al.* Revealing loss mechanisms through interpretable machine learning and accelerated discovery of ultra-low-loss dielectric ceramics in the Li_2TiO_3–Li_3NbO_4–MgO system. *Journal of Materials Science & Technology* 2026, **267**: 268–283.

[6] Saito S, Kurokawa K. A Precision Resonance Method for Measuring Dielectric Properties of Low-Loss Solid Materials in the Microwave Region. *Proceedings of the IRE* 1956, **44**: 35–42.

[7] Wu Z, Meng Q, Zhang S. Semiempirical study on the valences of Cu and bond covalency in $Y_{1-x}Ca_xBa_2Cu_3O_{6+y}$. *Physical Review B* 1998, **58**: 958.

[8] Phillips JC, Van Vechten JA. Charge Redistribution and Piezoelectric Constants. *Physical Review Letters* 1969, **23**: 1115–1117.

[9] Shi F, Dong H-L, Zhou D, *et al.* Lattice dynamics and phonon characteristics of complex perovskite microwave ceramics. *IET Nanodielectrics* 2019, **2**: 11–26.

[10] Yang H, Zhang S, Yang H, *et al.* The latest process and challenges of microwave dielectric ceramics based on pseudo phase diagrams. *Journal of Advanced Ceramics* 2021, **10**: 885–932.

[11] Zhang S, Gu X, Zhang N, *et al.* Ultra-high Q×f and low ε_r of microwave dielectric ceramic $SrYb_2O_4$ with mitigated rattling effect and design of dielectric resonant antenna for 5 G applications. *Journal of the European Ceramic Society* 2025, **45**: 117637.

[12] Liu C, Xu M, Kang X*, et al*. Advances in Low-Temperature Co-Fired Ceramics for Next-Generation Electronics Applications. *Advanced Materials* 2026, **n/a**: e17514.
[13] Guo H, Baker A, Guo J*, et al*. Protocol for Ultralow-Temperature Ceramic Sintering: An Integration of Nanotechnology and the Cold Sintering Process. *ACS Nano* 2016, **10**: 10606–10614.
[14] Luo W, Wang S, Zheng S, *et al*. Dielectric response of ANb_2O_6 (A = Zn, Co, Mn, Ni) columbite niobates: From microwave to terahertz. *Journal of Advanced Ceramics* 2024, **13**: 1189–1197.
[15] Jin JY, Wei M, Huang YH*, et al*. Core–shell structural engineering for efficient τf regulation in low-loss MgF_2-based microwave dielectric ceramics. *Journal of Materials Science & Technology* 2026, **271**: 279–286.
[16] Sun Z, Luo T, Gao P*, et al*. Machine-Learning-Designed BCZT–SBT Heterointerface Unlocks Fatigue-Resistant Energy Storage. *Advanced Materials* 2026, **38**: e19635.
[17] He J, Wang C, Li J*, et al*. Machine learning assisted prediction of dielectric temperature spectrum of ferroelectrics. *Journal of Advanced Ceramics* 2023, **9**: 1793–1804.
[18] Chen LF, Ong CK, Neo C*, et al*. Microwave electronics: measurement and materials characterization: John Wiley & Sons 2004.
[19] Kajfez D, Guillon P. Dielectric Resonators (Second Edition). [M].Atlanta:Noble, 1999.
[20] Kajfez D. Random and systematic uncertainties of reflection-type Q-factor measurement with network analyzer. *IEEE Transactions on Microwave Theory and Techniques* 2003, **51**: 512–519.
[21] Kajfez D, Chebolu S, Abdul-Gaffoor M*, et al*. Uncertainty analysis of the transmission-type measurement of Q-factor. *IEEE Transactions on Microwave Theory and Techniques* 2002, **47**: 367–371.
[22] Kajfez D. Linear fractional curve fitting for measurement of high Q factors. *IEEE transactions on microwave theory and techniques* 2002, **42**: 1149–1153.
[23] Hakki B, Coleman PD. A dielectric resonator method of measuring inductive capacities in the millimeter range. *IRE Transactions on Microwave theory and techniques* 2003, **8**: 402–410.
[24] Courtney WE. Analysis and evaluation of a method of measuring the complex permittivity and permeability microwave insulators. *IEEE Transactions on Microwave Theory and Techniques* 2003, **18**: 476–485.
[25] Kooi P, Leong M, Satya Prakash A. Finite-element analysis of the shielded cylindrical dielectric resonator. IEE Proceedings H (Microwaves, Antennas and Propagation): IET 1985:7–16.
[26] Kajfez D. Incremental frequency rule for computing the Q-factor of a shielded TE/sub omp/dielectic resonator (short papers). *IEEE transactions on microwave theory and techniques* 2003, **32**: 941–943.
[27] Krupka J, Derzakowski K, Riddle B*, et al*. A dielectric resonator for measurements of complex permittivity of low loss dielectric materials as a function of temperature. *Measurement Science and Technology* 1998, **9**: 1751–1756.
[28] Li L, Zhu JY, Chen XM. Measurement Error of Temperature Coefficient of Resonant Frequency for Microwave Dielectric Materials by $TE_{01\delta}$-Mode Resonant Cavity Method. *IEEE Transactions on Microwave Theory and Techniques* 2016, **64**: 3781–3786.
[29] Li L, Ubic R, Chen XM. On the τ_f measurement of microwave dielectric ceramics. *Materials Research Bulletin* 2024, **178**: 112920.
[30] Yang S, Li L, Chen XM. Temperature dependence of τ_f and its origin in $MgTiO_3$–$CaTiO_3$ microwave dielectric composites. *Journal of the European Ceramic Society* 2022, **42**: 5718–5725.
[31] Shannon RD. Dielectric polarizabilities of ions in oxides and fluorides. *Journal of Applied Physics* 1993, **73**: 348–366.

[32] Phillips J. Dielectric definition of electronegativity. *Physical Review Letters* 1968, **20**: 550.
[33] Van Vechten JA. Quantum dielectric theory of electronegativity in covalent systems. I. Electronic dielectric constant. *Physical Review* 1969, **182**: 891.
[34] Van Vechten J. Quantum dielectric theory of electronegativity in covalent systems. II. Ionization potentials and interband transition energies. *Physical review* 1969, **187**: 1007.
[35] Phillips J. Ionicity of the chemical bond in crystals. *Reviews of modern physics* 1970, **42**: 317.
[36] Levine B. Bond susceptibilities and ionicities in complex crystal structures. *The Journal of Chemical Physics* 1973, **59**: 1463–1486.
[37] Phillips JC. Bonds and Bands in Semiconductors. *Science* 1970, **169**: 1035–1042.
[38] Kucharczyk W. A bond-charge calculation of the quadratic electro-optic effect in LiF. *Journal of Physics C: Solid State Physics* 1987, **20**: 1875–1880.
[39] Levine B. Bond-charge calculation of nonlinear optical susceptibilities for various crystal structures. *Physical review B* 1973, **7**: 2600.
[40] Van Vechten J, Bergstresser T. Electronic structures of semiconductor alloys. *Physical Review B* 1970, **1**: 3351.
[41] Stringfellow G. Calculation of ternary phase diagrams of III–V systems. *Journal of Physics and Chemistry of Solids* 1972, **33**: 665–677.
[42] De Alvarez CV, Walter JP, Cohen ML*, et al*. Wavelength-modulation spectra and band structures of InP and GaP. *Physical Review B* 1972, **6**: 1412.
[43] Wang J, Ren Y, Zhu X, *et al.* Novel medium-entropy $Ca_3(Co_{0.25}Zn_{0.25}Mg_{0.25}Cu_{0.25})_2SiV_2O_{12}$ microwave dielectric ceramics with high Q×f and near-zero τ_f. *Journal of Advanced Ceramics* 2025, **14**: 9221110.
[44] Li C, Du K, Zhou M, *et al.* Achieving ultra-low thermal expansion and excellent microwave dielectric properties in osumilite-type $BaMg_2Al_6Si_{9-x}Ge_xO_{30}$ ceramics. *Journal of Advanced Ceramics* 2025, **14**: 9221146.
[45] Yang H, Chai L, Liu Q*, et al.* Ionic substitution effects on the structure-property relationship of $Zn_{0.5}Ti_{0.5}NbO_4$ microwave dielectric ceramics. *Ceramics International* 2022, **48**: 25292–25301.
[46] Li Y, Hou Z, Fang Z, *et al.* Chemical bond and dielectric response of $Yb_2Si_2O_7$ ceramic with low dielectric constant at GHz and THz. *Journal of Advanced Ceramics* 2025, **14**: 9221024.
[47] Shi M, Ma S, Xia W, *et al.* Effects of oxygen vacancy on bond ionicity, lattice energy, and microwave dielectric properties of CeO_2 ceramics with Yb^{3+} substitution. *Journal of Advanced Ceramics* 2024, **13**: 247–254.
[48] Xu C, Yang H, Xing L*, et al.* Structural features of glass-free $Al_2Mo_3O_{12}$ ceramic with excellent microwave dielectric properties. *Ceramics International* 2023, **49**: 33578–33587.
[49] Harrison W, Cheetham A, Faber Jr J. The crystal structure of aluminum molybdate, $Al_2(MoO_4)_3$, determined by time-of-flight powder neutron diffraction. *Journal of Solid State Chemistry* 1988, **76**: 328–333.
[50] Zhang S, Li H, Zhou S*, et al.* Estimation thermal expansion coefficient from lattice energy for inorganic crystals. *Japanese journal of applied physics* 2006, **45**: 8801.
[51] Shao ZX, Zhang QR, Liu TY*, et al.* First-principles study on electronic structures and absorption bands of $CaWO_4$ crystals with interstitial oxygen atoms. *Physica Status Solidi (a)* 2007, **204**: 3159–3164.
[52] Xiao M, Sun H, Zhou Z*, et al.* Bond ionicity, lattice energy, bond energy, and microwave dielectric properties of $Ca_{1-x}Sr_xWO_4$ ceramics. *Ceramics International* 2018, **44**: 20686–20691.

[53] Niu H, Gou H, Ewing RC*, et al.* First principles investigation of structural, electronic, elastic and thermal properties of rare-earth-doped titanate Ln_2TiO_5. *AIP Advances* 2012, **2**: 032114.

[54] Zheng Y, Luo X, You J*, et al.* Hierarchical porous ceramics with multiple open pores from boehmite gel emulsions. *Journal of the American Ceramic Society* 2021, **104**: 1902–1907.

[55] Guo H, Chu W, Zheng Q*, et al.* Tuning the carrier lifetime in black phosphorene through family atom doping. *The Journal of Physical Chemistry Letters* 2020, **11**: 4662–4667.

[56] Koga E, Yamagishi Y, Moriwake H, *et al.* Order-disorder transition and its effect on microwave quality factor Q in $Ba(Zn_{1/3}Nb_{2/3})O_3$ system. *Journal of Electroceramics* 2006, **17**: 375–379.

[57] Li H, Fan H, Zhang J*, et al.* Sintering behavior and properties of lithium stabilized sodium β"-alumina ceramics with YSZ addition. *Ceramics International* 2019, **45**: 6744–6752.

[58] Hanuza J, Ptak M, Mączka M*, et al.* Polarized IR and Raman spectra of $Ca_2MgSi_2O_7$, $Ca_2ZnSi_2O_7$ and $Sr_2MgSi_2O_7$ single crystals: Temperature-dependent studies of commensurate to incommensurate and incommensurate to normal phase transitions. *Journal of Solid State Chemistry* 2012, **191**: 90–101.

[59] Xue J, Dong M, Li J*, et al.* Gelcasting of aluminum nitride ceramics. *Journal of the American Ceramic Society* 2010, **93**: 928–930.

[60] Liu D, Zhang S, Wu Z. Lattice energy estimation for inorganic ionic crystals. *Inorganic Chemistry* 2003, **42**: 2465–2469.

[61] Tian H, Zhang Y, Wang R*, et al.* Effect of Ge^{4+}-substituted on the structure characteristics and microwave/terahertz dielectric properties of ultra-low ε_r, high Q·f cordierite ceramics. *Journal of Materials Science & Technology* 2025, **216**: 165–177.

[62] Tian H, Zhang X, Zhang Z*, et al.* Low-permittivity $LiLn(PO_3)_4$ (Ln = La, Sm, Eu) dielectric ceramics for microwave/millimeter-wave communication. *Journal of Advanced Ceramics.* 2024, **13**: 602–620.

[63] Tian H, Liu Y, Zhang Z*, et al.* Crystal structure, bond characteristics, and microwave dielectric properties of novel low-ε_r $LiRE(PO_3)_4$ (RE = Pr, Nd) ceramics. *Ceramics International* 2025, **51**: 5249–5261.

[64] Zhang Z, Feng R, Li B. A novel microwave dielectric ceramic CaB_2O_4 with low dielectric constant. *Physica B: Condensed Matter* 2024, **695**: 416526.

[65] Li S, Li C, Mao M*, et al.* High Q×f values of Zn-Ni co-modified $LiMg_{0.9}Zn_{0.1-x}Ni_xPO_4$ microwave dielectric ceramics for 5G/6G LTCC modules. *Journal of the European Ceramic Society* 2022, **42**: 5684–5690.

[66] Huang F, Su H, Li Y*, et al.* Experimental and theoretical study on the relationship between structure and properties of NiO substituted $BaZnP_2O_7$ microwave dielectric ceramics with enhanced quality factor for LTCC application. *Materials Research Bulletin* 2024, **175**: 112766.

[67] Chen Y-B, Tang L, Su X. Q Factor Enhancement in $Nd_2Zr_3(MoO_4)_9$ Microwave Ceramics via B-Site $(Bi_{0.5}Ta_{0.5})^{4+}$ Substitution and Low-Temperature Sintering. *Journal of the European Ceramic Society* 2025: 117771.

[68] Lin MC, Ling IC, Hsu TH*, et al.* Investigation of the correlation between structure and microwave dielectric properties of ZnV_2O_6 ceramic using PVL bond theory. *Journal of the European Ceramic Society* 2024, **44**: 5016–5021.

[69] Yang H, Huang X, Zhang J*, et al.* Effect of Nd^{3+} and Sm^{3+} doping on the crystal structure and dielectric properties of $Y_{2-x}A_xMgTiO_6$ ceramics. *Journal of Advanced Ceramics* 2025, **14**: 9221082.

[70] Wu H, Kim ES. Characterization of crystal structure and microwave dielectric properties of $AZrNb_2O_8$ (A = Zn, Co, Mg, Mn) ceramics based on complex bond theory. *Ceramics International* 2016, **42**: 5785–5791.

[71] Yang H, Guo Z, Xiong Z*, et al.* Bond theory, vibrational spectroscopy, and dielectric responses of trirutile ATa_2O_6 (A = Mg, Ni) microwave ceramics. *Ceramics International* 2024, **50**: 19171–19181.

[72] Wang S, Zhang Y. Structure, bond characteristics and microwave dielectric properties of new $A_{0.75}Ti_{0.75}Ta_{1.5}O_6$ (A = Ni, Co, Zn and Mg) ceramics based on complex chemical bond theory. *Journal of the European Ceramic Society* 2020, **40**: 1181–1185.

[73] Xiao L, Deng L, Zhang Y*, et al.* Crystal Structure, Chemical Bond, and Microwave Dielectric Properties of $Ba_{1-x}Sr_x(Zn_{1/3}Nb_{2/3})O_3$ Solid Solution Ceramics. *Molecules* 2023, **28**: 3451.

[74] Wang Y, Wu P, Liu Q*, et al.* SnO_2 doping effects on the phase constitution and microwave dielectric properties of a $Co_{0.5}Ti_{0.5}NbO_4$ system. *Ceramics International* 2022, **48**: 17433–17439.

[75] Chen Y, Zhang S, Yang H*, et al.* Bond ionicity, lattice energy and structural evolution of Ta substituted $0.15ZnO–0.15Nb_2O_5–0.55TiO_2$ dielectric ceramics. *Ceramics International* 2019, **45**: 8832–8839.

[76] Zhang Y, Zhang Y, Yang M*, et al.* Ion selection criteria for effective co-doping in perovskite ceramics: A promising strategy via synergistic pinning effect. *Journal of Materials Science & Technology* 2026, **269**: 102–112.

[77] Pandey J, Ghoshal D, Dey D*, et al.* Local ferroelectric polarization in antiferroelectric chalcogenide perovskite $BaZrS_3$ thin films. *Physical Review B* 2020, **102**: 205308.

[78] Zhang H, Diao C, Liu S*, et al.* XRD and Raman study on crystal structures and dielectric properties of $Ba[Mg_{(1-x)/3}Zr_xNb_{2(1-x)/3}]O_3$ solid solutions. *Ceramics International* 2014, **40**: 2427–2434.

[79] Shi F, Dong H. Correlation of crystal structure, dielectric properties and lattice vibration spectra of $(Ba_{1-x}Sr_x)(Zn_{1/3}Nb_{2/3})O_3$ solid solutions. *Dalton Transactions* 2011, **40**: 6659–6667.

[80] Lv J, Cao Z, Wang Y*, et al.* Crystal structures and microwave dielectric properties of Sr_2MgWO_6 ceramics at different sintering temperatures. *Journal of Materiomics* 2022, **8**: 79–87.

[81] Lv J, Xiao EC, Li XH*, et al.* Crystal structures, dielectric properties, and lattice vibrational characteristics of $(1-x)CaWO_4–xTiO_2$ composite ceramics. *Ceramics International* 2020, **46**: 3715–3724.

[82] Xiao EC, Shi F, Fu G*, et al.* Effects of $BaCu(B_2O_5)$ additives on the crystal structures and dielectric properties of $CaMgGeO_4$ ceramics for LTCC applications. *Crystal Engineering Communications* 2020, **22**: 4768–4777.

[83] Xiao EC, Li J, Wang J*, et al.* Phonon characteristics and dielectric properties of $BaMoO_4$ ceramic. *Journal of Materiomics* 2018, **4**: 383–389.

[84] Wang X, Lv J, Xu Y*, et al.* Dielectric responses and structure-property relationships of $Ca_{1-x}Ba_xWO_4$ composite microwave dielectric ceramics. *Journal of Alloys and Compounds* 2022, **925**: 166669.

[85] An Z, Lv J, Wang X*, et al.* Effects of LiF additive on crystal structures, lattice vibrational characteristics and dielectric properties of $CaWO_4$ microwave dielectric ceramics for LTCC applications. *Ceramics International* 2022, **48**: 29929–29937.

[86] Xiao Ec, Cao Z, Li J*, et al.* Crystal structure, dielectric properties, and lattice vibrational characteristics of $LiNiPO_4$ ceramics sintered at different temperatures. *Journal of the American Ceramic Society* 2020, **103**: 2528–2539.

[87] Yu Y, Wang X, An Z, *et al*. Dielectric response mechanism and structure–property relationships of $SrSn(BO_3)_2$ microwave ceramics with ultra-low permittivity and their application for 5G microstrip patch antenna. *Scientific Reports* 2025, **15**: 9283.

[88] Xiang H, Kilpijärvi J, Myllymäki S, *et al*. Spinel-olivine microwave dielectric ceramics with low sintering temperature and high quality factor for 5 GHz wi-fi antennas. *Applied Materials Today* 2020, **21**: 100826.

[89] Li J, Wang J, Fu G, *et al*. Crystal structure characteristics, intrinsic properties, and vibrational spectra of non-stoichiometric $Ca_{1+x}WO_4$ ceramics. *Journal of Applied Physics* 2018, **124**.

[90] Reaney IM, Iddles D. Microwave Dielectric Ceramics for Resonators and Filters in Mobile Phone Networks. *Journal of the American Ceramic Society* 2006, **89**: 2063–2072.

[91] Sebastian M, Ubic R, Jantunen H. Low-loss dielectric ceramic materials and their properties. *International Materials Reviews* 2015, **60**: 392–412.

[92] Okaya A, Barash LF. The Dielectric Microwave Resonator. *Proceedings of the Institute of Radio Engineers* 1962, **50**: 2081–2092.

[93] Cohn SB. Microwave Bandpass Filters Containing High-Q Dielectric Resonators. *IEEE Transactions on Microwave Theory and Techniques* 1968, **16**: 218–227.

[94] Masse DJ, Pucel RA, Readey DW, *et al*. A new low-loss high-k temperature-compensated dielectric for microwave applications. *Proceedings of the IEEE* 1971, **59**: 1628–1629.

[95] Plourde JK, Linn DF, O'Bryan Jr HM, *et al*. $Ba_2Ti_9O_{20}$ as a Microwave Dielectric Resonator. *Journal of the American Ceramic Society* 1975, **58**: 418–420.

[96] Kawashima S, Nishida M, Ueda I, *et al*. $Ba(Zn_{1/3}Ta_{2/3})O_3$ Ceramics with Low Dielectric Loss at Microwave Frequencies. *Journal of the American Ceramic Society* 1983, **66**: 421–423.

[97] Chen H, Fu X, An Q, *et al*. Determining the Quality Factor of Dielectric Ceramic Mixtures with Dielectric Constants in the Microwave Frequency Range. *Scientific Reports* 2017, **7**: 14120.

[98] Cao M, Li L, Wu SY, *et al*. Dominant role of ceramic connectivity in microwave dielectric properties of porous ceramics. *Acta Materialia* 2023, **258**: 119207.

[99] Breeze JD, Perkins JM, McComb DW, *et al*. Do Grain Boundaries Affect Microwave Dielectric Loss in Oxides? *Journal of the American Ceramic Society* 2009, **92**: 671–674.

[100] Shimada T. Dielectric loss and damping constants of lattice vibrations in $Ba(Mg_{1/3}Ta_{2/3})O_3$ ceramics. *Journal of the European Ceramic Society* 2003, **23**: 2647–2651.

[101] Davies PK, Tong J, Negas T. Effect of Ordering-Induced Domain Boundaries on Low-Loss $Ba(Zn_{1/3}Ta_{2/3})O_3$–$BaZrO_3$ Perovskite Microwave Dielectrics. *Journal of the American Ceramic Society* 1997, **80**: 1727–1740.

[102] Bieringer M, Moussa SM, Noailles LD, *et al*. Cation Ordering, Domain Growth, and Zinc Loss in the Microwave Dielectric Oxide $Ba_3ZnTa_2O_{9-\delta}$. *Chemistry of Materials* 2003, **15**: 586–597.

[103] Fu MS, Liu XQ, Chen XM, *et al*. Cation Ordering and Domain Boundaries in $Ca[(Mg_{1/3}Ta_{2/3})_{1-x}Ti_x]O_3$ Microwave Dielectric Ceramics. *Journal of the American Ceramic Society* 2008, **91**: 2581–2587.

[104] Fu MS, Liu XQ, Chen XM, *et al*. Effects of Mg Substitution on Microstructures and Microwave Dielectric Properties of $Ba(Zn_{1/3}Nb_{2/3})O_3$ Perovskite Ceramics. *Journal of the American Ceramic Society* 2010, **93**: 787–795.

[105] Fu MS, Ni L, Chen XM. Abnormal variation of microwave dielectric properties in A/B site co-substituted $(Ca_{1-0.3x}La_{0.2x})[(Mg_{1/3}Ta_{2/3})_{1-x}Ti_x]O_3$ complex perovskite ceramics. *Journal of the European Ceramic Society* 2013, **33**: 813–823.

[106] Sun TL, Chen XM. Tailoring the order–disorder transition and microwave dielectric properties of $Ba[(Ni_{0.6}Zn_{0.4})_{1/3}Nb_{2/3}]O_3$ ceramics by Mg-substitution. *Materials Chemistry and Physics* 2015, **165**: 142–149.

[107] Zhang J, Zhou Y, Yue Z*, et al*. Microwave Dielectric Properties and Thermally Stimulated Depolarization Currents of $(1-x)Ba(Mg_{1/3}Nb_{2/3})O_3$–$xBaSnO_3$ Solid Solutions. *Journal of the American Ceramic Society* 2015, **98**: 3942–3947.

[108] Shi RD, Liu L, Zhu XL*, et al*. Ordered domain engineering and physical property modification of $Ba(Co_{1/3}Nb_{2/3})O_3$ complex perovskite ceramics. *Journal of the American Ceramic Society* 2022, **105**: 1159–1172.

[109] Shi RD, Liu L, Zhu XL*, et al*. Improving τ_f and thermal conductivity of $Ba(Zn_{1/3}Nb_{2/3})O_3$ microwave dielectric ceramics by ordered domain engineering. *Journal of the American Ceramic Society* 2022, **105**: 4219–4229.

[110] Guo RZ, Shi RD, Zhu XL*, et al*. Synergistic modification of properties in $Ba[(Zn_{0.8}Mg_{0.2})_{1/3}Nb_{2/3}]O_3$ ceramics through ordered domain engineering. *Journal of the American Ceramic Society* 2023, **106**: 4275–4283.

[111] Kang ZH, Guo RZ, Da Shi R*, et al*. Co-optimization of microwave dielectric properties in $Ba(Mg_{1/3}Ta_{2/3})O_3$ complex perovskite ceramics through ordered domain engineering. *Journal of the American Ceramic Society* 2023, **106**: 3471–3480.

[112] Guo RZ, Yu Chen X, Ding YH*, et al*. Effects of B′-site configurational entropy on structure and microwave dielectric characteristics in $Ba(B'_{1/3}Nb''_{2/3})O_3$ complex perovskite ceramics. *Journal of the American Ceramic Society* 2024, **107**: 6275–6284.

[113] Li H, Liu F, Chang KC*, et al*. Accelerating B-site cation ordering-disordering transition and improving dielectric properties of $Ba(Co,Zn)_{1/3}Nb_{2/3}O_3$ complex perovskite microwave ceramics by CuO doping. *Journal of the American Ceramic Society* 2024, **107**: 6152–6163.

[114] Guo W, Lu Y, Zhang C*, et al*. Crystallographic shearing effects on the broadband dielectric response of rutile TiO_{2-x} ceramics. *Journal of the American Ceramic Society* 2025, **108**: e70035.

[115] Wu FF, Sun R, Du C*, et al*. P^{5+}- Enhanced Novel Samarium Niobate Ultralow-Loss Microwave Ceramics as Dielectric Resonator for X-Band Antenna Applications. *Advanced Functional Materials* 2025, **35**: 2421225.

[116] Zhang Y, Xiang H, Wu X, *et al.* Low dielectric loss in vanadium-based zircon ceramics via high-entropy strategy. *Journal of Advanced Ceramics* 2025, **14**: 9221012.

[117] Lu Y, Guo W, Zhang C, *et al.* High-Q enstatite microwave/terahertz dielectric ceramics modulated by phase transition and lattice distortion. *Journal of Advanced Ceramics* 2025, **14**: 9221053.

[118] Li Z, Yang H, Zhong C*, et al*. Tuning lattice distortion and defect chemistry via medium-entropy strategy in $Sr_{0.5}Ba_xCa_{0.5-x}MoO_4$ microwave dielectric ceramics. *Acta Materialia* 2026, **303**: 121740.

[119] Petzelt J, Kamba S, Kozlov GV*, et al*. Dielectric properties of microwave ceramics investigated by infrared and submillimetre spectroscopy. *Ferroelectrics* 1996, **176**: 145–165.

[120] Petzelt J, Kamba S. Submillimetre and infrared response of microwave materials: extrapolation to microwave properties. *Materials Chemistry and Physics* 2003, **79**: 175–180.

[121] Braunlich P. Thermally stimulated relaxation in solids. *SPRINGER-VERLAG N. Y. INC., 1979, 331* 1979.

[122] Hino T. Thermally Stimulated Characteristics in Solid Dielectrics. *IEEE Transactions on Electrical Insulation* 1980, **EI-15**: 301–311.

[123] Liu W, Randall CA. Thermally Stimulated Relaxation in Fe-Doped $SrTiO_3$ Systems:I. Single Crystals. *Journal of the American Ceramic Society* 2008, **91**: 3245–3250.

[124] Zhang J, Yue Z, Luo Y, *et al*. Understanding the thermally stimulated relaxation and defect behavior of Ti-containing microwave dielectrics: A case study of $BaTi_4O_9$. *Materials & Design* 2017, **130**: 479–487.

[125] Guo W, Ma Z, Chen Y, *et al*. Lattice dynamics and terahertz response of microwave dielectrics: A case study of Al-doped $Ca_{0.6}Sm_{0.27}TiO_3$ ceramics. *Journal of the European Ceramic Society* 2022, **42**: 4953–4961.

[126] Guo W, Lu Y, Zhang C, *et al*. Low-temperature dielectric relaxation and microwave-terahertz dielectric response of Ca-Sm-Ti-O perovskite ceramics. *Journal of the European Ceramic Society* 2025, **45**: 117287.

[127] Guo W, Lu Y, Ma Z, *et al*. Defect-related broadband dielectric loss mechanisms of $Na_{1/2}Sm_{1/2}Ti_{1-z}(Al_{1/2}Nb_{1/2})_zO_3$ ceramics. *Acta Materialia* 2023, **255**: 119093.

[128] Liu W, Randall CA. Thermally Stimulated Relaxation in Fe-Doped $SrTiO_3$ Systems: II. Degradation of $SrTiO_3$ Dielectrics. *Journal of the American Ceramic Society* 2008, **91**: 3251–3257.

[129] Zhang J, Zhou Y, Peng B, *et al*. Microwave Dielectric Properties and Thermally Stimulated Depolarization Currents of MgF_2-Doped Diopside Ceramics. *Journal of the American Ceramic Society* 2014, **97**: 3537–3543.

[130] Zhang X, Zhang Y, Zhang J, *et al*. Microwave Dielectric Properties and Thermally Stimulated Depolarization Currents Study of $(1-x)Ba_{0.6}Sr_{0.4}La_4Ti_4O_{15}–xTiO_2$ Ceramics. *Journal of the American Ceramic Society* 2014, **97**: 3170–3176.

[131] Zhang J, Yue Z, Zhou Y, *et al*. Microwave Dielectric Properties and Thermally Stimulated Depolarization Currents of $(1-x)MgTiO_3–xCa_{0.8}Sr_{0.2}TiO_3$ Ceramics. *Journal of the American Ceramic Society* 2015, **98**: 1548–1554.

[132] Zhang J, Yue Z, Zhou Y, *et al*. Temperature-dependent dielectric properties, thermally-stimulated relaxations and defect-property correlations of TiO_2 ceramics for wireless passive temperature sensing. *Journal of the European Ceramic Society* 2016, **36**: 1923–1930.

[133] Zhang J, Luo Y, Yue Z, *et al*. Temperature stability, low loss and defect relaxation of MgO-TiO_2 microwave dielectric ceramics modified by $Ca_{0.8}Sr_{0.2}TiO_3$. *Ceramics International* 2018, **44**: 141–145.

[134] Luo Y, Guo W, Chen Y, *et al*. Thermally-stimulated defect relaxations and microwave/terahertz dielectric response of La,Al co-doped $(Ba,Sr)La_4Ti_4O_{15}$ ceramics. *Journal of the European Ceramic Society* 2021, **41**: 158–164.

[135] Ma Z, Guo W, Yue Z. Microwave dielectric properties of Al-doped $Ba_4(Sm,Nd)_{9.33}Ti_{18}O_{54}$ ceramics added with TiO_2 and sintered in oxygen. *Ceramics International* 2022, **48**: 12906–12913.

[136] Guo W, Zhang J, Luo Y, *et al*. Microwave dielectric properties and thermally stimulated depolarization of Al-doped $Ba_4(Sm,Nd)_{9.33}Ti_{18}O_{54}$ ceramics. *Journal of the American Ceramic Society* 2019, **102**: 5494–5502.

[137] Guo W, Ma Z, Luo Y, *et al*. Structure, defects, and microwave dielectric properties of Al-doped and Al/Nd co-doped $Ba_4Nd_{9.33}Ti_{18}O_{54}$ ceramics. *Journal of Advanced Ceramics* 2022, **11**: 629–640.

[138] Guo W, Yang Y, Ma Z, *et al*. Effects of Zr_{4+} and Hf_{4+} substitution on the structure and dielectric response of $Ba_4Sm_{9.33}Ti_{18}O_{54}$ ceramics. *Ceramics International* 2024, **50**: 12443–12449.

[139] Lu Y, Guo W, Zhang C, *et al*. Effects of Ge^{4+} substitution on the crystal structure and microwave/terahertz dielectric properties of diopside ceramics. *Journal of the European Ceramic Society* 2024, **44**: 5008–5015.

[140] Jiang Z, Guo W, Xie Z, *et al*. Defect analysis and microwave dielectric properties of reaction-sintered rutile $ZnO–Nb_2O_5–TiO_2$ ceramics. *Ceramics International* 2026, **52**: 10087–10094.

[141] Ding YH, Liu L, Yang ZJ, *et al.* Structure and microwave dielectric characteristics of $Hf_{1-x}Ti_xO_2$ ceramics. *Journal of the American Ceramic Society* 2022, **105**: 1127–1135.
[142] Hameed I, Li L, Liu XQ, *et al.* Ultra low loss $(Mg_{1-x}Ca_x)_2SiO_4$ dielectric ceramics (x = 0 to 0.15) for millimeter wave applications. *Journal of the American Ceramic Society* 2022, **105**: 2010–2019.
[143] Wang X, Li L, Hong WB, *et al.* Preparation and microwave dielectric properties of BPO_4 ceramics with ultra-low dielectric constant. *Journal of Materials Science: Materials in Electronics* 2021, **32**: 6660–6667.
[144] Wang H, Kamba S, Du H, *et al.* Microwave dielectric relaxation in cubic bismuth based pyrochlores containing titanium. *Journal of Applied Physics* 2006, **100**: 014105.
[145] Parida S, Rout SK, Cavalcante LS, *et al.* Structural refinement, optical and microwave dielectric properties of $BaZrO_3$. *Ceramics International* 2012, **38**: 2129–2138.
[146] Pulphol P, Vittayakorn N, Vittayakorn W, *et al.* Dielectric relaxation behavior of $BaZrO_3$ ceramics at low temperature. *Ceramics International* 2020, **46**: 24488–24494.
[147] Zurmühlen R, Petzelt J, Kamba S, *et al.* Dielectric spectroscopy of Ba $(B_{1/2}' B_{1/2}'')$ O_3 complex perovskite ceramics: Correlations between ionic parameters and microwave dielectric properties. I. Infrared reflectivity study (10^{12}–10^{14} Hz). *Journal of Applied Physics* 1995, **77**: 5341–5350.
[148] Wu FF, Zhou D, Du C, *et al.* Temperature stable $Sm(Nb_{1-x}V_x)O_4$ ($0.0 \leq x \leq 0.9$) microwave dielectric ceramics with ultra-low dielectric loss for dielectric resonator antenna applications. *Journal of Materials Chemistry C* 2021, **9**: 9962–9971.
[149] Wu FF, Zhou D, Du C, *et al.* Design and Fabrication of a C-Band Dielectric Resonator Antenna with Novel Temperature-Stable $Ce(Nb_{1-x}V_x)NbO_4$ (x = 0–0.4) Microwave Ceramics. *ACS Applied Materials & Interfaces* 2022, **14**: 48897–48906.
[150] Wu FF, Zhou D, Du C, *et al.* Design and fabrication of a satellite communication dielectric resonator antenna with novel low Loss and temperature-stabilized $(Sm_{1-x}Ca_x)(Nb_{1-x}Mo_x)O_4$ (x = 0.15–0.7) microwave ceramics. *Chemistry of Materials* 2022, **35**: 104–115.
[151] Bosman A, Havinga E. Temperature dependence of dielectric constants of cubic ionic compounds. *Physical Review* 1963, **129**: 1593.
[152] Harrop P. Temperature coefficients of capacitance of solids. *Journal of Materials Science* 1969, **4**: 370–374.
[153] Cockbain A, Harrop P. The temperature coefficient of capacitance. *Journal of Physics D: Applied Physics* 1968, **1**: 1109–1115.
[154] Xiao Y, Chen XM, Liu XQ. Microstructures and microwave dielectric characteristics of $CaRAlO_4$ (R = Nd, Sm, Y) ceramics with tetragonal K_2NiF_4 structure. *Journal of the American Ceramic Society* 2004, **87**: 2143–2146.
[155] Fan XC, Chen XM, Liu XQ. Structural dependence of microwave dielectric properties of $SrRAlO_4$ (R = Sm, Nd, La) ceramics: crystal structure refinement and infrared reflectivity study. *Chemistry of Materials* 2008, **20**: 4092–4098.
[156] Liu B, Li L, Liu XQ, *et al.* Structural evolution of $SrLaAl_{1-x}(Zn_{0.5}Ti_{0.5})_xO_4$ ceramics and effects on their microwave dielectric properties. *Journal of Materials Chemistry C* 2016, **4**: 4684–4691.
[157] Colla E, Reaney I, Setter N. Effect of structural changes in complex perovskites on the temperature coefficient of the relative permittivity. *Journal of Applied Physics* 1993, **74**: 3414–3425.
[158] Reaney IM, Enrico L. Colla ELC, Nava Setter NS. Dielectric and structural characteristics of Ba-and Sr-based complex perovskites as a function of tolerance factor. *Japanese Journal of Applied Physics* 1994, **33**: 3984.
[159] Reaney I, Wise P, Ubic R, *et al.* On the temperature coefficient of resonant frequency in microwave dielectrics. *Philosophical Magazine A* 2001, **81**: 501–510.

[160] Wise P, Reaney I, Lee W, *et al.* Structure–microwave property relations in $(Sr_xCa_{(1-x)})_{n+1}Ti_nO_{3n+1}$. *Journal of the European Ceramic Society* 2001, **21**: 1723–1726.

[161] Zhou D, Randall CA, Wang H, *et al.* Ultra-Low Firing High-k Scheelite Structures Based on $[(Li_{0.5}Bi_{0.5})_xBi_{1-x}][Mo_xV_{1-x}]O_4$ Microwave Dielectric Ceramics. *Journal of the American Ceramic Society* 2010, **93**: 2147–2150.

[162] Du K, Yin CZ, Guo YB, *et al.* Phase transition and permittivity stability against temperature of $CaSn_{1-x}Ti_xGeO_5$ ceramics. *Journal of the European Ceramic Society* 2022, **42**: 147–153.

[163] Wu FF, Zhou D, Du C, *et al.* Design of a Sub-6 GHz Dielectric Resonator Antenna with Novel Temperature-Stabilized $(Sm_{1-x}Bi_x)NbO_4$ (x = 0–0.15) Microwave Dielectric Ceramics. *ACS Applied Materials & Interfaces* 2022, **14**: 7030–7038.

[164] Cheng K, Li C, Yin C, *et al.* Effects of Sr^{2+} substitution on the crystal structure, Raman spectra, bond valence and microwave dielectric properties of $Ba_{3-x}Sr_x(VO_4)_2$ solid solutions. *Journal of the European Ceramic Society* 2019, **39**: 3738–3743.

[165] Yin C, Yin Y, Du K, *et al.* Fabrication of high-efficiency dielectric patch antennas from temperature-stable $Sr_{3-x}Ca_xV_2O_8$ microwave dielectric ceramic. *Journal of the European Ceramic Society* 2023, **43**: 1492–1499.

[166] Lee HJ, Hong KS, Kim SJ, *et al.* Dielectric Properties of MNb_2O_6 Compounds (Where M= Ca, Mn, Co, Ni, or Zn). *Materials Research Bulletin* 1997, **32**: 847–855.

[167] Bian JJ, Wu JY. Designing of Glass-Free LTCC Microwave Ceramic-$Ca_{1-x}(Li_{0.5}Nd_{0.5})_xWO_4$ by Crystal Chemistry. *Journal of the American Ceramic Society* 2012, **95**: 318–323.

[168] Kim ES, Choi W. Effect of phase transition on the microwave dielectric properties of $BiNbO_4$. *Journal of the European Ceramic Society* 2006, **26**: 1761–1766.

[169] Jo HJ, Kim JS, Kim ES. Microwave dielectric properties of $MgTiO_3$-based ceramics. *Ceramics International* 2015, **41**: S530–S536.

[170] Chen J, Fang W, Ao L, *et al.* Structure and chemical bond characteristics of two low-εr microwave dielectric ceramics $LiBO_2$ (B = Ga, In) with opposite τ_f. *Journal of the European Ceramic Society* 2021, **41**: 3452–3458.

[171] Zhang J, Li J, Sun Y, *et al.* Densification, microwave dielectric properties and rattling effect of $LiYbO_2$ ceramics with low ε_r and anomalous positive τ_f. *Journal of the European Ceramic Society* 2022, **42**: 7455–7460.

[172] Choi JW, Van Dover R. Correlation between temperature coefficient of resonant frequency and tetragonality ratio. *Journal of the American Ceramic Society* 2006, **89**: 1144–1146.

[173] Liao Q, Li L, Ren X, *et al.* New Low-Loss Microwave Dielectric Material $ZnTiNbTaO_8$. *Journal of the American Ceramic Society* 2011, **94**: 3237–3240.

[174] Ramarao S, Murthy V. Crystal structure refinement and microwave dielectric properties of new low dielectric loss $AZrNb_2O_8$ (A: Mn, Zn, Mg and Co) ceramics. *Scripta Materialia* 2013, **69**: 274–277.

[175] Xia WS, Li LX, Ning PF, *et al.* Relationship between bond ionicity, lattice energy, and microwave dielectric properties of $Zn(Ta_{1-x}Nb_x)_2O_6$ ceramics. *Journal of the American Ceramic Society* 2012, **95**: 2587–2592.

[176] Xiaomeng M, Xu Z, Huanrong T, *et al.* Effect of $(Zn_{1/3}Nb_{2/3})^{4+}$ co-substitution on the microwave dielectric properties of $Ce_2Zr_3(MoO_4)_9$ ceramics. *Ceramics International* 2022, **48**: 7441–7447.

[177] Li H, Chen X, Xiang Q, *et al.* Structure, bond characteristics and Raman spectra of $CaMg_{1-x}Mn_xSi_2O_6$ microwave dielectric ceramics. *Ceramics International* 2019, **45**: 14160–14166.

[178] Paschoal C, Moreira R, Surendran K, *et al*. Infrared reflectivity and intrinsic dielectric behavior of $RETiTaO_6$ (RE = Y, Ce, Pr, Nd, Sm, Eu, Gd, Tb, Dy, Ho, Er, and Yb) microwave ceramics. *Journal of Materials Research* 2005, **20**: 1164–1171.

[179] Tang Y, Zhang Z, Li J, *et al*. $A_3Y_2Ge_3O_{12}$ (A = Ca, Mg): two novel microwave dielectric ceramics with contrasting τ_f and Q×f. *Journal of the European Ceramic Society* 2020, **40**: 3989–3995.

[180] Dunitz J, Orgel L. Stereochemistry of ionic solids. *Advances in Inorganic Chemistry and Radiochemistry* 1960, **2**: 1–60.

[181] Park HS, Yoon KH, Kim ES. Effect of bond valence on microwave dielectric properties of complex perovskite ceramics. *Materials Chemistry and Physics* 2003, **79**: 181–183.

[182] Ying T, Jie L, Huaicheng X, *et al*. Rattling Effect: A New Mechanism Affecting the Resonant Frequency Temperature Coefficient of Microwave Dielectric Ceramics. *Journal of Inorganic Materials* 2025, **40**: 656–666.

[183] Ying T, Huaicheng X, Jie L. Rattling Effect in A Site and Microwave Dielectric Properties of $Ca_{(3-x)}Mg_xYb_2Ge_3O_{12}(0 \leq x \leq 3)$ Garnets. *Journal of the chinese ceramic society* 2023, **51**: 872–811.

[184] Sun Y, Xiang H, Tang Y, *et al*. Constructing the cationic rattling effect to realize the adjustability of the temperature coefficient in $Nd_{2-x}Sm_xO_3$ microwave dielectric ceramics. *Journal of the European Ceramic Society* 2024, **44**: 2859–2865.

[185] Tang Y, Li H, Li J, *et al*. Relationship between Rattling Mg^{2+} ions and anomalous microwave dielectric behavior in $Ca_{3-x}Mg_{1+x}LiV_3O_{12}$ ceramics with garnet structure. *Journal of the European Ceramic Society* 2021, **41**: 7697–7702.

[186] Yang Y, Zhai Y, Xiang H, *et al*. Rattling effects on microwave dielectric properties of $Ca_3TiBGe_3O_{12}$ (B = Mg, Zn) garnets. *Journal of the European Ceramic Society* 2022, **42**: 4566–4572.

[187] Yang Y, Tang Y, Li J, *et al*. Effects of ionic coordination bonding on microwave dielectric properties of $Y_2CaBGa_4O_{12}$ (B = Zr, Sn) garnets. *ACS Applied Electronic Materials* 2022, **4**: 3512–3519.

[188] Gu X, Tang Y, Chen J, *et al*. Tuning microwave dielectric properties of low-temperature sintered $Ca_{1-x}(Li_{0.5}Eu_{0.5})_xMoO_4$ ($0.1 \leq x \leq 0.5$) ceramics by the strong rattling effect of Li^+. *Journal of the European Ceramic Society* 2025, **45**: 117149.

[189] Xu L, Fang W, Tang Y, *et al*. Crystal structure evolution, bond characteristics and tunable microwave dielectric properties of $(Ce_{1-x}Ca_x)(Nb_{1-x}W_x)O_4$ ceramics. *Journal of the European Ceramic Society* 2024, **44**: 4657–4665.

[190] Wang S, Fang W, Wu D, *et al*. Two K20 microwave dielectric ceramics $SrLnAlO_4$ (Ln = Eu, Gd) with near-zero τ_f and contrasting Q×f. *Journal of the European Ceramic Society* 2024, **44**: 6470–6476.

[191] Li F, Tang Y, Li J, *et al*. Effect of A-site cation on crystal structure and microwave dielectric properties of AGe_4O_9 (A = Ba, Sr) ceramics. *Journal of the European Ceramic Society* 2021, **41**: 4153–4159.

[192] Zhang S, Gu X, Zhang N, *et al*. Ultra-high Q×f and low ε_r of microwave dielectric ceramic $SrYb_2O_4$ with mitigated rattling effect and design of dielectric resonant antenna for 5 G applications. *Journal of the European Ceramic Society* 2025, **45**: 117637.

[193] Sun Y, Wu J, Tang Y, *et al*. Effects of ion polarizability and oxygen vacancy on microwave dielectric properties of fluorite-structured $Ce_{1-x}Ca_xO_{2-x}$. *Journal of the American Ceramic Society* 2024, **107**: 1148–1158.

[194] Jia YQ, Luo WK, Li L, *et al*. MSO_4 (M= Ca, Sr, Ba) microwave dielectric ceramics with low dielectric constant. *Journal of the American Ceramic Society* 2023, **106**: 1250–1259.

[195] Wang X, Zhu XL, Li L, *et al*. Structure evolution and adjustment of τ_f in (Ba, Sr) HfO_3 and (Sr, Ca) HfO_3 microwave dielectric ceramics. *Journal of the American Ceramic Society* 2024, **107**: 285–299.

[196] Jiang Y, Wu G, Mao M*, et al*. Deeper insights into dodecahedron distortion and microwave dielectric properties of $Y_{3-x}R_xAl_{(Oct)2}Al_{(Tet)3-x}Si_xO_{12}$ (x = 0.1–0.5; R = Mg, Ca) garnet-type ceramics. *Ceramics International* 2023, **49**: 23334–23339.

[197] Liu D, Shao G, Tai X, *et al.* Field assisted sintering: Overview of thermo–electro–mechanical coupling effects, *Journal of Advanced Ceramics* 2026, **15**: 9221276.

[198] Evangeline T G, Annamalai A R. Densification of ceramics and ceramic-based composites using ultralow temperature sintering (cold sintering): A comprehensive review. *International Journal of Applied Ceramic Technology* 2025, **22**: e14996.

[199] Guo J, Guo H, Baker AL*, et al*. Cold sintering: a paradigm shift for processing and integration of ceramics. *Angewandte Chemie* 2016, **128**: 11629–11633.

[200] Guo H, Baker A, Guo J*, et al*. Cold sintering process: a novel technique for low-temperature ceramic processing of ferroelectrics. *Journal of the American Ceramic Society* 2016, **99**: 3489–3507.

[201] Grasso S, Biesuz M, Zoli L*, et al*. A review of cold sintering processes. *Advances in Applied Ceramics* 2020, **119**: 115–143.

[202] Ding J, Guo J, Yan R, *et al*. Cold sintering process: A green route to fabricate thermoelectrics, *Journal of Advanced Ceramics* 2024, **13**: 1697–1712.

[203] Mamaghani KR, Parvin N. Cold sintering for quantum ceramics: A low-temperature route to topological and spin–orbit-coupled materials. *Journal of Alloys and Compounds Communications* 2025: 100118.

[204] Yu T, Cheng J, Li L*, et al*. Current understanding and applications of the cold sintering process. *Frontiers of Chemical Science and Engineering* 2019, **13**: 654–664.

[205] Rao X, Yang X, Sun R, et al. Strong ferroelectric and luminescence properties of 0–3 type $0.8BaTiO_3$–$0.2CaTiO_3$: Pr^{3+} composite ceramics prepared by cold sintering process, *Journal of Advanced Ceramics* 2024, **13**: 1002−1010.

[206] Guo J, Baker AL, Guo H*, et al*. Cold sintering process: a new era for ceramic packaging and microwave device development. *Journal of the American Ceramic Society* 2017, **100**: 669–677.

[207] Wang D, Li L, Jiang J*, et al*. Cold sintering of microwave dielectric ceramics and devices. *Journal of Materials Research* 2021, **36**: 333–349.

[208] Wang D, Zhang S, Wang G*, et al*. Cold sintered $CaTiO_3$–K_2MoO_4 microwave dielectric ceramics for integrated microstrip patch antennas. *Applied Materials Today* 2020, **18**: 100519.

[209] Liu B, Li L, Song KX*, et al*. Enhancement of densification and microwave dielectric properties in LiF ceramics via a cold sintering and post-annealing process. *Journal of the European Ceramic Society* 2021, **41**: 1726–1729.

[210] Li L, Hong WB, Yang S*, et al*. Effects of water content during cold sintering process of NaCl ceramics. *Journal of Alloys and Compounds* 2019, **787**: 352–357.

[211] Zhao E, Hao J, Xue X*, et al*. Rutile TiO_2 microwave dielectric ceramics prepared via cold sintering assisted two step sintering. *Journal of the European Ceramic Society* 2021, **41**: 3459–3465.

[212] Li X, Li L, Si M, *et al.* Cold sintered $BaTiO_3$-Poly(ether imide) (PEI) nanocomposites with superior comprehensive performances. *Journal of Advanced Ceramics* 2024, **13**: 1453–1460.

[213] Bouville F, Studart AR. Geologically-inspired strong bulk ceramics made with water at room temperature. *Nature Communications* 2017, **8**: 14655.

[214] Guo J, Berbano SS, Guo H*, et al*. Cold sintering process of composites: bridging the processing temperature gap of ceramic and polymer materials. *Advanced Functional Materials* 2016, **26**: 7115–7121.

[215] Palneedi H, Sharief P, Hong SM, *et al*. Densification and grain growth in ceramics fabricated by cold sintering: A review on the effect of process parameters. *Journal of the American Ceramic Society* 2026, **109**: e70268.
[216] Tang L, Huang Z, Deng M, *et al*. Densification of water-insoluble Li_2TiO_3 nanoceramics via a cold sintering process using water as a transient liquid phase. *Journal of Advanced Ceramics* 2025, **14**: 9221133.
[217] Guo J, Floyd R, Lowum S, *et al*. Cold sintering: progress, challenges, and future opportunities. *Annual Review of Materials Research* 2019, **49**: 275–295.
[218] Hassan M, Venkatesan S, Ryu HJ. Non-volatile immobilization of iodine by the cold-sintering of iodosodalite. *Journal of Hazardous Materials* 2020, **386**: 121646.
[219] Bang S, Sengul M, Fan Z, *et al*. Morphological and chemical evolution of transient interfaces during zinc oxide cold sintering process. *Materials Today Chemistry* 2022, **24**: 100925.
[220] Biesuz M, Taveri G, Duff AI, *et al*. A theoretical analysis of cold sintering. *Advances in Applied Ceramics* 2020, **119**: 75–89.
[221] Kang X, Floyd R, Lowum S, *et al*. Mechanism studies of hydrothermal cold sintering of zinc oxide at near room temperature. *Journal of the American Ceramic Society* 2019, **102**: 4459–4469.
[222] Hong WB, Li L, Cao M, *et al*. Plastic deformation and effects of water in room-temperature cold sintering of NaCl microwave dielectric ceramics. *Journal of the American Ceramic Society* 2018, **101**: 4038–4043.
[223] Sengul MY, Guo J, Randall CA, *et al*. Water-mediated surface diffusion mechanism enables the cold sintering process: a combined computational and experimental study. *Angewandte Chemie* 2019, **131**: 12550–12554.
[224] Biesuz M, Grasso S, Sglavo VM. What's new in ceramics sintering? A short report on the latest trends and future prospects. *Current Opinion in Solid State and Materials Science* 2020, **24**: 100868.
[225] Ndayishimiye A, Sengul MY, Sada T, *et al*. Roadmap for densification in cold sintering: Chemical pathways. *Open Ceramics* 2020, **2**: 100019.
[226] Galotta A, Sglavo VM. The cold sintering process: A review on processing features, densification mechanisms and perspectives. *Journal of the European Ceramic Society* 2021, **41**: 1–17.
[227] Kähäri H, Teirikangas M, Juuti J, *et al*. Dielectric properties of lithium molybdate ceramic fabricated at room temperature. *Journal of the American Ceramic Society* 2014, **97**: 3378–3379.
[228] Hao J, Guo J, Ma C, *et al*. Cold sintering of Na_2WO_4 ceramics using a Na_2WO_4–$2H_2O$ chemistry. *Journal of the European Ceramic Society* 2021, **41**: 6029–6034.
[229] Hao J, Guo J, Zhao E, *et al*. Grain size effect on microwave dielectric properties of Na_2WO_4 ceramics prepared by cold sintering process. *Ceramics International* 2020, **46**: 27193–27198.
[230] Podonak MK, Paydar MH, Forghani M, *et al*. B_2O_3 as an effective additive for cold sintering of $MgTiO_3$. *Journal of the European Ceramic Society* 2024, **44**: 261–269.
[231] Liu Y, Liu P, Hu C. Low-temperature preparation and microwave dielectric properties of cold sintered $Li_2Mg_3TiO_6$ nanocrystalline ceramics. *Ceramics International* 2018, **44**: 21047–21052.
[232] Santha N, Rakhi M, Subodh G. Fabrication of high quality factor cold sintered $MgTiO_3$–NaCl microwave ceramic composites. *Materials Chemistry and Physics* 2020, **255**: 123636.
[233] Zhou MF, Zheng YX, Sha K, *et al*. A novel strategy to assemble core–shell-structured LiF–$CaTiO_3$ microwave dielectric ceramics via cold sintering and post-annealing

treatment. *Journal of Materials Science: Materials in Electronics* 2021, **32**: 28447–28453.

[234] Liu J, Liu B, Song KX. Enhanced microwave dielectric properties of Al_2O_3 ceramics via a cold sintering assisted two-step sintering route. *Journal of Materials Science: Materials in Electronics* 2024, **35**: 764.

[235] Pang LX, Zhou D, Li WB*, et al.* High quality microwave dielectric ceramic sintered at extreme-low temperature below 200° and co-firing with base metal. *Journal of the European Ceramic Society* 2017, **37**: 3073–3077.

[236] Abbas Q, Mirzaeian M, Hunt MR*, et al.* Current state and future prospects for electrochemical energy storage and conversion systems. *Energies* 2020, **13**: 5847.

[237] Zeng Z, Cheng J, Xu X*, et al.* Room-temperature densified Al_2O_3–H_3BO_3 ceramics with excellent microwave dielectric properties and thermal conductivity for chip packaging. *Journal of Materiomics* 2025, **11**: 101069.

[238] Hong WB, Li L, Yan H*, et al.* Cold sintering and microwave dielectric properties of dense HBO_2-II ceramics. *Journal of the American Ceramic Society* 2019, **102**: 5934–5940.

[239] Li C, Liu Y, Chi M*, et al.* ULTCC post-annealing cold sintering densification process, microwave dielectric properties of $Zn_3B_2O_6$ ceramics. *Materials Today Communications* 2022, **33**: 104997.

[240] Chi M, Liu Y, Zhou T*, et al.* Ni doping improving magnesium borate microwave dielectric ceramic for LTCC via cold sintering and post-annealing process. *Journal of Materials Science: Materials in Electronics* 2023, **34**: 235.

[241] Jia YQ, Hong WB, Li L*, et al.* Dense LiF microwave dielectric ceramics with near-zero linear shrinkage during sintering. *Ceramics International* 2022, **48**: 28463–28470.

[242] Cheng J, Wang H, Xu X*, et al.* Negative thermal expansion ScF_3 ceramic for electronic packaging applications. *Journal of Materiomics* 2025: 101126.

[243] Mena-Garcia J, Ndayishimiye A, Fan Z*, et al.* Sodium molybdate-hexagonal boron nitride composites enabled by cold sintering for microwave dielectric substrates. *Journal of the American Ceramic Society* 2023, **106**: 5975–5985.

[244] Ma M, Song K, Ji Y*, et al.* 5G microstrip patch antenna and microwave dielectric properties of cold sintered $LiWVO_6$–K_2MoO_4 composite ceramics. *Ceramics International* 2021, **47**: 19241–19246.

[245] Li Y, Zheng M, Zang M*, et al.* Cold sintering co-firing of (Ca, Bi)(Mo, V) O_4–PTFE composites in a single step. *Journal of the American Ceramic Society* 2022, **105**: 6262–6270.

[246] Wang D, Zhou D, Zhang S*, et al.* Cold-sintered temperature stable $Na_{0.5}Bi_{0.5}MoO_4$–Li_2MoO_4 microwave composite ceramics. *ACS Sustainable Chemistry & Engineering* 2018, **6**: 2438–2444.

[247] Ji Y, Song K, Zhang S*, et al.* Cold sintered, temperature-stable $CaSnSiO_5$–K_2MoO_4 composite microwave ceramics and its prototype microstrip patch antenna. *Journal of the European Ceramic Society* 2021, **41**: 424–429.

[248] Madhuri R, Rajan A, Ganesanpotti S. Cold-sintered $NaCa_2Mg_2V_3O_{12}$–Li_2MoO_4 microwave dielectrics for the design and fabrication of high-bandwidth antennas. *Materials Research Bulletin* 2023, **158**: 112069.

[249] Kähäri H, Teirikangas M, Juuti J*, et al.* Room-temperature fabrication of microwave dielectric Li_2MoO_4–TiO_2 composite ceramics. *Ceramics International* 2016, **42**: 11442–11446.

[250] Sibi N, Rajan A, Subodh G. Garnet mineral based composites through cold sintering process: microstructure and dielectric properties. *Journal of the European Ceramic Society* 2020, **40**: 371–375.

[251] Li X, Fu C, Xu W, *et al*. Hybrid low-temperature sintering processes of electro-ceramics. *Journal of the American Ceramic Society* 2024, **107**: 1996–2009.
[252] Li X, Liu W, Li L, *et al*. Energy efficient sintering of high-performance ceramics. *Journal of Advanced Ceramics* 2025, **14**: 9221186.
[253] Liang J, Zhao X, Kang S, *et al*. Microstructural evolution of ZnO via hybrid cold sintering/spark plasma sintering. *Journal of the European Ceramic Society* 2022, **42**: 5738–5746.
[254] Pozar DM. Microwave engineering: John Wiley & Sons 2011.
[255] Liu Y, He G, Zhang W, et al. Low loss and temperature-stable $Y_3MgAl_3GeO_{12}$ microwave dielectric ceramics for X-band applications. *Journal of Advanced Ceramics* 2025, **14**: 9221136.
[256] Liu C, Xu M, Kang X, *et al*. Advances in Low-Temperature Co-Fired Ceramics for Next-Generation Electronics Applications. *Advanced Materials* 2026: e17514.
[257] Xiang H, Zhou Y, Chen J, *et al*. Regulation of the temperature stability in ordered olivine microwave dielectric ceramics with low loss for dielectric resonant antenna. *Journal of Advanced Ceramics* 2025, **14**: 9221149.
[258] Zhou D, Pang LX, Wang DW, *et al*. High permittivity and low loss microwave dielectrics suitable for 5G resonators and low temperature co-fired ceramic architecture. *Journal of Materials Chemistry C* 2017, **5**: 10094–10098.
[259] Balanis CA. Antenna theory: analysis and design: John Wiley & Sons 2016.
[260] Liu H, Jiang Y, Yu X, *et al*. Dodecahedron lattice of rattling phenomenon, and microwave dielectric properties of yttrium aluminum garnet ceramics and its application verification for Wifi6E/7 patch and 6G resonant antennas. *Journal of the European Ceramic Society* 2024, **44**: 3895–3902.
[261] Wang Z, Guo H, Wei H, *et al*. Near-Zero TCF and High Quality Factor Achieved in $Li_2Ti_{1-x}(Fe_{1/2}Nb_{1/2})_xO_3$-Based Microwave Dielectric Ceramics via Phase Modulation Engineering. *ACS Applied Materials & Interfaces* 2026, **18**: 1931–1941.
[262] Xu X, Zhou X, Wu H, *et al*. Bonding characteristics, electrical and microwave/terahertz dielectric properties of novel tetragonal scheelite structure $NaSrLnMo_3O_2$ (Ln = Ce, Pr, Eu, Y, Yb) ceramics for antenna application. *Journal of Advanced Ceramics* 2025, **14**: 9221179.
[263] Ma Y, Zhang W, Liu Y, *et al*. Sintering behavior, crystal structure and dielectric properties of novel low permittivity $Na_5Sm(WO_4)_4$ ceramics for antenna design. *Journal of Alloys and Compounds* 2025: 182660.
[264] Feng Z, Wang R, Wu H, *et al*. Crystal structure, chemical bond characteristics, lattice vibrations, and microwave dielectric properties of Cu-modified tri-magnesium phosphate ceramics for antenna applications. *Journal of Alloys and Compounds* 2025, **1036**: 182038.
[265] Wang R, Liu D, Xu K, *et al*. Ultra-low εr and low dielectric loss $(Mg_{1-x}Mn_x)_2Al_4Si_5O_{18}$ (x = 0.1–0.5) microwave dielectric ceramics for patch antenna and dielectric resonator antenna applications. *Ceramics International* 2025, **51**: 40171–40183.
[266] Sun C, Zhang X, Zhou X, *et al*. Low permittivity $LiGd(PO_3)_4$ microwave dielectric ceramics and their application in C-band. *Journal of Alloys and Compounds* 2025, **1033**: 181163.
[267] Zhang Z, Li W, Zhu W, *et al*. Structure and dielectric temperature properties of CeO_2 doped $Li_2ZnTi_3O_8$ microwave ceramics and their application in 5G microstrip patch antennas. *Ceramics International* 2025, **51**: 42599–42608.
[268] Shehbaz M, Du C, Niaz MW, *et al*. All Ceramic Wideband Dielectric Patch Antenna Using Temperature-Stable High-Permittivity $Ba_{4.5}(Sm_{0.8}La_{0.2})_9Ti_{18}O_{54}$ Microwave Dielectric Ceramic for 5G Applications. *Advanced Engineering Materials* 2025, **27**: 2402519.

[269] Zhang X, Du W, Xu X, *et al.* Microwave dielectric properties of $LiCe(PO_3)_4$ metaphosphate ceramics and their application for 5G microstrip patch antenna. *Ceramics International* 2025, **51**: 17503–17513.

[270] Lou W, Song K, Hussain F, *et al.* Microwave dielectric properties of $Mg_{1.8}R_{0.2}Al_4Si_5O_{18}$ (R = Mg, Ca, Sr, Ba, Mn, Co, Ni, Cu, Zn) cordierite ceramics and their application for 5G microstrip patch antenna. *Journal of the European Ceramic Society* 2022, **42**: 2254–2260.

[271] Yin C, Du K, Zou Z, *et al.* Design and fabrication of a C-band patch antenna using novel low permittivity $SrGa_2Si_2O_8$ microwave dielectric ceramic. *Journal of the European Ceramic Society* 2023, **43**: 6091–6097.

[272] Liu Z, Du K, Li C, *et al.* Design and fabrication of a C-band patch antenna with low loss $BaM_4Si_5O_{17}$ microwave dielectric ceramics. *ACS Applied Materials & Interfaces* 2024, **16**: 57325–57333.

[273] Wu Y, Zhang W, Chen W, *et al.* Dielectric properties of temperature-stable Li_2O–Al_2O_3–B_2O_3–$CaTiO_3$ glass-ceramic composite for LTCC application. *Journal of Materials Research and Technology* 2025, **36**: 653–660.

[274] Wang W, Bao J, Wang C, *et al.* $LiMSiO_4$ (M = Ga, Sc and Y): Low-permittivity and high thermal conductivity microwave dielectric ceramics for millimeter-wave communications. *Journal of Materials Science & Technology* 2025, **225**: 288–296.

[275] Wang Z, Liu L, Du Q, *et al.* Enhanced microwave dielectric properties of CeO_2–TiO_2 ceramics by adding Al_2O_3 for microstrip antenna application. *Ceramics International* 2022, **48**: 14378–14385.

[276] Shi MA, Xia WS, Ma SY, *et al.* Crystal structure, chemical bonding properties, microwave dielectric properties and microstrip patch antenna applications of molybdates ceramics with Mo-site substitution. *Ceramics International* 2025, **51**: 24722–24730.

[277] Xu X, Jiang L, Zhang Y, *et al.* Structure characteristics, electrical and microwave dielectric properties of quaternary-phase Na_2O–Fe_2O_3–MoO_3 ceramic and fabrication of patch antenna for a sub-6 GHz 5G band. *Journal of Alloys and Compounds* 2025, **1014**: 178828.

[278] Hou H, Zhang A, Yang H, *et al.* $LiGaSiO_4$: An ultra-low permittivity dielectric material enabling application in patch antenna. *Ceramics International* 2024, **50**: 7758–7766.

[279] Xu X, Du W, Du J, *et al.* Low sintering temperature, interface characteristic and microwave/terahertz dielectric properties of ternary-phase Nd_2O_3–P_2O_5 based ceramics for patch antenna application. *Surfaces and Interfaces* 2024, **54**: 105201.

[280] Zhu W, Wang X, Liu F, *et al.* Phonon characteristics, dielectric respond mechanism, structure-property relationships of $(1-x)SrSn(BO_3)_2$-$xTiO_2$ microwave dielectric ceramics with low permittivity and their application for 5G microstrip patch antenna. *Ceramics International* 2025, **51**: 44901–44910.

[281] Xiong S, Zhu G, Zhu X, *et al.* Microstrip dielectric patch antenna fabrication and characterization using ultra low permittivity and low temperature Co-fired $LiAlSiO_4$ ceramics. *Journal of the European Ceramic Society* 2025, **45**: 116930.

[282] Zhou MF, Liu B, Hu CC, *et al.* Ultra-low permittivity MgF_2 ceramics with high Qf values and their role as microstrip patch antenna substrates. *Ceramics International* 2023, **49**: 369–374.

[283] Lin FL, Liu B, Song KX. $NaLaMgWO_6$ microwave dielectric ceramics and their sub-6 GHz band microstrip patch antenna applications. *Journal of Materials Science: Materials in Electronics* 2022, **33**: 21737–21745.

[284] Liu L, Zhang X, Zhang Y, *et al.* Low sintering temperature and microwave dielectric properties of H_3BO_3-added $Li_2Ti_{0.85}(A_{1/3}Ta_{2/3})_{0.15}O_3$ (A = Zn, Mg) ceramics for patch antenna application. *Ceramics International* 2023, **49**: 38614–38622.

[285] Yang H, Liu Q, Wang Z*, et al*. High-frequency and intrinsic dielectric properties of β-$CaSiO_3$ and its application: the microstrip patch antenna. *Journal of the American Ceramic Society* 2024, **107**: 3209–3218.

[286] Rahman MA, Islam MT, Singh MJ*, et al*. Magnetic, dielectric and structural properties of $Co_xZn_{(0.90-x)}Al_{0.10}Fe_2O_4$ synthesized by sol–gel method with application as flexible microwave substrates for microstrip patch antenna. *Journal of Materials Research and Technology* 2022, **16**: 934–943.

[287] Mali D, Rajaram N, Vehale R*, et al*. Preparation of phase-pure $MgTiO_3$ microwave dielectric ceramics for GPS antenna application. *Journal of Materials Chemistry C* 2024, **12**: 15101–15111.

[288] Xu X, Zhang Y, Du W*, et al*. The crystal structure and electric and microwave dielectric properties of novel scheelite structure $NaEr(MoO_4)_2$ ceramics and its application in the S-band. *Journal of Materials Chemistry C* 2024, **12**: 18021–18035.

[289] RM. G. Sintering: From Empirical Observations to SicentificPrinciples. *Amsterdam (the Netherlands): Elsevier,* 2022.

[290] Song XQ, Zeng FF, Yang JQ*, et al*. Crystal structure and microwave dielectric properties of garnet-type $Ca_2YZr_{2-x}Ti_xAl_3O_{12}$ ceramics for dual-band bandpass filters. *Journal of the European Ceramic Society* 2022, **42**: 4962–4968.

[291] Jiang T, Wang Z, Yu Z*, et al*. Research on rare earth-doped $Zn_{1.8}SiO_{3.8}$ microwave dielectric ceramics and their applications in filters. *ACS Applied Electronic Materials* 2025, **7**: 3333–3342.

[292] Yang J, Xie Q, Ao L*, et al*. Structure and microwave dielectric properties of novel walstromite-type $MCa_2Si_3O_9$ (M = Ba, Sr) ceramics. *Ceramics International* 2023, **49**: 27147–27153.

[293] Wen W, Jiang T, Wang J*, et al*. Enhanced microwave dielectric properties and 5G filter design of rare-earth-doped $Zn_{1.8}SiO_{3.8}$ ceramics. *Ceramics International* 2025, **51**: 37337–37347.

[294] Xiong S, Chen YB, Tang R*, et al*. ZnO-doped $MnMoO_4$ ceramics with modulated structure and enhanced microwave dielectric properties for λ/2 microstrip bandpass filters. *Ceramics International* 2025, **51**: 55725–55736.

[295] He G, Du C, Wang Z*, et al*. $BaSc_2O_4$: A Novel AB_2O_4-Type Low-k Microwave Dielectric Ceramic With Giant Positive τ_f for 5G/6G Frequency Compensation. *Advanced Functional Materials* 2026: e28138.

[296] Cameron RJ, Kudsia CM, Mansour RR. Microwave filters for communication systems: fundamentals, design, and applications: John Wiley & Sons 2018.

[297] Cassivi Y, Perregrini L, Arcioni P*, et al*. Dispersion characteristics of substrate integrated rectangular waveguide. *IEEE Microwave and Wireless Components Letters* 2002, **12**: 333–335.

[298] Lee B, Lee G, Nam S*, et al*. Extremely Low-Complexity Negative Coupling Structure for SIW Filters and Approach to Adjust Rejection Next to Transmission Zeros. *IEEE Transactions on Microwave Theory and Techniques* 2025, **73**: 5238–5247.

[299] Zakharov AV, Litvintsev SM. Lumped-distributed resonators providing multiple transmission zeros in bandpass filters with simple and mixed couplings. *IEEE Transactions on Circuits and Systems I: Regular Papers* 2024, **71**: 3502–3513.

[300] Moscato S, Cannone G, Oldoni M*, et al*. Ku/Ka band diplexer based on thin-film technology for small ground-segment user terminals. *International Journal of Microwave and Wireless Technologies* 2022, **14**: 345–350.

[301] Behera R, Sangam K, Lonkadi SS*, et al*. Realization of Lange Coupler using Hybrid Technology and its Characterization. 2022 Trends in Electrical, Electronics, Computer Engineering Conference (TEECCON): IEEE 2022:135–141.

[302] Wang D, Polat E, Schuster C, *et al.* Fast and miniaturized phase shifter with excellent figure of merit based on liquid crystal and nanowire-filled membrane technologies. *IEEE Journal of Microwaves* 2021, **2**: 174–184.

[303] Masin B, Ashok K, Joseph M, *et al.* $(Ca_{1-x}M_x)V_2O_6$ (M = Zn, Ba) ultra-low temperature co-firable ceramics for microwave power divider applications. *Journal of Materials Science: Materials in Electronics* 2025, **36**: 435.

[304] Hao L, Wu Y, Wang W, *et al.* Design of on-chip dual-band bandpass filter using lumped elements in LTCC technology. *IEEE Transactions on Circuits and Systems II: Express Briefs* 2021, **69**: 959–963.

[305] Huang X, Zhang X, Zhou L, *et al.* Low-loss self-packaged Ka-band LTCC filter using artificial multimode SIW resonator. *IEEE Transactions on Circuits and Systems II: Express Briefs* 2022, **70**: 451–455.

[306] Liu H, Cao L, Gu J, *et al.* High-entropy processed high quality and low-temperature cofired $LiMgPO_4$-based dielectric ceramics for low-loss packaged millimeter-wave filters. *Journal of the European Ceramic Society* 2025, **45**: 116957.

[307] He X, Yang W, Liao S, *et al.* 140-GHz high-efficiency low-profile reflectarray antenna using heterogeneous design strategy. *IEEE Transactions on Antennas and Propagation* 2023, **72**: 932–937.

[308] Zhang H, Shamim A. Wideband and wide beam scanning dual-polarized phased array antenna-in-package design for 5G applications. *IEEE Open Journal of Antennas and Propagation* 2023, **5**: 140–152.

[309] Pramono S, Sumantyo JTS, Ibrahim MH, *et al.* A Novel Low Temperature Cofired-Cordierite Ceramic Substrate Based Compact Ultra-Wideband Circularly Polarized Array Antenna for C-Band Remote Sensing Application. *IEEE Open Journal of Antennas and Propagation* 2025.

[310] Zhou QL, Chen X, Fu G. A miniaturized wideband circularly polarized antenna based on tightly coupled monopole. *IEEE Antennas and Wireless Propagation Letters* 2024, **23**: 1864–1868.

[311] Yu Z, Chen C, Chen WD, *et al.* A low-profile LTCC phased array antenna with wideband and high-gain for X-band satellite communications. *IEEE Transactions on Antennas and Propagation* 2024, **73**: 659–664.

[312] Wang D, Xu K-D. Dual-band LTCC substrate integrated cavity slot antenna arrays in D-band for 6G IoT applications. *IEEE Internet of Things Journal* 2024, **12**: 8980–8991.

[313] Yu Z, Chen C, Chen W-d, *et al.* A wideband and low-profile phased array based on metasurface antenna elements in LTCC package. *IEEE Antennas and Wireless Propagation Letters* 2025, **24**: 2197–2201.

[314] Du Z, Pan J, Yang D, *et al.* Quarter-Mode Dielectric-Filled Resonators Based on Virtual Magnetic Walls. *IEEE Microwave and Wireless Technology Letters* 2025, **35**: 650–653.

[315] Wang XY, Pan YM, Tang SC, *et al.* Design of Single-Layer Substrate-Integrated Dielectric Resonator Antenna and Array for Millimeter-Wave Applications. *IEEE Antennas and Wireless Propagation Letters* 2025, **25**: 99–103.

[316] Liu H, Liu Y, Yu X, *et al.* A high-performance, temperature-stable $Mg_{1.99}Ga_{0.01}Si_{0.99}Al_{0.01}O_4$-$CaTiO_3$ microwave dielectric ceramic and its 5 G/6 G waveguide filter. *Journal of the European Ceramic Society* 2023, **43**: 7471–7477.

[317] Wu D-S, Li Y, Xue Q, *et al.* Balanced and unbalanced duplexers using common oval dielectric resonators. *IEEE Transactions on Circuits and Systems I: Regular Papers* 2021, **68**: 3211–3221.

[318] Luo W, Wang X, Chen X, *et al.* Perfect absorption based on a ceramic anapole metamaterial. *Materials Horizons* 2023, **10**: 1769–1779.

[319] Luo W, Zhao R, Liu Y, *et al.* Desymmetrized Metamaterials Enable Perfect Absorption. *Advanced Materials* 2026: e22888.

[320] Guo D, Wang Y, Xia J*, et al*. Investigation of $BaTiO_3$ Formulation: An Artificial Neural Network (ANN) Method. *Journal of the European Ceramic Society* 2002, **22**: 1867–1872.

[321] Guo D, Wang Y, Nan C*, et al*. Application of Artificial Neural Network Technique to the Formulation Design of Dielectric Ceramics. *Sensors and Actuators A: Physical* 2002, **102**: 93–98.

[322] Zhai WH, Lu WC, Liu X*, et al*. Prediction of Properties of $(Zr_{0.7}Sn_{0.3})TiO_4$ Dielectric Ceramics Using Support Vector Regression. *Journal of Applied Sciences* 2005, **23**: 648–653.

[323] Ni Z, Wang F, Guan Y*, et al*. Acceleration of Optimizing the Dielectric Properties of $(Ca_{0.7}Nd_{0.2})_{1-x}(Li_{0.5}Nd_{0.5})_xTi_{1-y}(Mg_{1/3}Nb_{2/3})_yO_3$ with the Aid of Machine Learning. *Journal of the American Ceramic Society* 2024, **107**: 3380–3389.

[324] Appiah M, Yang Y, Ullah B*, et al*. Exceptionally Optimized Millimeter-Wave Properties of Cordierite-Based Materials via Innovative Processing and Predictive Analytics. *Journal of the European Ceramic Society* 2025, **45**: 117206.

[325] Liu X, Huang Q, Su C*, et al*. Deep Learning Enhanced Prediction of Microwave Dielectric Constant of Spinel Ceramics Eliminating Manual Feature Engineering. *Materials Today Physics* 2025, **54**: 101723.

[326] Scott DJ, Manos S, Coveney PV*, et al*. Functional Ceramic Materials Database: An Online Resource for Materials Research. *Journal of Chemical Information and Modeling* 2008, **48**: 449–455.

[327] Scott DJ, Manos S, Coveney PV. Design of Electroceramic Materials Using Artificial Neural Networks and Multiobjective Evolutionary Algorithms. *Journal of Chemical Information and Modeling* 2008, **48**: 262–273.

[328] Qin J, Liu Z, Ma M*, et al*. Machine Learning Approaches for Permittivity Prediction and Rational Design of Microwave Dielectric Ceramics. *Journal of Materiomics* 2021, **7**: 1284–1293.

[329] Qin J, Ma M, Zhang F*, et al*. Machine Learning-Based Optimization of Clausius-Mossotti Equation for Dielectric Constant Calculation. *Journal of the Chinese Ceramic Society* 2025, **53**: 2643–2650.

[330] Sheng Y, Wu Y, Jiang C*, et al*. Interpretable Model of Dielectric Constant for Rational Design of Microwave Dielectric Materials A Machine Learning Study. *Journal of Materials Informatics* 2025, **5**: 1–13.

[331] Liu XB, Su C, Huang QX*, et al*. Machine Learning Enhanced Prediction of Permittivity of Spinel Microwave Dielectric Ceramics Compared to Traditional C-M Calculation. *Modelling and Simulation in Materials Science and Engineering* 2024, **32**: 035002.

[332] Ye Y, Ni Z, Hu K*, et al*. Dielectric Constant Prediction of Perovskite Microwave Dielectric Ceramics via Machine Learning. *Materials Today Communications.* 2023, **35**: 105733.

[333] Xi ZC, Wang X, Wang CH*, et al*. Accelerating Low-*k* Dielectric Material Discovery: From Graph Machine Learning to Synthesis. *ACS Applied Materials & Interfaces* 2025, **17**: 40743–40752.

[334] Liu X, Shao N, Huang Q*, et al*. Enhanced permittivity prediction in microwave dielectric ceramics and structure-property insights via CGCNN combined with GNNExplainer. *Materials Today Chemistry* 2025, **49**: 103088.

[335] Riebesell J, Surta TW, Goodall REA*, et al*. Discovery of high-performance dielectric materials with machine-learning-guided search. *Cell Reports Physical Science* 2024, **5**: 102241.

[336] Morita K, Davies DW, Butler KT*, et al*. Modeling the Dielectric Constants of Crystals Using Machine Learning. *The Journal of Chemical Physics* 2020, **153**: 024503.

[337] Kireeva N, Solov'ev VP. Machine Learning Analysis of Microwave Dielectric Properties for Seven Structure Types: The role of the Processing and Composition. *Journal of Physics and Chemistry of Solids* 2021, **156**: 110178.
[338] Liu R, Chen Z, Lu Z*, et al.* Machine Learning-Assisted Study of the Effects of $CaZrO_3$ and Y_2O_3 Co-doping on the Dielectric Properties of X8R $BaTiO_3$ Based Ceramics. *Ceramics International* 2025, **51**: 30257–30268.
[339] Liu Z, Qian C, Yang X. Machine learning-driven dielectric constant prediction for rock-salt structured microwave dielectric ceramics. *Journal of Alloys and Compounds* 2025, **1044**: 184460.
[340] Liu YC, Liu TY, Huang TH*, et al.* Exploring Dielectric Constant and Dissipation Factor of LTCC Using Machine Learning. *Materials* 2021, **14**: 1–14.
[341] Noda Y, Otake M, Nakayama M. Descriptors for Dielectric Constants of Perovskite-Type Oxides by Materials Informatics with First-Principles Density Functional Theory. *Science and Technology of Advanced Materials* 2020, **21**: 92–99.
[342] Kim E, Kim J, Min K. Prediction of Dielectric Constants of ABO_3-Type Perovskites Using Machine Learning and First-Principles Calculations. *Physical Chemistry Chemical Physics* 2022, **24**: 7050–7059.
[343] Lin X, Li C, Hao H*, et al.* Accelerated Search for ABO_3-Type the Electronic Contribution of Polycrystalline Dielectric Constants by Machine Learning. *Computational Materials Science* 2021, **193**: 110404.
[344] Yao T, Chen L, Hu N*, et al.* Discovering ABO_3-Type Perovskite with Different Dielectric Constants via Intelligent Optimization Algorithm. *AIP Advances* 2024, **14**.
[345] Takahashi A, Kumagai Y, Miyamoto J*, et al.* Machine Learning Models for Predicting the Dielectric Constants of Oxides Based on High-Throughput First-Principles Calculations. *Physical Review Materials* 2020, **4**: 103801.
[346] Shimano Y, Kutana A, Asahi R. Machine Learning and Atomistic Origin of High Dielectric Permittivity in Oxides. *Scientific Reports* 2023, **13**: 22236.
[347] Gopakumar A, Pal K, Wolverton C. Identification of High-Dielectric Constant Compounds from Statistical Design. *npj Computational Materials* 2022, **8**: 146.
[348] Guo Z, Yang H, Qiao H*, et al.* Data-driven and interpretable machine learning accelerates discovery of $Li_4SrCaSi_2O_8$-based microwave ceramics for high-performance dielectric antennas. *Journal of Advanced Ceramics* 2026, **15**: 9221257.
[349] Qin J, Liu Z, Ma M*, et al.* Structure and Microwave Dielectric Properties of Gillespite-Type $ACuSi_4O_{10}$ (A = Ca, Sr, Ba) Ceramics and Quantitative Prediction of the Q×f Value via Machine Learning. *ACS Applied Materials & Interfaces* 2021, **13**: 17817–17826.
[350] Mo L, Qin J, Ma M*, et al.* Machine Learning Assisted Q×f Value Prediction of ABO_4-Type Microwave Dielectric Ceramics. *Journal of Materiomics* 2025, **11**: 100926.
[351] Oba Y, Umeda Y, Ishii D. Materials Informatics for Dielectric Loss Tangent in the Millimeter Wave Region. *Japanese Journal of Applied Physics* 2022, **61**: SN1007.
[352] Yang M, Mo L, Qin J*, et al.* Machine learning assisted τ_f value prediction of ABO_3-type microwave dielectric ceramics. *Journal of Materiomics* 2025: 101117.